Simulating the impact of blue-green infrastructure on the microclimate of urban areas

Ivo L. Suter

Imperial College London

Department of Civil and Environmental Engineering
Imperial College London

Submitted in part fulfilment of the requirements for the degree of Doctor of Philosophy in Civil and Environmental Engineering of Imperial College London.

Abstract

Simulating the impact of blue-green infrastructure on the microclimate of urban areas

Ivo L. Suter

Under supervision of Dr Maarten van Reeuwijk

This dissertation covers the development of two numerical models to investigate the impact of blue-green solutions on the urban microclimate; in particular, how vegetation and green infrastructure in cities influences the surface energy balance, how much water and heat is exchanged by the surface, and how the resulting sensible and latent heat fluxes feed back on the atmospheric flow. The first model is a relatively simple energy balance model and is envisioned to be of use in the master planning stage. The second model is a sophisticated three-dimensional unsteady large-eddy simulation (LES) code which provides information with spatial resolutions of one metre and sub-second time-intervals. This model will be of use primarily in the detailed design phase and for scientific investigations.

The energy balance model MTEB is based on the Town Energy Balance (Masson, 2000). It was extended to incorporate the physics of green roofs; is capable of predicting the urban climate on a neighbourhood scale and to assess the scalability of climate mitigation strategies. The MTEB model solves a set of ordinary differential equations describing the evolution of heat and water on idealised urban surfaces such as roads, walls and roofs. Air movement is not modelled explicitly; instead aerodynamic resistances are used to describe the turbulent heat and moisture transport in the atmosphere. This model was used to investigate the effect of evaporative cooling from green roofs on outdoor air temperatures in an urban environment. Simulations were performed for different climates and urban geometries, with varying soil moisture content, green roof fraction and urban surface layer thickness. All simulations show a linear relationship between surface layer temperature reduction (ΔT_{sl}) and domain averaged evaporation rates from vegetation. The slope of this relationship is called the evaporative cooling potential with a value of $\approx -0.35\mathrm{K\,day\,mm^{-1}}$. This value is independent of the method by which water is supplied. Further, a simple algebraic expression to predict the evaporative cooling potential was derived using a

Taylor series expansion. For a London summer climate the results imply a maximum achievable mean temperature reduction ≤ 0.4K. Thus, without additional watering the outdoor cooling effect of green roofs on a neighbourhood scale is rather limited. The detailed LES model, DALES-Urban (Heus et al., 2010, Tomas et al., 2015), was extended in order to study the complex exchanges between the urban morphology and the atmospheric air. Indeed, turbulence is very heterogeneous and depends strongly on the local morphology and temperature distribution. Turbulence in turn is a major contributor to momentum, energy and moisture fluxes. Wall functions were introduced to model scalar and momentum fluxes at horizontal and vertical structures such as roads, roofs and walls. Energy balances for all urban surfaces, including wall heat flux, heat storage and radiation were fully integrated, where the radiosity approach was being pursued to simulate short- and longwave radiative exchanges. A detailed verification was carried out to ensure that the physics were implemented correctly. These model capabilities allow to simulate urban processes in unprecedented detail allowing to gain new insight into the complex urban microclimate and help urban planning and development.

DALES-Urban was used to perform a study of the effect of a green roof on the “Eastside” building in South Kensington. The 3D building morphology was created from LIDAR data. The results indicate that the presence of a single green roof does neither affect the average wind velocities nor the average air temperature in any substantial way. The green roof surface energy balance shows a clear shift from a sensible to a latent heat flux, leading to cooler vegetated surfaces. The corresponding humidity increase in the air is found to be marginal.

Declaration of originality

All the work presented in this thesis is that of the author. Any work or contributions made by others is referenced appropriately.

Ivo Suter

June 30, 2018

Copyright declaration

Contents

List of figures

List of tables

List of key symbols and abbreviations

Abbreviations

AC	Air conditioning
CFD	Computational fluid dynamics
DALES	Dutch Atmospheric Large Eddy Simulation model
DNS	Direct numerical simulation
GPU	Graphics processing unit
HVAC	Heating, ventilation and air conditioning
IBM	Immersed boundary method
LAI	Leaf area index
LES	Large Eddy Simulation
MPI	Message Passing Interface
MTEB	Modified Town Energy Balance
NBS	Nature based solutions
NDVI	Normalized difference vegetation index
NOAA	National Oceanic and Atmospheric Administration
RANS	Reynolds-averaged Navier–Stokes equations model
RMSE	Root-mean-square error
SEB	Surface Energy Balance
TEB	Town Energy Balance
UBL	Urban boundary layer

UEB	Urban Energy Balance
UHI	Urban Heat Island

Constants

κ	Von Kármán constant, 0.41
ρ_{w}	Density of water, $1000\mathrm{kg\,m^{-3}}$
σ	Stefan-Boltzman constant, $5.67 \times 10^{-8}\mathrm{W\,m^{-2}\,K^{-4}}$
c_{d}	Heat capacity of dry air, $1004\mathrm{J\,kg^{-1}\,K^{-1}}$
g	Gravitational acceleration of Earth, $9.81\mathrm{m\,s^{-2}}$
L_{v}	Latent heat of vaporization, $2.26 \times 10^{6}\mathrm{J\,kg^{-1}}$
Pr	Prandtl number of air, 0.71
R_{d}	Gas constant for dry air, $287.04\mathrm{J\,kg^{-1}\,K^{-1}}$
R_{v}	Gas constant for water vapour, $461.5\mathrm{J\,kg^{-1}\,K^{-1}}$

Model Parameters

C_{s}	Smagorinsky constant, 0.167

Subscripts

atm	Atmosphere.
c	Canyon.
G	Vegetated surface and green roof.
R	Conventional roof.
r	Road.
sl	Atmospheric surface layer.
s	Surface.
w	Wall.

Symbols

α	Albedo. [-]
δ	Fraction of water on a surface. [-]
ϵ	Longwave emissivity. [-]
Γ	Surface conductive heat flux. [$\mathrm{W\,m^{-2}}$]
$\hat{L}$	Obukhov length. [m]
λ	Thermal conductivity. [$\mathrm{W\,m^{-1}\,K^{-1}}$]
$\mathcal{R}$	Runoff. [$\mathrm{kg\,m^{-2}\,s^{-1}}$]
ν	Kinematic viscosity of a fluid. [$\mathrm{m^{2}\,s^{-1}}$]
Ω	Solar azimuthal angle. [rad]
ϕ_h	Dimensionless temperature gradient. [-]
ϕ_m	Dimensionless wind shear. [-]
ψ	View factor. [-]
ρ_a	Density of air. [$\mathrm{kg\,m^{-3}}$]
θ	Potential temperature. [K]
θ_v	Liquid water virtual potential temperature. [K]
υ	Solar zenith angle. [rad]
$\varkappa$	Thermal diffusivity. [$\mathrm{m^{2}\,s^{-1}}$]
φ	Scalar quantity. [various]
ς	Absorptivity. [-]
ζ	Atmospheric stability parameter. [-]
b	Building width. [m]
c	Heat capacity. [$\mathrm{J\,kg^{-1}\,K^{-1}}$]

C_d	Bulk transfer coefficient for momentum. [-]
C_h	Bulk transfer coefficient for heat and moisture. [-]
D	Incoming diffusive shortwave radiation. [W m^{-2}]
d	Layer thickness. [m]
E	Latent heat flux. [W m^{-2}]
e	Evaporative cooling potential. [K m^{2} W^{-1}]
F_h	Stability function for heat and moisture. [-]
F_m	Stability function for momentum. [-]
f_W	Water supply. [W m^{-2}]
G	Ground heat flux. [W m^{-2}]
H	Sensible heat flux. [W m^{-2}]
h	Building height. [m]
I	Solar irradiance. [W m^{-2}]
K	Net shortwave radiation. [W m^{-2}]
$K^{\downarrow}$	Incoming shortwave radiation. [W m^{-2}]
$K^{\uparrow}$	Outgoing shortwave radiation. [W m^{-2}]
L	Net longwave radiation. [W m^{-2}]
l	Street width. [m]
$L^{\downarrow}$	Incoming longwave radiation. [W m^{-2}]
$L^{\uparrow}$	Outgoing longwave radiation. [W m^{-2}]
P	Precipitation. [kg m^{-2} s^{-1}]
p	Atmospheric pressure. [Pa]
q	Specific humidity. [kg kg^{-1}]

R	Incoming reflected shortwave radiation. [W m^{-2}]
r	Resistance. [s m^{-1}]
Re	Reynolds number. [-]
Ri_b	Bulk Richardson number. [-]
S	Incoming direct solar radiation. [W m^{-2}]
T	Temperature. [K]
t	Time. [s]
u_i	Velocity component (u, v or w). [m s^{-1}]
u_*	Friction velocity. [m s^{-1}]
U_T	Magnitude of the wall tangential velocity. [m s^{-1}]
W	Water storage. [kg m^{-2}]
x_i	Coordinate in Euclidean space (x, y or z). [m]
z_0	Aerodynamic roughness length. [m]

1
Introduction

The fast growth of global population, mainly in urban areas (UNFPA, 2012) and the concurrent increase in likelihood of extreme weather events (IPCC, 2014) due to climate change forces cities to prepare for water scarcity and heat spells. Furthermore, air & noise pollution and other adverse impacts affect an increasing number of people; posing severe threats to health and stability of cities in the future.

These problems are amplified due to the fact that the densely built environment of cities differs strongly from a natural land surface. And as a consequence the interplay of many processes lead to an altered urban climate and to the urban heat island (UHI) effect (Oke, 1982, Rosenzweig et al., 2015), the tendency that cities are hotter than the rural surrounding. In particular effects of radiation, anthropogenic heating and vastly different material and surface properties are responsible.

Vegetation has a large impact on the temperature close to the surface and can alleviate some of the temperature-related problems. Vegetated surfaces are generally colder than classical building materials such as metal, brick or concrete as energy is used for the evaporation of water. This energy would otherwise heat up the ground, infrastructure and atmosphere (Getter & Rowe, 2006). Greening of façades and roofs can mitigate the effects of the urban heat island (Santamouris, 2014), specifically, improve thermal comfort and lower heat stress due to enhanced evapotranspiration from vegetation during hot and dry periods. Green roofs or walls also lead to lower indoor temperatures and reduce the energy demand for air conditioning (Castleton et al., 2010). Consequently, the augmented installation of green infrastructure such

as vegetated roofs or walls is a possible remedy for exceedingly hot cities and the subsequent health problems.
Initiatives such as the Blue-Green Dream project that was funded by Climate-KIC (Blue Green Dream, 2018, Climate-KIC, 2018) promote the increased use of vegetation in urban planning & development and show that these solutions are preferable both from a sustainability and financial perspective (Bozovic et al., 2017). Plants and other Nature Based Solutions (NBS) can bring many benefits to urban areas compared to historically utilized methods of development. Air and water pollution, flood risk and the urban heat island effect can be reduced; carbon dioxide emissions are lower and additionally they are often preferential for financial and aesthetic reasons (European Commission, 2012, United Nations Environment Programme, 2014, Tzoulas et al., 2007). The Blue-Green Dream thus advocates the use of vegetation and other NBS in urban development. However, developing adaptation and mitigation strategies requires state-of-the-art tools to predict and study the effects of such measures. This dissertation is part of the Blue-Green Dream project and aims to provide modelling tools to assess the climate in the urban environment. A large number of scales and physical processes are involved in the formation of urban microclimates and we generally lack a profound understanding of the interplay of all these factors. In the remainder of this chapter some of the most important processes will be introduced. This thesis presents the efforts of capturing these processes and developing a model to study the urban microclimate are presented.

1.1 The heterogeneity of the urban canopy

Figure 1.1 demonstrates clearly the heterogeneity of the urban landscape. The urban structure[1] varies strongly: roads can be built in patterns or grow more organically; residential, commercial and industrial zones segment cities; and also vegetation and open water lead to stark contrasts. Furthermore the patterns of surface cover and the urban fabric, i.e. the material composition and texture of the urban surface, is subject to great variability. This represents a major challenge to all attempts of modelling, since, at its core, a model is an abstraction and simplification of the

[1] The three-dimensional configuration of urban elements

Figure 1.1: View of Seattle (US-WA). The landscape of cities is extremely heterogeneous. Vegetation and open water surfaces contrast with the built environment; buildings, roads and car parks in various shapes and material composition.
From: `https://pixabay.com`, Creative Commons CC0 Licence.

problem. Urban processes take place on a large range of spatial- and timescales and appreciating the range of scales involved is "probably the single most important key to understanding urban climates" (Oke et al., 2017). Figure 1.2 shows a range of typical time- and length scales of phenomena of the urban climate. In the macro-scale the dynamics of large pressure systems take place. These processes may still be influenced by large urban areas yet no details of cities are resolved. On the other side of the spectrum, the smallest micro-scale processes include dissipation of kinetic energy in Kolmogorov eddies ($O(1\text{mm})$) or aerosol processes ($O(1\mu\text{m})$). Also into the micro-scale fall turbulent eddies forming around buildings, trees and other obstacles. The range 100m-50km forms the local-scale, which is an integration of a mix of microclimatic effects; and in turn the combination of individual local-scales plumes produces the urban boundary layer (UBL), which is a meso-scale phenomenon. Besides length scales also timescales vary substantially, and for many processes the two are fundamentally linked.

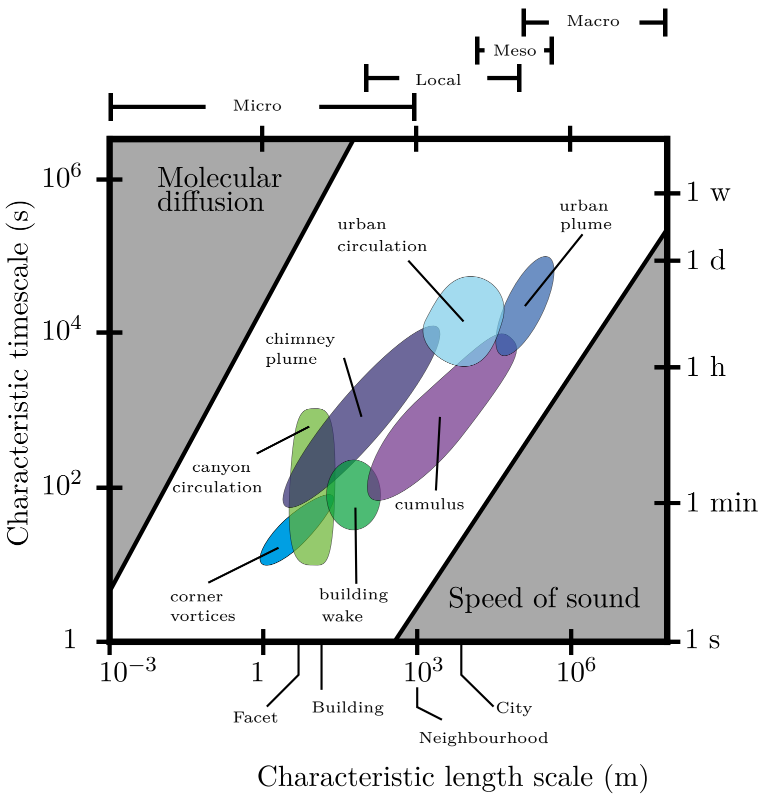

Figure 1.2: Time- and horizontal space scales of selected urban climate dynamics phenomena. The names of urban scales is given below the image, the atmospheric scales above. After Oke et al. (2017).

1.2 The urban energy balance

Any attempt to understand how the urban microclimate differs from the rural surroundings must start with an analysis of their respective surface energy balances (SEB). This section introduces the basic equation describing the energy exchange taking place at any surface. Urban areas exchange energy in various forms (Erell et al., 2011), such as incoming and outgoing longwave ($L^{\downarrow}$, $L^{\uparrow}$) and shortwave radiative fluxes ($K^{\downarrow}$, $K^{\uparrow}$), the turbulent sensible heat flux (H), the turbulent latent heat flux (E), ground heat flux (G) and the heat storage per unit time (dQ/dt, often denoted ΔQ). Additional heat sources[1], e.g. anthropogenic heating, could be added if desired (O). These fluxes have to balance and the SEB is expressed as

$$\frac{dQ}{dt} = (L^{\downarrow} - L^{\uparrow}) + (K^{\downarrow} - K^{\uparrow}) - (H + E + G) + O, \tag{1.1}$$

where all the terms have unit W m^{-2}. In this presentation a number of processes have been introduced. For the transport of energy, three modes are possible:

- Radiation, transport by propagation of electromagnetic radiation: $L^{\downarrow}$, $L^{\uparrow}$, $K^{\downarrow}$ and $K^{\uparrow}$.
- Conduction, transport of energy through matter by molecular interactions: G.
- Advection, transport of energy by the movement of matter: H and E.

1.3 Electromagnetic radiation

Radiative fluxes occur on the whole electromagnetic spectrum. Nevertheless, only two wavelength-bands contain a significant amount of energy in atmospheric processes near the surface. These two bands are here called “shortwave” ($< 4\mu$m) and “longwave” ($\geq 4\mu$m).: Shortwave radiation is radiation originating from the sun; either direct, or after interaction with other surfaces or the atmosphere. The spectrum of solar radiation contains most energy in the visible light (0.4-0.7 μm). The

[1]Under certain circumstances anthropogenic energy fluxes can be the largest term in the SEB. It is highly recommended to include the effects of HVAC and traffic in the future. Traffic is of further interest since vehicles also displace considerable amounts of air and introduce turbulence. However, modelling anthropogenic processes is largely beyond the scope of this thesis.

visible wavelength range is also the part of the spectrum that is used by plants for photosynthesis Hall & Rao (1999).
Shortwave radiation thus depends on the daily and annual cycles of the sun/earth and the state of the atmosphere. Furthermore, radiation will be partly absorbed and partly reflected if it hits an object and so reflected radiation from other surfaces has to be considered as well. In a very heterogeneous terrain such as cities, the shadowing and reflection patterns can heavily influence the local SEB and thus temperatures. Figure 1.3 shows how the angle of incoming shortwave radiation, shading and reflections interact with the urban geometry. Radiation can be reflected multiple times from different surfaces, each time losing some of its energy. The effect that it is difficult for radiation to leave the urban geometry is called "radiation trapping".
Longwave radiation originates from every object; surfaces and also the atmosphere; based on the entities temperature. The largest part of longwave emission occurs between 4μm and 100μm (Petty, 2006). Longwave radiation emitted by one surface can be reabsorbed by another. For cases where the gap between two walls is relatively small this also leads to "trapping", since most of the emitted radiation will be reabsorbed by the opposing wall (see Fig. 1.3). This medley of processes and their strong influence makes the prediction of the surface energy balance a challenging matter.

1.4 Nature-based solutions & Blue-Green infrastructure

Plants serve as an intermediary between the soil and the atmosphere. This Section describes the process of evaporation and transpiration and the modification of the near-surface atmosphere by vegetation. The behaviour of plants under various environmental conditions has been studied extensively (Moene & van Dam, 2014), especially for crops, and a host of models exist which exceed the needs of this project. Processes like root water uptake, water flow within the plants or photosynthesis will not be considered here. However, of major interest are the exchange of momentum, heat and water between the surface and the atmosphere. Transpiration from plants and soil evaporation extract water from the soil and release it into the air. Together these terms are called evapotranspiration. Evaporation and transpiration occur si-

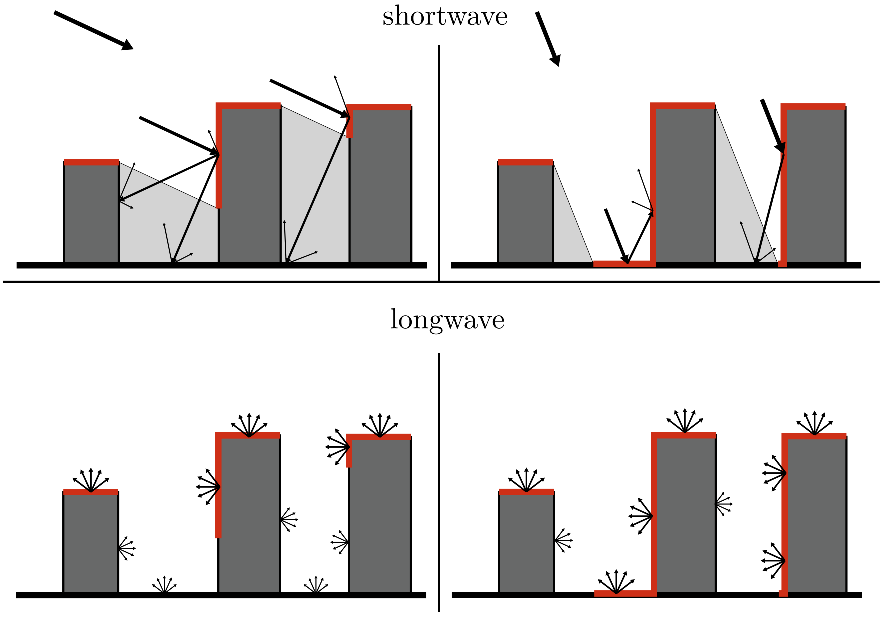

Figure 1.3: Top: Influence of solar angle on shortwave radiation, reflections and shading. The temperature of surfaces and the space between buildings depends strongly on the interplay of these two mechanisms.
Bottom: In narrow gaps a large fraction of emitted longwave radiation is reabsorbed by surrounding surfaces. The longwave radiation is thus “trapped” between buildings leading to warmer surfaces.

multaneously and there is no easy way of distinguishing between the two processes. Apart from water availability in the top soil, the evaporation from vegetation is determined mainly by the solar radiation reaching the leaves. The phase change from liquid water into water vapour in the air requires large amounts of energy, generally provided by the radiation. Furthermore, the pores in the leaves, stomata, are open during the daytime to allow the exchange of gases used in photosynthesis, facilitating transpiration. The energy exchange associated with the evapotranspiration is called latent heat flux E. Yet, the air temperature close to the surface is largely determined by the sensible heat flux H. Since the other terms in Eq. 1.1 remain relatively constant between vegetated and unvegetated surfaces, it is due to this fact that vegetation is generally attributed to cool the air in its vicinity. Tall vegetation like trees also provide shade for lower surfaces. While trees are indeed a very interesting topic in the area of urban climate, the focus of this thesis lies on the effect of green roofs and trees and tall vegetation are not considered here. Heat transport through the ground G is in reality also strongly modified by the presence of vegetation cover or snow, when freezing or thawing occurs and by flowing water within the soil.

1.5 Transport in the Atmospheric Surface Layer

Mixing and transport of energy and water vapour in the atmosphere is mainly caused by the movement of air. The mixing is generated by turbulence, the tendency that the flow of the wind exhibits chaotic deviations in its characteristic properties, such as its speed and direction. The extent of atmospheric turbulence depends upon the nature of the flow itself and the effect of obstacles encountered. In the urban canopy these obstacles are numerous and the drag on the wind produces turbulence, but decreases its average velocity. Within the surface layer the wind speed thus generally increases with height. Yet, the presence of buildings and other obstacles forces the air to flow around them, which can locally induce high wind speeds even at ground level. Typically, the taller the building, the lower the pressure on the leeward side and the higher the velocities that are induced (Erell et al., 2011). In the low-pressure leeward wake, on the other hand, the local flow is often found to reverse direction. A schematic diagram of the turbulence within the urban surface layer can be seen in

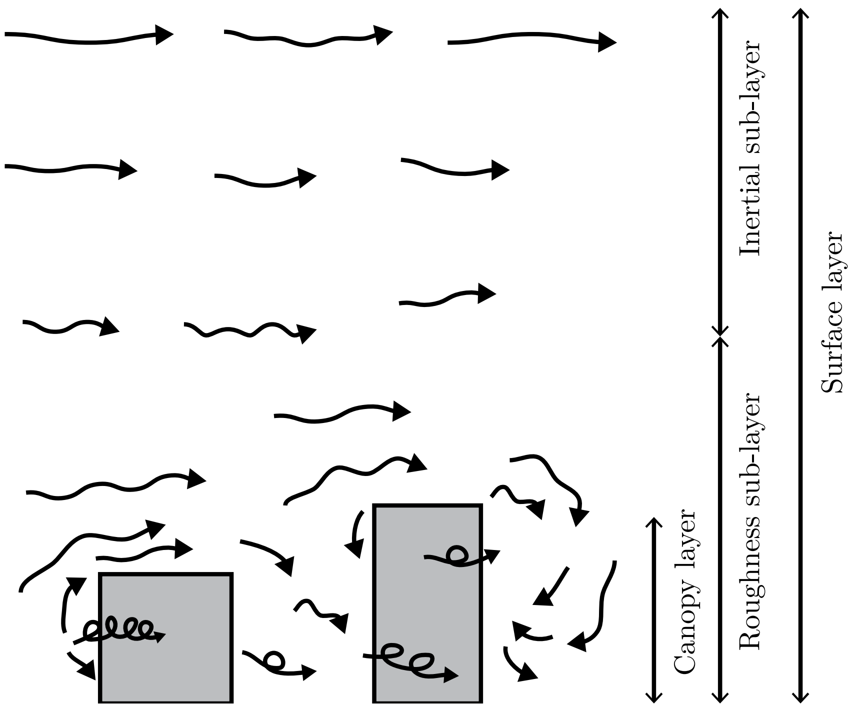

Figure 1.4: Schematic diagram of roughness and inertial sub-layers. The urban surface layer is very turbulent, especially within the canopy. The mean velocity increases with height.

Figure 1.4. The fact that the air has to flow around buildings implies that between and just above those obstacles the mean turbulent quantities can vary drastically and even well away the effect of the surface on the profiles of mean quantities remains. The surface layer is thus often divided into sub-layers (e.g. Barlow, 2014). The canopy layer reaches up to the mean height of buildings/trees, in the roughness sub-layer the flow is still affected by individual obstacles. Above, in the inertial sub-layer, a logarithmic wind profile develops.

To grasp the concepts of mean and turbulent characteristics mathematically, the wind velocity ($\mathbf{u}$) and scalar quantities are often split into two parts using Reynolds decomposition:

$$u_\mathrm{i} = \overline{u}_\mathrm{i} + u'_\mathrm{i} \tag{1.2}$$

$$\varphi = \overline{\varphi} + \varphi' \tag{1.3}$$

where u_i are the components of the velocity vector and φ can be any scalar quantity, including directional momentum $\varphi = \rho_a u_\mathrm{i}$. The overlines ($^{-}$) indicate averaging and

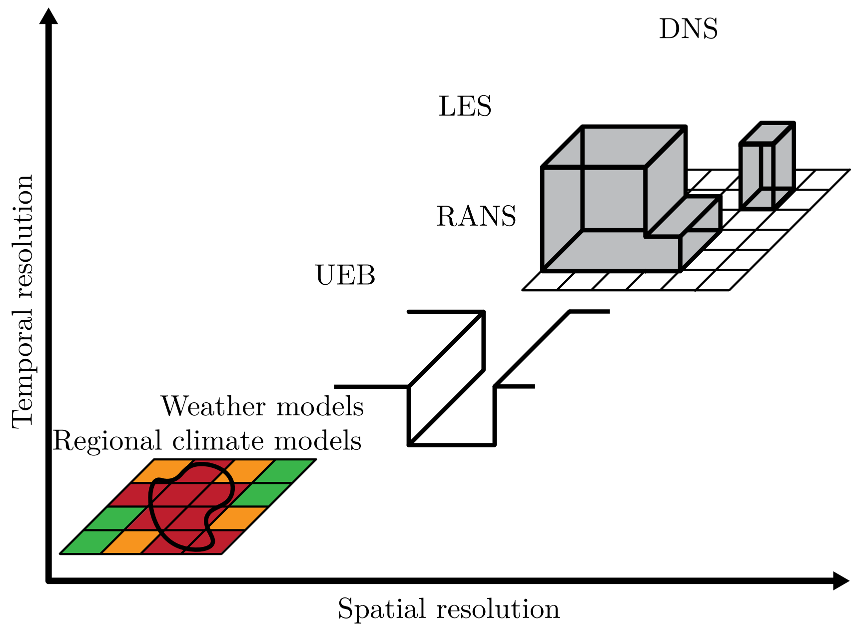

Figure 1.5: Increasing complexity of urban modelling tools: from tile representation of landscapes in climate & weather models over spatially averaged canyon representation in UEB to fully obstacle resolved RANS, LES and DNS.

the primes ($'$) are the fluctuations, i.e. the deviations from those means. Commonly the ergodic principle is applied and time averaging is done to obtain $\overline{u}_{\mathrm{i}}$ and $\overline{\varphi}$ (e.g. Ghannam et al., 2015). Reynolds decomposition allows us to differentiate between the fluxes due to mean transport and fluxes due to turbulence:

$$\overline{u_{\mathrm{i}}\varphi} = \overline{u}_{\mathrm{i}}\overline{\varphi} + \overline{u_{\mathrm{i}'\varphi'}} \tag{1.4}$$

where $\overline{u}_{\mathrm{i}}\overline{\varphi}$ is the transport due to mean quantities and $\overline{u'_{\mathrm{i}}\varphi'}$ is the turbulent/eddy flux of φ in the direction of u_{i}. For example, the turbulent vertical flux of horizontal momentum can be expressed as $\rho_{\mathrm{a}}\overline{w'u'}$.

1.6 Existing urban climate modelling tools

Several possible approaches for studying urban climate have been used, ranging from observation to numerical simulations. In this context, the physical processes set out in the preceding pages and their complex interactions must be taken into account

(Mirzaei & Haghighat, 2010, Mirzaei, 2015, Moonen et al., 2012, Arnfield, 2003, Rizwan et al., 2008, Grimmond, 2007, Barlow, 2014). A diagram showing different approaches can be seen in Figure 1.5. One possible approach is the use of standalone urban energy balance (UEB) models. UEBs are based on the concept that total energy in the urban boundary layer, the lowest few hundred meters of the atmosphere, has to be conserved. UEBs are widely used as surface schemes in numerical weather prediction and regional atmospheric models, such as the Town Energy Budget (Masson, 2000, TEB) used by the French national weather service (Météo-France) or the Joint UK Land Environment Simulator (Best et al., 2011, Clark et al., 2011, JULES) by the UK Met Office. They are computationally inexpensive and include many physical processes, but are still very simplified representations of the urban environment. The building geometry is often only represented in an averaged sense, and no single building can be studied. Furthermore, the transport in the air is parameterised since the Navier-Stokes equation (Eq. 3.2) describing air movement is not solved explicitly. Other UEBs include variations of TUF (Krayenhoff & Voogt, 2007, Yaghoobian & Kleissl, 2012), SUEWS (Järvi et al., 2011), RayMan (Matzarakis et al., 2010) and the SOLWEIG model (Lindberg et al., 2008). An UEB is used in Chapter 2 to study the effect of evaporative cooling on outdoor air temperatures.

A more complex approach is the use of computational fluid dynamics (CFD) models. The explicit simulation of the turbulent flow is computationally expensive and many of the CFD models applied for urban climatology studies today are based on the Reynolds-averaged Navier-Stokes (RANS) equation, e.g. MIMO (Ehrhard et al., 2000), MITRAS (Schlünzen et al., 2003), ENVI-met (Huttner, 2012) and MUKLIMO3 (Sievers, 2016). RANS models predict the mean flow field. This allows for use of relatively large time-steps and lower computational demands. On the downside small eddies interacting within the urban canopy will not be captured and thus important processes in the heterogeneous terrain will not be reproduced, especially in non-neutral situations.

Large-Eddy simulation (LES) tools are better suited for more detailed studies. They resolve the large eddies containing the bulk of the turbulent energy spectrum explicitly, while parameterising only the small eddies. Examples of LES models capable of dealing with urban terrain are PALM-USM (Maronga et al., 2015, Resler et al., 2017) and OpenFoam2. However, most CFD models neither contain a representation of energy exchanges at the urban surface nor explicitly treat radiative fluxes. Coupling of stand-alone energy balance models is a possibility (Musy et al., 2015), yet there persist technical difficulties and different approaches in model design across research groups. Due to the increase in computational resources in recent years LES models are currently the most promising method to provide sufficiently detailed information about the urban microclimate. For these reasons urban LES models are being developed that include many of the important processes that shape the urban environment, such as surface energy balances, treatment of radiation, effect of vegetation and anthropogenic heating. In this project the Dutch Atmospheric Large-Eddy Simulation (DALES) model (Heus et al., 2010, Tomas et al., 2015) is being used and further extended to include descriptions for radiation, vegetation and energy and momentum fluxes from urban surfaces.

Little is known about how the air circulation is influenced by green infrastructure. The plants themselves affect the flow around them by representing additional roughness, essentially reducing wind velocity close to the surface. The exchange of water and heat modifies the air's buoyancy. This is of importance for the ventilation of urban street canyons, where the air often poorly mixes with air aloft, but most human activities take place. It is thus the goal to be able to model the urban air flow with the effects of buildings and green infrastructure on a neighbourhood scale.

1.7 Scope

The focus of this dissertation is the development of capabilities to predict the effect of vegetation on the urban microclimate. A two-pronged approach has been taken in which a rapid model has been developed for urban planning applications and a LES model was developed for detailed scientific investigations. The fast method estimating the effect of green façades and roofs can be used in integrated modelling studies, e.g. in conjunction with building energy models, to facilitate urban planning and design. The extended LES model accommodates the heterogeneity of the urban landscape and includes the most relevant physical processes determining the urban microclimate.

Therefore, the following objectives have been formulated:

- Create a tool for integrated modelling of the effect of vegetation for urban planning.
- Develop the capabilities to study vegetation and the urban microclimate using LES. Including following processes:
  - Long- and shortwave radiation.
  - Representation of various surfaces properties and vegetated surfaces.
  - Heat, moisture and momentum exchange on all surfaces.
  - Wall & ground heat flux. Energy storage in walls, roofs and roads.

The desired applications of the resulting model include

- predicting the effect of the installation of green roofs and green walls on the local microclimate.
- modelling the effect of shading and albedo on radiation and surface temperatures.
- examining turbulent structures in the urban boundary layer and suburban-urban transition.
- studying the urban heat island effect and the importance of thermal inertia.

Emphasis was placed on simulating dry and hot weather conditions and all assumptions were made on this basis; e.g. no modelling of snow and water cover on urban surfaces.

1.8 Structure of this thesis

This report is structured as follows. This chapter covers the background of urban climate and how it is influenced by vegetation and radiation. In Chapter 2 an urban energy balance model is adopted to predict the cooling over an urban area due to evapotranspiration from vegetation. In Chapter 3 the LES model is introduced and how we deal with boundaries in the fluid domain and the fluxes on those boundaries. Chapter 4 is about urban facets, radiation and the implementation of a surface energy balance into the LES model. Finally, in Chapter 5 the new model is applied in a realistic case to highlight the new capabilities.

2

Energy balance modelling

2.1 Introduction

This chapter focuses on evaluating the effect of evaporative cooling on outdoor air temperatures in an urban environment and is adapted from the 2017 Urban Climate article "A neighbourhood-scale estimate for the cooling potential of green roofs" by Ivo Suter, Čedo Maksimović and Maarten van Reeuwijk (Suter et al., 2017).

Quantifying the cooling effect of green roofs on outdoor air temperatures is difficult and various studies suggest only a small temperature reduction on street level (Li et al., 2014, Gromke et al., 2015, Yang et al., 2016). Roofs with a high albedo, so-called "cool roofs", reflect a larger proportion of solar radiation than conventional roofs and may excel in reducing outdoor temperatures (Mackey et al., 2012, Georgescu et al., 2014, Santamouris, 2014), but they lack the additional benefits for ecology and water management that green roofs provide (Oberndorfer et al., 2007). Yet, to significantly improve thermal comfort both cool and green roof strategies need to be implemented on a large scale. This brings up the question how efficiently the implementation of green roofs can be scaled up. Li et al. (2014) and Sun et al. (2016) describe a linear decrease of air temperature with green roof fraction, Mackey et al. (2012) compare temperature reduction to the normalised difference vegetation index (NDVI) from satellite measurements and also find a linear relationship. However, this dependency is not well understood, yet if it generally holds, a fast way of determining the slope coefficient depending on urban characteristics will be of great support for decision makers and urban planners. To this purpose an established urban energy balance model was modified to quantify the cooling potential of green roofs and study the scalability of potential mitigation strategies. Specifically, this chapter will

1. quantify the cooling of green roofs on an urban scale taking the UEB model approach (Oke, 1988, Grimmond et al., 2010);

2. examine how the cooling relates to the evaporation rates;

3. derive a relatively simple equation for the cooling potential for a given amount of water to evaporate.

In section 2.2 the original UEB model and the changes we made for simulating green roofs in an urban environment are discussed. Section 2.3 presents steady and unsteady diurnal cases simulated with the new model and investigates the effect of surface layer thickness, urban geometry, method of water supply and evaporation from green roofs on the surface layer temperature. In section 2.4 an algebraic equation to predict the cooling from green roofs is derived which is subsequently compared to the findings in section 2.3. Finally, in section 2.5 we discuss our findings and set them into context of application in real cities.

2.2 Urban Energy Balance Model

The coupling of numerical weather prediction models with the (urban) surface is usually achieved by using land surface modules such as the Town Energy Budget (Masson, 2000, TEB) used by the French national weather service (Météo-France) or the Joint UK Land Environment Simulator (Best et al., 2011, Clark et al., 2011, JULES) by the UK Met Office. These models are based on a surface energy balance (Eq. 1.1). UEB models solve a set of ordinary differential equations describing the evolution of heat and water on urban surfaces such as roads, walls and roofs. Air movement is not modelled explicitly; instead aerodynamic resistances are used to describe the turbulent heat and moisture transport in the atmosphere. We used the open source TEB as starting point for our UEB model. Here we summarise the principles underlying TEB, for a detailed description see Masson (2000). The urban

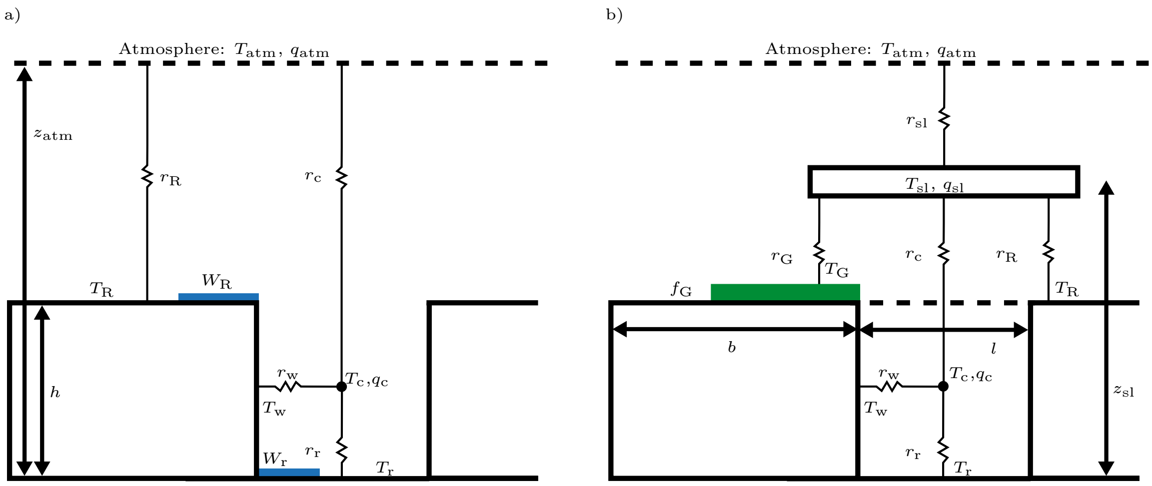

Figure 2.1: a) Schematic of TEB. b) Schematic of the modified TEB scheme, including the surface layer above the canyon and green roofs. The symbol T denotes temperature, q specific humidity, W water, and r aerodynamic resistance. The subscript $_{\mathrm{R}}$ stands for conventional roof, $_{\mathrm{G}}$ for green roof, $_{\mathrm{r}}$ for road, $_{\mathrm{w}}$ for wall, $_{\mathrm{c}}$ for canyon, $_{\mathrm{sl}}$ for surface layer and $_{\mathrm{atm}}$ for the atmosphere. The geometry is given by building height h, building width b and canyon width l. The middle of the surface layer is at an elevation z_{sl} and the atmospheric forcing height is z_{atm}. f_{G} is the fraction of green roof to total roof area.

geometry in TEB is represented as a generic street canyon, including a single conventional roof (R), wall (w) and road (r) surface (Figure 2.1a). The scheme assumes isotropy for the street and house distribution on a large horizontal scale. Equations describing directional process such as radiation are thus integrated horizontally over 360°. TEB therefore does not represent single buildings, but rather the average over a large domain. The canyons are represented by mean building height (h), building width (b) and road width (l). Grimmond et al. (2010) have previously shown that more complex UEB models do not necessarily yield more accurate results. Three distinct energy budgets are considered for the roof, wall and road. The TEB scheme thus takes the form of five coupled differential equations, three for the temperatures and two for the water reservoirs on the roof and the road. The evolution of temperature with time is described as

$$c_\star d_\star \frac{dT_\star}{dt} = K_\star + L_\star - H_\star - E_\star - G_\star, \tag{2.1}$$

where $T_\star$ [K] represents the roof, wall or road temperature, respectively. The corresponding heat capacity is c [J m^{-3} K^{-1}] and the layer thickness d [m]. K is the net shortwave radiation, L the net longwave radiation, H the sensible heat flux, E the latent heat flux and G the ground heat flux, all in $\mathrm{W\,m^{-2}}$. For roofs and walls the ground heat flux G actually describes the conduction heat flux into the buildings, not into the ground. Yet, since the temperature evolution inside both the buildings and the ground below roads are not modelled explicitly, a distinction is not necessary. The water (W) budget on the roof and road is

$$\frac{dW_\star}{dt} = P - \frac{E_\star}{L_\mathrm{v}} - \mathcal{R}, \tag{2.2}$$

where P [$\mathrm{kg\,m^{-2}\,s^{-1}}$] is the precipitation rate, L_v [$\mathrm{Jkg^{-1}}$] is the latent heat of vaporization and $\mathcal{R}$ [$\mathrm{kg\,m^{-2}\,s^{-1}}$] is the runoff. The air inside the canyon is assumed not to have any significant heat capacity and therefore its temperature adjusts instantaneously to the flux balance between road, walls and canyon top. The sensible, latent and ground heat fluxes are defined as,

$$H_\star = \frac{c_\mathrm{p}\rho_\mathrm{a}(T_\star - T_\mathrm{atm})}{r_\star}, \tag{2.3}$$

$$E_\star = \frac{L_\mathrm{v}\rho_\mathrm{a}\delta_\star(q_\star - q_\mathrm{atm})}{r_\star}, \tag{2.4}$$

$$G_\star = \lambda_\star\frac{T_\star - T_\mathrm{bld}}{d_\star}, \tag{2.5}$$

respectively. Here c_p [$\mathrm{J\,kg^{-1}\,K^{-1}}$] is the heat capacity of dry air at constant pressure and ρ_a [$\mathrm{kg\,m^{-3}}$] is the density of air, $\delta_\star$ [-] is the fraction of water on the respective surface and q [$\mathrm{kg\,kg^{-1}}$] is the specific humidity. Sensible (2.3) and latent heat fluxes (2.4) between wall, canyon and atmosphere depend on the aerodynamic resistances $r_\star$ [$\mathrm{s\,m^{-1}}$]. These resistances describe the transport in the atmosphere and depend on the atmospheric stability, i.e. on the local temperature and wind profile. Ground heat flux (2.5) is based on one-dimensional thermal conductivity, where $\lambda_\star$ [$\mathrm{Wm^{-1}K^{-1}}$] is the effective thermal conductivity, $d_\star$ [m] is the layer thickness and T_bld [K] is the constant internal building temperature, or, when considering roads, the constant ground temperature, respectively. One has to keep in mind that a constant building temperature is in reality only achieved by using HVAC, an effect which is currently not being considered in this model. The walls, roof and roads are described as a single layer with one effective resistance throughout this chapter. For a complete account of the TEB, especially the treatment of radiation and details on the aerodynamic resistances, see the original model description by Masson (2000).

Since TEB is used as a surface parameterisation for numerical weather prediction models, the fluxes from roof and canyon are directly linked to the atmosphere and they are completely independent of each other (see Figure 2.1a). As a consequence it is not possible to study the effect of roofs on canyon temperature. In order to allow the roof to interact with the other surfaces, it is necessary to introduce an additional air layer between the roof and the atmosphere (Figure 2.1b). The introduction of this surface layer splits the original resistances into two parts. The surface layer air has a moisture content (q_{sl}) and a heat capacity, i.e. temperature (T_{sl}). The evolution of the surface layer's air temperature and specific humidity are given by

$$c_{\mathrm{sl}} d_{\mathrm{sl}} \frac{dT_{\mathrm{sl}}}{dt} = \left(a_{\mathrm{R}} H_{\mathrm{R}} + a_{\mathrm{c}} H_{\mathrm{c}} + a_{\mathrm{G}} H_{\mathrm{G}} - H_{\mathrm{sl}}\right), \tag{2.6}$$

$$\rho_{\mathrm{a}} L_{\mathrm{v}} d_{\mathrm{sl}} \frac{dq_{\mathrm{sl}}}{dt} = \left(a_{\mathrm{R}} E_{\mathrm{R}} + a_{\mathrm{c}} E_{\mathrm{c}} + a_{\mathrm{G}} E_{\mathrm{G}} - E_{\mathrm{sl}}\right). \tag{2.7}$$

The fluxes from the canyon, conventional roof, green roof and surface layer are denoted with subscripts $_{\mathrm{c}}$, $_{\mathrm{R}}$, $_{\mathrm{G}}$ and $_{\mathrm{sl}}$, respectively. The flux from the canyon is the sum of the fluxes from the road and the walls. The surface layer stretches the entire area of the urban unit, while the conventional roof, green roof and canyon only cover a part of the area each. The fraction covered by the canyon, green roof and conventional roof are $a_{\mathrm{c}} = l/(b+l), a_{\mathrm{G}} = f_{\mathrm{G}} b/(b+l), a_{\mathrm{R}} = (1-f_{\mathrm{G}})b/(b+l)$, respectively. Note that by definition $a_{\mathrm{c}} + a_{\mathrm{G}} + a_{\mathrm{R}} = 1$. The terms in (2.6) and (2.7) are thus scaled accordingly. During extreme hot weather, open water surfaces on buildings and roads are irrelevant and will not be considered. The green roof temperature T_{G} is governed by equation (2.1), whilst the green roof water W_{G}, i.e. soil moisture, is evolving according to

$$L_{\mathrm{v}} \frac{dW_{\mathrm{G}}}{dt} = L_{\mathrm{v}}(P - \mathcal{R}) + f_{\mathrm{W}} - E_{\mathrm{G}}, \tag{2.8}$$

where $f_{\mathrm{W}}/L_{\mathrm{v}}$ is the additional supply through watering of the plants in $\mathrm{kg\,m^{-2}\,s^{-1}}$. The soil moisture W_{G} is expressed in $\mathrm{kg\,m^{-2}}$ so that the values are consistent with the water content on conventional roofs and roads $W_{\star}$. Furthermore the constant thickness d_{G} of the green roof can be omitted from equations. Dividing the values of

W_G by d_G will lead to values for soil moisture in $\mathrm{kg\,m^{-3}}$. To represent the evaporation from vegetation and soil the Penman-Monteith approach (Jarvis, 1976, Noilhan & Planton, 1989, ECMWF, 2013) was utilised:

$$E_\mathrm{G} = \frac{\frac{dq_\mathrm{sat}}{dT}(K-G) + \frac{\rho c_\mathrm{p}}{r_\mathrm{a}}(q_\mathrm{sat}(T) - q_\mathrm{sl})}{\frac{dq_\mathrm{sat}}{dT} + \frac{c_\mathrm{p}}{L_\mathrm{v}}(1+\frac{r_\mathrm{c}}{r_\mathrm{a}})} \tag{2.9}$$

where q_sat $[\mathrm{kg\,kg^{-1}}]$ is the saturation specific humidity and $\frac{dq_\mathrm{sat}}{dT}$ is the slope of the saturation specific humidity in $\mathrm{kg\,kg^{-1}\,K^{-1}}$. The aerodynamic resistance r_a is obtained in the same way as all the other aerodynamic resistances as described in Masson (2000). The resistance of the vegetation r_c is parameterised as:

$$r_\mathrm{c} = \frac{r_\mathrm{c,min}}{LAI} f_1(K) f_2(W_\mathrm{G}) f_3(T_\mathrm{sl}), \tag{2.10}$$

$$f_1(K) = \min\left(1, \frac{c_1 K + 0.05}{0.81(c_1 K + 1)}\right)^{-1}, \tag{2.11}$$

$$f_2(W_\mathrm{G}) = \frac{W_\mathrm{fc} - W_\mathrm{wilt}}{W_\mathrm{G}/d - W_\mathrm{wilt}}, \tag{2.12}$$

$$f_3(T_\mathrm{sl}) = \frac{1}{1 - c_2(T_\mathrm{sl} - c_3)^2}. \tag{2.13}$$

where $c_1 = 0.004\mathrm{m^2\,W^{-1}}$, $c_2 = 0.0016\mathrm{K^{-2}}$, $c_3 = 298\mathrm{K}$, LAI is the Leaf Area Index, d [m] is the thickness of the soil layer, W_wilt $[\mathrm{kg\,m^{-3}}]$ is the volumetric soil moisture at wilting point and W_fc $[\mathrm{kg\,m^{-3}}]$ is the volumetric soil moisture at field capacity.

2.3 Results

2.3.1 Steady state

In this section the modified TEB (MTEB) is used to study the effect of green roofs on the local microclimate. Of particular interest is the relationship between air temperature (T) and latent heat flux (E), since the latter can be directly influenced by increasing the area of green roofs or by additional watering of the plants. Four steady state scenarios are being studied with different geometries and climates as described in Table 2.1. All scenarios represent summer conditions, with no open water available for evaporation. Hot scenarios (**H**) are in an environment with high atmospheric temperature (32°C) and solar radiation (520W m^{-2}), cool (**C**) scenarios have lower temperature (22°C) and radiation (480W m^{-2}). The narrow (**N**) canyon geometry has a street width of 12m and building width of 26m. The wide (**W**) geometry features 20m wide roads and buildings.

Table 2.1: Scenario parameters: Case identifier, atmospheric temperature (T_{atm}), building height (h), building width (b) and street width (l).

Case	K [W m^{-2}]	T_{atm} [°C]	h [m]	b [m]	l [m]
CN	480	22	20	26	12
CW	480	22	20	20	20
HN	520	32	20	26	12
HW	520	32	20	20	20

For all cases external forcings, i.e. the incoming solar radiation and atmospheric temperature, were held constant during the simulation, thus given enough time the system attains a steady state. Therefore, the values for S and T_{atm} in Table 2.1 must be interpreted as daytime means. In reality, urban climate never reaches a steady state and the diurnal cycle plays an important role. Nevertheless, the steady state results will prove to be representative also for cities with a diurnal cycle as will be shown in Section 2.3.2.

The wind velocity at 48m was 3m s^{-1} and the longwave forcing was modelled as in Swinbank (1963) and is a function of atmospheric temperature. The albedo of the green roof was kept identical to the conventional roof to isolate the effect of evaporative cooling. For each base scenario a series of simulations with combinations of different surface air layer thickness, green roof fraction and varying soil moisture content was carried out and analysed. To define the surface layer thickness the forcing height of the atmosphere was set to 48m, 150m or 300m resulting in a thickness d_{sl} of 28m, 130m and 280m, respectively. The fraction of roof covered by vegetation (f_{G}) was varied between 0% and 100% of b in 25% intervals. Soil moisture content W_{G} took one of the following values between wilting point and field capacity in [kgm^{-2}]: $[56, 58, 60, 62, 65, 65.5, 66, 69, 74, 80, 88, 99, 103]$. By varying the soil moisture content the latent heat flux can be influenced while not directly affecting any of the other fluxes. For a soil moisture content at the wilting point or below no evaporation takes place, while the maximum evaporation is reached at field capacity. In all the

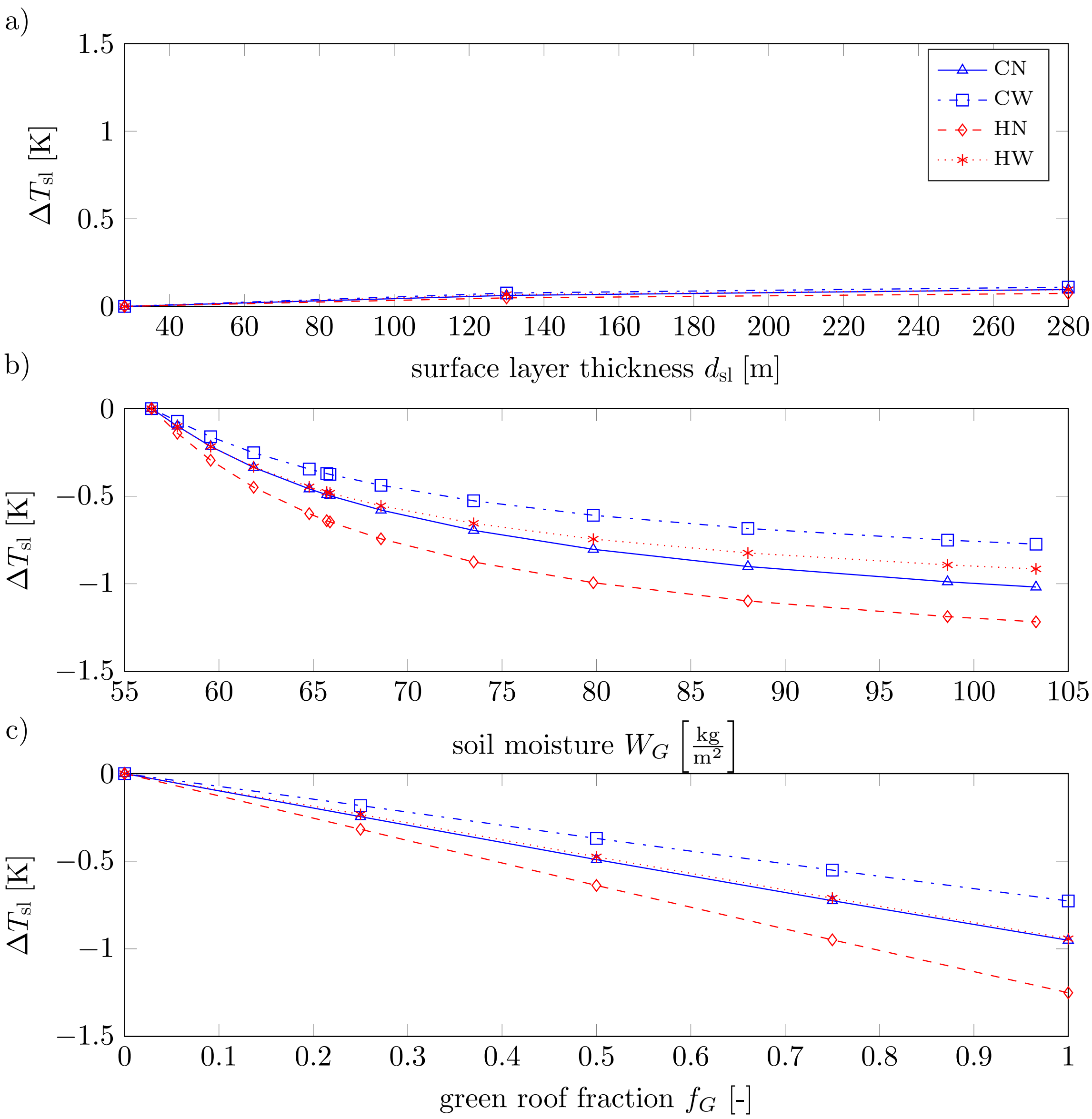

Figure 2.2: (a) Change of surface layer temperature (ΔT_{sl}) depending on surface layer thickness d_{sl}, (b) soil moisture content W_G and (c) green roof fraction f_{G}.

simulations no runoff was assumed and W_{G} was held constant by supplying water (f_{W}) equal to the evaporation rate (E_{G}). The additional water supply essentially is a forcing on the system, which allows for a steady state to be attained. Thus, (2.8) simplifies to

$$0 = f_{\mathrm{w}} - E_{\mathrm{G}}, \tag{2.14}$$

Figure 2.2a shows the influence of the surface layer thickness on the surface layer temperature ΔT_{sl} for the four scenarios with a green roof fraction of 50% and soil moisture content of 65kgm^{-2}. We find that in general the effect on ΔT_{sl} is very weak

and the curves flatten for increasing layer thickness. A thicker surface layer leads to slightly higher temperatures. This is the result of the resistances depending on the surface layer thickness. The resistance between the surface layer and the atmosphere r_{sl} depends more strongly on the thickness than the resistance between the surface layer and the roof r_{R}. Thus, a thicker layer reduces the flux between the surface layer and the atmosphere more than the flux between the roof and the surface layer.
Figure 2.2b shows the change in surface layer temperature depending on the soil moisture content. The surface layer thickness is 130m and the green roof fraction is 50%. We can see that the temperature reduction at the wilting point is 0 since no evaporation occurs. Increasing soil moisture leads to more cooling, but with a decreasing rate. The geometry with narrow roads also has wider buildings as can be seen in Table 2.1; the same green roof fraction therefore corresponds to a larger vegetated area. The cases **CN** and **HN** thus show a stronger temperature reduction for a given soil moisture content. Temperature reduction is also larger in a hotter climate.
Figure 2.2c shows the change in surface layer temperature depending on the fraction of roofs covered with vegetation. The surface layer thickness is 130m and the soil moisture content was 65kgm^{-2}. We observe a linear relationship between temperature reduction and green roof fraction. Again, hotter conditions lead to a stronger temperature reduction for a given green roof fraction and the geometries with narrower streets offer more roof area, leading to more cooling. These two effects coincidentally lead to an almost identical graph for the **HW** and **CN** case.

By plotting surface layer air temperature reduction against the average latent heat flux it is possible to capture all effects shown in Figure 2.2 in a single plot. Here the latent heat flux is averaged over the entire horizontal area to remove the effect of the different green roof fractions and roof sizes, i.e.

$$\overline{E} = a_{\mathrm{G}} E_{\mathrm{G}}. \tag{2.15}$$

Figure 2.3a shows a collapse of all the data on a single line of the form

$$\Delta T_{\mathrm{sl}} = e_{\mathrm{E}} \cdot \Delta \overline{E}, \tag{2.16}$$

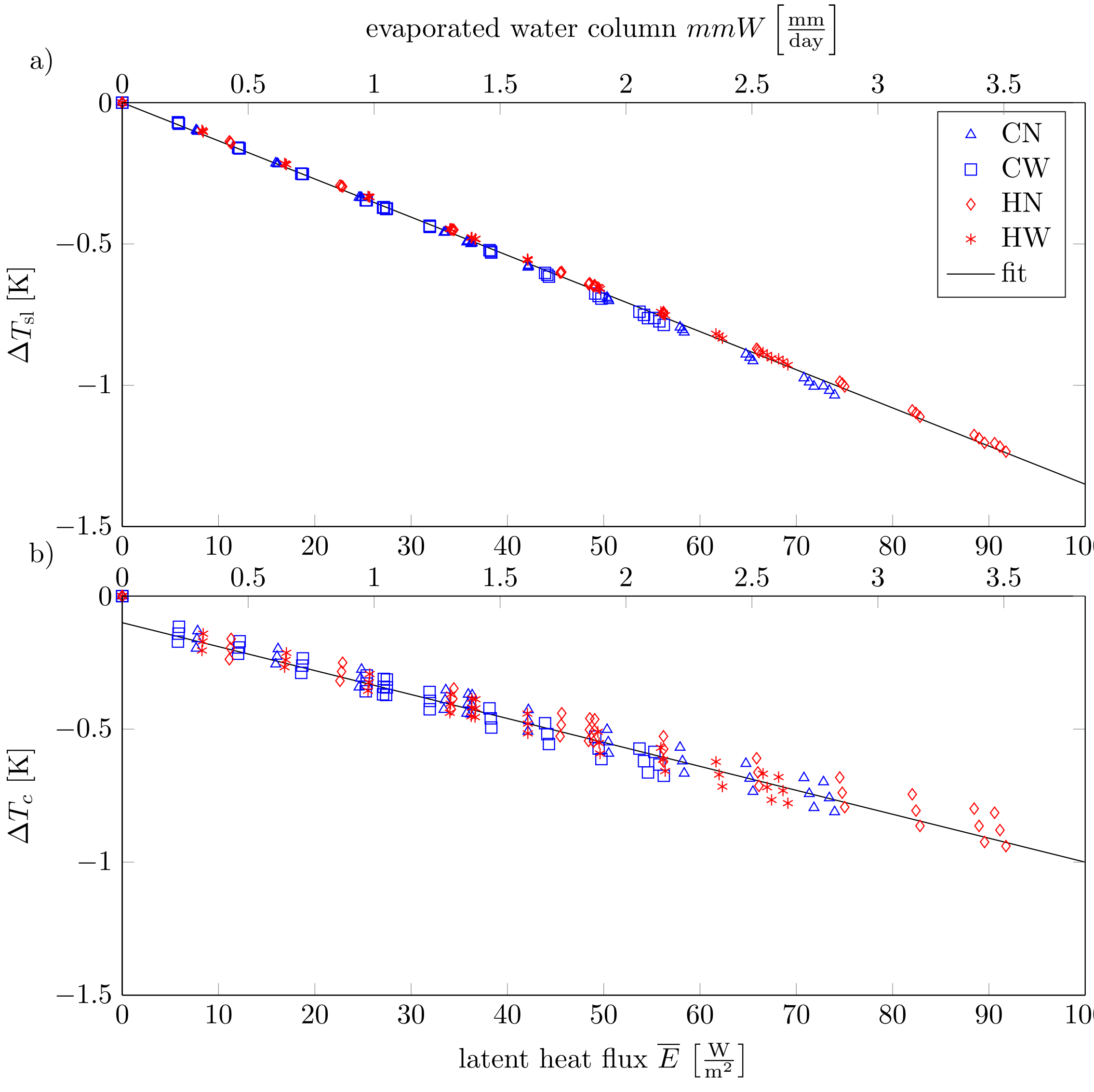

Figure 2.3: (a) Change of the surface layer air temperature and (b) canyon temperature depending on latent heat flux from vegetated green roofs. Daily evaporated water column corresponding to the latent heat flux on top x-axis.

where the gradient e_E is the evaporative cooling potential with

$$e_\mathrm{E} = -0.014\mathrm{Km}^2\mathrm{W}^{-1} \tag{2.17}$$

for all scenarios. Alternatively, the relationship 2.16 can be expressed as

$$\Delta T_\mathrm{sl} = e_\mathrm{W} \cdot mmW \tag{2.18}$$

where mmW is the daily evaporated water column,

$$mmW = \frac{\overline{E}}{L_\mathrm{v}\rho_w}\frac{86400\mathrm{s}}{\mathrm{day}}, \tag{2.19}$$

with the density of water $\rho_\mathrm{w} = 1000\mathrm{kg\,m}^{-3}$. Equation 2.19 converts the energy flux $\overline{E}$ into the water flux mmW with units $\mathrm{mm\,day}^{-1}$, which is commonly used for precipitation measurements. Equation 2.18 thus facilitates relating the potential cooling to the available precipitation. The resulting gradient is

$$e_\mathrm{W} = -0.35\mathrm{Kday\,mm}^{-1}. \tag{2.20}$$

For the remainder of this section e will always be used in the SI form (e_E). A previous study by Li et al. (2014) found a comparable relationship between daily mean near surface temperatures and domain average daily mean latent heat flux of -0.018K $\mathrm{m}^2\,\mathrm{W}^{-1}$ and for daily maximum near surface temperatures -0.022K $\mathrm{m}^2\,\mathrm{W}^{-1}$ by using the meso-scale atmospheric model WRF-PUCM to study the impact of green roofs on the Baltimore-Washington metropolitan area. Equation (2.16) allows us to assess the maximal cooling we can achieve with the available precipitation for the given climate or we can estimate the effect additional watering would have on green roof performance, with an upper limit given by green roof area and climate.

Figure 2.3b shows the temperature reduction inside the canyon. The slope is somewhat smaller at -0.01K $\mathrm{m}^2\,\mathrm{W}^{-1}$. This is expected since green roofs only interact with the canyon via the surface layer and not directly. Since the resistance between canyon and surface layer depends on the surface layer thickness, the corresponding three cases can clearly be distinguished. We can also observe a deviation from the linear behaviour for very small latent heat fluxes. Due to the indirect interaction of the canyon and the green roof we will continue to focus on surface layer temperature.

2.3.2 Diurnal cycle

We compare the steady state results to an unsteady case with an idealised diurnal atmospheric temperature and radiation cycles. The forcing corresponds to the **HW** case with a surface layer thickness of 300m and a green roof fraction of 50%. Daily shortwave radiation is prescribed as $K = K_0 \cdot \max(\sin(\frac{2\pi(t-4\mathrm{h})}{32\mathrm{h}}), 0)$, truncated and repeated after 24h leading to 16h daylight per day. Radiation was set to zero during night time resulting in a daily mean of 520W m^{-2}. The atmospheric temperature followed the same profile, with constant 293K during the night and a daytime mean of 305K. The resulting surface layer temperatures are shown in the Figure 2.4a.

By changing the soil moisture content we can reproduce Figure 2.3 for daily mean temperatures and maximum temperatures. The daily mean temperatures are the average over the entire day and the maximum temperatures are the peak surface layer temperatures that occur around 16:00 in the afternoon. Figure 2.4b reveals a linear behaviour for both mean and maximum temperatures even under unsteady conditions and confirms the assumption that the effect on mean temperature -0.014K m^2 W^{-1} is lower than on maximum temperatures -0.021K m^2 W^{-1}. Note that the effect on mean temperature in the unsteady case is very close to the findings for a steady state (shown as dashed line), it is thus assumed that the steady state case can be used as an approximation of daily mean quantities. While the choice of daily mean latent heat flux or evaporated water column is convenient for comparison with available precipitation it is not ideal to examine temperature extremes. The temperature maximum is a daytime phenomenon (under hot summer conditions) and in this idealised case the day is 16h (t_d) and night 8h long. Since evapotranspiration at night is minimal, mean daytime evaporation is approximately 24h/16h$\cdot\overline{E}$ and we indeed find

$$\Delta T_\mathrm{sl,max} \approx e_\mathrm{E} \cdot \frac{24h}{t_\mathrm{d}} \cdot \Delta\overline{E}. \tag{2.21}$$

2.3.3 Methods of water supply

So far the soil moisture W_G was held constant by supplying water at a rate f_W equal to the evaporation rate E_G during all the simulations, which is a necessary condition to reach a steady state. In this section, the sensitivity on the method of water supply is examined, namely:

a)

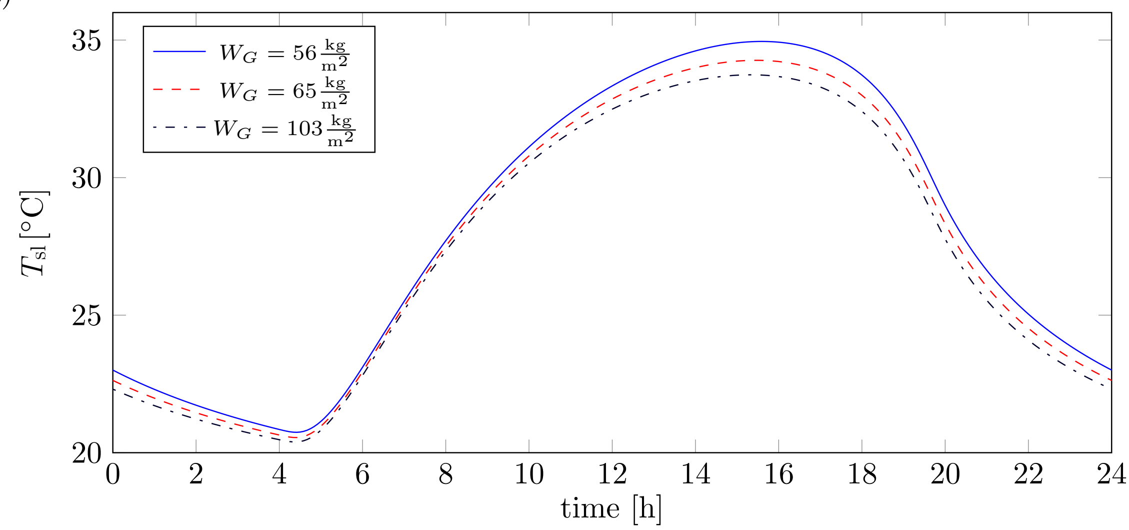

b)

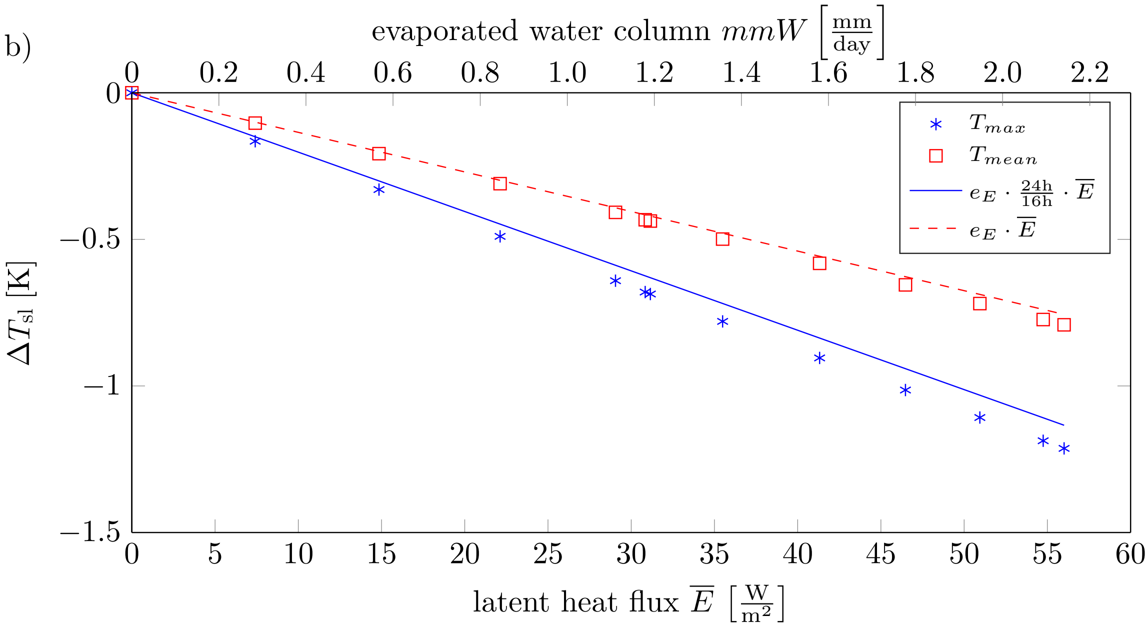

Figure 2.4: a) Diurnal cycle of surface layer temperature for the **HW** case for three different soil moisture contents and b) reduction of daily mean and maximum temperature due to latent heat flux from green roofs (bottom).

1. No water supply, soil moisture slowly depleting
2. Using a time series of actual rainfall as forcing
3. Watering for 30min in the morning
4. Constant watering throughout the day, drip irrigation.

The time series of the water supply can be seen in Figure 2.5a. The rainfall data has been collected during three summer days of the CAPITOUL experiment in Toulouse, France (Masson et al., 2008) and amounts to 10.4mm over the three days. The total water supplied by constant irrigation is 6.5mm and by morning irrigation 4.9mm over three days, respectively. The geometry and diurnal forcing used were identical to the unsteady case in section 2.3.2 and different evaporation rates were achieved by varying initial soil moisture.

From the results shown in Figure 2.5b it is clear that the slope e_E is robust and does not significantly depend on the chosen supply method. The "mean" quantities are averaged over the third day. $\overline{E}$ and $\Delta T_{\mathrm{sl},mean}$ are thus the 1-day averages of the differences between a scenario with evaporation and one without. The temperature reduction $\Delta T_{\mathrm{sl},max}$ is the difference between the daily maximum temperature of scenarios with and without evaporation during the third day. It is important to consider that when plotting ΔT vs E, excess water does not show up in the graph, since it runs off and does not evaporate. The water supply to green roofs in reality would thus need to be larger than the evaporated water column suggests, since runoff can usually not be completely avoided. It is thus recommended to choose drip irrigation to avoid runoff of excess water.

2.4 A simple estimate of the evaporative cooling potential

To better understand what processes influence the evaporative cooling potential e and to estimate the value without having to solve the set of differential equations numerically, we derive an algebraic expression for e. The MTEB model is a set of ODEs describing the evolution of heat and water reservoirs over time. Every differential equation is based on a flux balance. The exchange processes between the reservoirs

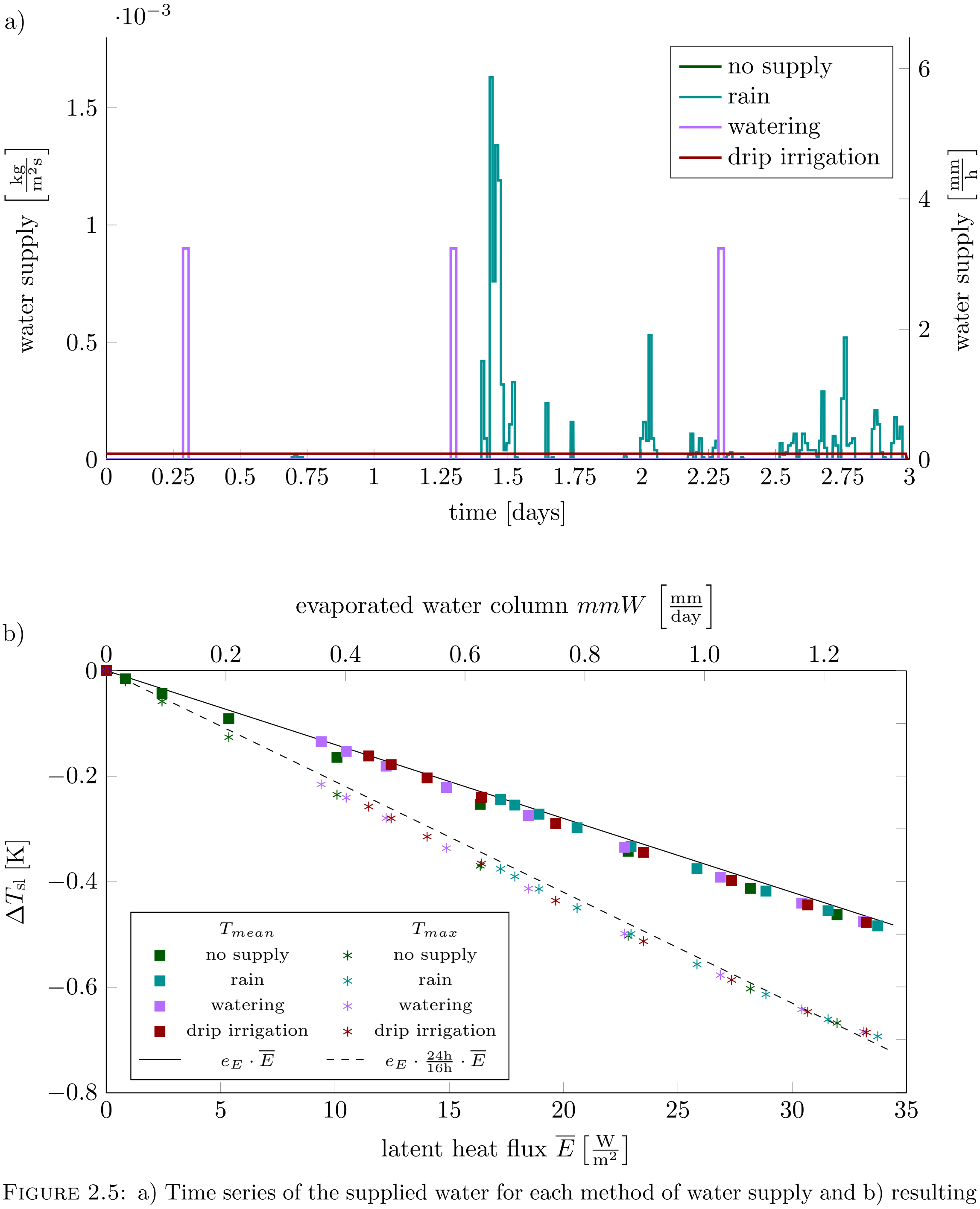

FIGURE 2.5: a) Time series of the supplied water for each method of water supply and b) resulting change of daily mean and maxima surface layer air temperatures depending on latent heat flux from vegetated green roofs for each method. Daily evaporated water column corresponding to the latent heat flux on top x-axis.

and between the reservoirs and the atmosphere are described by various functions depending on the current state of the system, $\boldsymbol{x} = [T_\mathrm{R}, T_\mathrm{w}, T_\mathrm{R}, q_\mathrm{sl}, T_\mathrm{sl}, T_\mathrm{G}, W_\mathrm{G}]^T$. A very general way to express the MTEB model is then

$$C\frac{d\boldsymbol{x}}{dt} = \boldsymbol{g}(\boldsymbol{x}) + \boldsymbol{f} \tag{2.22}$$

where C is a diagonal matrix containing the heat capacities. The external forcing ($\boldsymbol{f}$) on the system, notably the solar shortwave radiation and water supply (f_w) is given by

$$\boldsymbol{f} = [K_\mathrm{R}, K_\mathrm{w}, K_\mathrm{R}, 0, 0, K_\mathrm{G}, f_\mathrm{w}]^T . \tag{2.23}$$

The 7×1 column vector $\boldsymbol{g} = (g_1(\boldsymbol{x}), g_2(\boldsymbol{x}), ...)$ contains the energy and water balances (equations 2.1, 2.2, 2.6, 2.7, 2.8) and defines the evolution of x_i with time. To analyse the reaction of this system to a perturbation from a reference state $\boldsymbol{x}_0$ we perform a multivariate Taylor series expansion with result

$$C\frac{d\boldsymbol{x}}{dt} = \boldsymbol{g}(\boldsymbol{x_0}) + J\boldsymbol{\epsilon} + \boldsymbol{f} + \mathcal{O}\left(\boldsymbol{\epsilon}^2\right), \tag{2.24}$$

where $\boldsymbol{\epsilon} = \boldsymbol{x} - \boldsymbol{x_0}$ is the deviation from the reference state and $J_{ij} = \frac{\partial g_i}{\partial x_j}|_{\boldsymbol{x}_0}$ is the Jacobian given by

$$J = \begin{bmatrix} J_{11} & 0 & 0 & 0 & J_{15} & 0 & 0 \\ 0 & J_{22} & J_{23} & 0 & J_{25} & 0 & 0 \\ 0 & J_{32} & J_{33} & 0 & J_{35} & 0 & 0 \\ 0 & 0 & 0 & J_{44} & J_{45} & J_{46} & J_{47} \\ J_{51} & J_{52} & J_{53} & 0 & J_{55} & J_{56} & 0 \\ 0 & 0 & 0 & J_{64} & J_{65} & J_{66} & J_{67} \\ 0 & 0 & 0 & J_{74} & J_{75} & J_{76} & J_{77} \end{bmatrix}, \tag{2.25}$$

with e.g. $J_{11} = \frac{\partial g_1}{\partial T_\mathrm{R}}$ and $g_1(T_\mathrm{R}) = L_\mathrm{R}(T_\mathrm{R}) - H_\mathrm{R}(T_\mathrm{R}) - G_\mathrm{R}(T_\mathrm{R})$ (from (2.1)). Thus the change of the roof temperature with time depends on the roof temperature itself via functions describing the longwave radiation, sensible heat flux and ground heat flux. To keep the Taylor series tractable we ignore the dependence of resistances upon $\boldsymbol{x}$.

We are interested in a change in forcing $\boldsymbol{f} = \boldsymbol{f_0} + \boldsymbol{f_\delta}$, where $\boldsymbol{f_\delta} = [0, 0, 0, 0, 0, 0, \Delta f_W]^T$ contains a change in water supply (in W m^{-2}). Here, $\boldsymbol{f} = \boldsymbol{f_0}$ corresponds to the steady state forcing in the reference state for which $\frac{d\boldsymbol{x}}{dt} = 0$ and $\boldsymbol{\epsilon} = 0$; hence $\boldsymbol{g}(\boldsymbol{x_0}) = -\boldsymbol{f_0}$, implying that the fluxes in the system balance the external forcing in the steady state. Thus, it follows from (2.24) that the modified steady state of the system is governed by

$$\boldsymbol{\epsilon} = -J^{-1}\boldsymbol{f_\delta}. \tag{2.26}$$

Written out and making use of the fact that $\boldsymbol{f_\delta}$ contains zeros except for the last entry, this relation reads

$$\begin{bmatrix} \Delta T_{\mathrm{R}} \\ \Delta T_{\mathrm{w}} \\ \Delta T_{\mathrm{r}} \\ \Delta q_{\mathrm{sl}} \\ \Delta T_{\mathrm{sl}} \\ \Delta T_{\mathrm{G}} \\ \Delta W_{\mathrm{G}} \end{bmatrix} = - \begin{bmatrix} J^{-1}_{17} \\ J^{-1}_{27} \\ J^{-1}_{37} \\ J^{-1}_{47} \\ J^{-1}_{57} \\ J^{-1}_{67} \\ J^{-1}_{77} \end{bmatrix} \Delta f_{\mathrm{w}}. \tag{2.27}$$

The evaporative cooling potential, e, which links ΔT_{sl} to the domain-averaged latent heat flux $\overline{E} = a_{\mathrm{G}} E_{\mathrm{G}}$ is given by

$$e_E = -J^{-1}_{57} a_G^{-1}, \tag{2.28}$$

making use of (2.14).

The Jacobian J can be obtained readily by making use of symbolic mathematics software such as MAPLE, after which J can be evaluated numerically and then inverted for any reference state. This works for any UEB, as long as the functions $\boldsymbol{g}$ and their derivatives are known. For the **HW** scenario with 50% green roof fraction and 28m surface layer thickness the result is

$$J = \begin{bmatrix} -27.34 & 0 & 0 & 0 & 17.76 & 0 & 0 \\ 0 & -14.1 & 5.45 & 0 & 4.47 & 0 & 0 \\ 0 & 12.9 & -19.3 & 0 & 4.47 & 0 & 0 \\ 0 & 0 & 0 & -96450 & 1.13 & -0.69 & 2.07 \\ 4.44 & 4.47 & 2.23 & 0 & -58.0 & 4.44 & 0 \\ 0 & 0 & 0 & 3122 & 13.22 & -24.3 & -8.30 \\ 0 & 0 & 0 & 3122 & -4.54 & 2.74 & -8.30 \end{bmatrix} \tag{2.29}$$

and

$$J^{-1} = \begin{bmatrix} -38.7 & -7.7 & -3.7 & 0.0 & -13 & -2.2 & 2.2 \\ -1.8 & -102 & -30 & 0.0 & -11 & -1.9 & 1.9 \\ -2.5 & -71 & -73.3 & 0.0 & -12.4 & -2 & 2 \\ 0.0 & 0.0 & 0.0 & -0.01 & 0.0 & 0.0 & -0.0 \\ -3.4 & -12 & -5.7 & 0.0 & -20 & -3.4 & 3.4 \\ -2.2 & -7.8 & -3.8 & 0.0 & -13.6 & -3.9 & 3.9 \\ 1 & 3.9 & 1.9 & -4 & 6.8 & -11 & -11 \end{bmatrix} \times 10^{-3}. \tag{2.30}$$

In this case $-J^{-1}_{57} = -0.0034\mathrm{K\,m^2\,W^{-1}}$. With the given green roof fraction and geometry the green roof makes up 25% of the entire area, and thus $e_E = -J^{-1}_{57}/0.25 = -0.0136\mathrm{K\,m^2\,W^{-1}}$, which is very close to the value of -0.0135 we obtain by solving the ODE numerically.

The approach above, although correct, is neither amenable to hand calculations, nor does it provide insight into physical processes. We thus simplify (2.25) further by assuming that feedback processes can be neglected for small $\boldsymbol{\epsilon}$. Without feedback mechanism it is possible to reduce the number of equations required to determine e_E. A forcing on the soil moisture content W_G will initially only affect E_G, whose derivatives appear in J_{47}, J_{67} and J_{77}. We can thus disregard the conventional roof temperature $T_\mathrm{R} \implies J_{1,\star}$, $T_\mathrm{w} \implies J_{2,\star}$ and $T_\mathrm{r} \implies J_{3,\star}$ entirely. Since we are interested in surface layer temperature and T_sl does not directly depend on q_sl we can also ignore $J_{4,\star}$. Furthermore, without feedback processes only the upper triangular part of this reduced matrix is important. The simplified Jacobian is then given by

$$J_{\mathrm{f}} = \begin{bmatrix} J_{55} & J_{56} & 0 \\ 0 & J_{66} & J_{67} \\ 0 & 0 & J_{77} \end{bmatrix} \tag{2.31}$$

and the simplified system is

$$\boldsymbol{\epsilon}_{\mathrm{f}} = - \begin{bmatrix} \Delta T_{\mathrm{sl}} \\ \Delta T_{\mathrm{G}} \\ \Delta W_{\mathrm{G}} \end{bmatrix} = J_{\mathrm{f}}^{-1} \begin{bmatrix} 0 \\ 0 \\ \Delta f_{\mathrm{w}} \end{bmatrix}. \tag{2.32}$$

Specific to the current problem is that J_{67} and J_{77} are identical by definition, as they both describe the same physical process, namely the evaporation from the green roof which shows up both in the water and in the energy balance. Making use of this inverting J_{f} yields an estimate for e_E given by

$$e_{Ef} = -a_G^{-1} \frac{J_{56}}{J_{55} J_{66}} = -a_G^{-1} \frac{\frac{\partial g_5}{\partial T_{\mathrm{G}}}}{\frac{\partial g_5}{\partial T_{\mathrm{sl}}} \frac{\partial g_6}{\partial T_G}}. \tag{2.33}$$

We can verify that (2.33) corresponds to e_{Ef} by using that under the simplified conditions $e_{Ef} = a_G^{-1} \frac{-J_{56}}{J_{55}} \frac{1}{J_{66}} = a_G^{-1} \frac{\Delta T_{\mathrm{sl}}}{\Delta T_{\mathrm{G}}} \frac{\Delta T_{\mathrm{G}}}{a_G^{-1} \Delta \overline{E}}$, which is indeed the definition of e_E given by (2.16). In (2.33) g_5 describes the evolution of surface layer temperature with time and g_6 describes the evolution of the green roof temperature. The only term in g_5 depending on the green roof temperature is the sensible heat flux from the green roof and thus the numerator of (2.33) consists of a single term. The denominator describes how the temperatures depend on themselves and contains all the terms from the energy budgets Eq. (2.6) and (2.1), without the shortwave radiation. Thus,

$$e_{Ef} = \frac{-a_G^{-1} \frac{\partial H_{\mathrm{G}}}{\partial T_{\mathrm{G}}}}{\left(-\frac{\partial H_{\mathrm{sl}}}{\partial T_{\mathrm{sl}}} + \frac{\partial H_{\mathrm{R}}}{\partial T_{\mathrm{sl}}} + \frac{\partial H_{\mathrm{c}}}{\partial T_{\mathrm{sl}}} + \frac{\partial H_{\mathrm{G}}}{\partial T_{\mathrm{sl}}}\right)\left(\frac{\partial L_{\mathrm{G}}}{\partial T_{\mathrm{G}}} - \frac{\partial H_{\mathrm{G}}}{\partial T_{\mathrm{G}}} - \frac{\partial G_{\mathrm{G}}}{\partial T_{\mathrm{G}}} - \frac{\partial E_{\mathrm{G}}}{\partial T_{\mathrm{G}}}\right)}. \tag{2.34}$$

Most terms in (2.34) are simple to evaluate using (2.3) for sensible and (2.5) for ground heat flux. Longwave radiation follows the Stefan-Boltzman law. Only the term $\frac{\partial E_{\mathrm{G}}}{\partial T_{\mathrm{G}}}$ depends on the model choice and is a lengthy algebraic expression. Specifically, e_{Ef} takes the form

$$e_{Ef} = \frac{-1}{a_{\mathrm{G}}(-4\epsilon\sigma T_{G0}^{3} - \frac{\rho_a c_p}{r_{\mathrm{R}}} - \frac{\lambda_{\mathrm{R}}}{d_{\mathrm{R}}} - \frac{\partial E_{\mathrm{G}}}{\partial T_{\mathrm{G}}})} \frac{\mathcal{P}}{r_{\mathrm{R}}}, \tag{2.35}$$

where $\mathcal{P}$ can be interpreted as a net parallel resistance associated with the surface layer and is given by

$$\frac{1}{\mathcal{P}} = \left(-\frac{1}{r_{\mathrm{sl}}} + \frac{a_{\mathrm{R}}}{r_{\mathrm{R}}} + \frac{a_{\mathrm{c}}}{r_{\mathrm{R}}} \left(\frac{1}{\frac{3r_{\mathrm{R}}}{r_{\mathrm{c}}} + 1} - 1 \right) + \frac{a_{\mathrm{G}}}{r_{\mathrm{R}}} \right). \tag{2.36}$$

The dominant term in (2.35) was found to be r_{sl}^{-1} in our scenarios. This implies that a vastly different stability between the surface layer and the atmosphere could lead to significant changes in e. Yet, the surface layer is usually convective and resistances are low during daytime urban heat island conditions, limiting the actual effect of r_{sl}. Evaluating e_{Es} for the given reference values for the **HW** case results in

$$e_{Ef} = -0.0126 \frac{\mathrm{Km}^2}{\mathrm{W}}. \tag{2.37}$$

This simplified expression (2.34) produces a reasonably good estimate for e compared to the full MTEB model and can be used for any other chosen formulations of energy fluxes in other UEB models or other tools to assess the urban climate. The evaporative cooling potential can thus be derived without having to resort to complicated modelling.

2.5 Discussion

The evaporative cooling potential is a useful tool for city planners to get a rough first order estimate of how much cooling green roofs can provide. Indeed, we can use e_{w} to estimate the possible cooling from green roofs in a city by comparing the daily evaporated water column to the mean daily precipitation in that city. For example, London, with a mean summer precipitation of about 1.5mm day^{-1} (UK Met Office, 2018), can achieve an average surface layer temperature reduction of 0.4K if all the water above urban areas could be retained and evaporated. Without additional watering the outdoor cooling effect of green roofs in London will thus be rather small.

However, the effect on daily maximum temperatures is larger and during very hot days small temperature reductions can have a significant influence on health (Kovats & Hajat, 2008, Luber & McGeehin, 2008).

The small amount of precipitation generally available during hot periods in mid-latitudes indicates that neither the precise climate nor urban geometry are expected to be the limiting factors in the cooling potential of green roofs and e is therefore expected to be quite universal. Water availability appears to be the limiting factor. Increasing the area of green roofs to retain more water is a possible way to achieve more cooling. Yet, when capturing precipitation by other means (e.g. rain gutters) and using it to water green roofs, relatively small green roof fractions can achieve the same amount of cooling.

Most of human activities take place inside the urban canyon and it can thus be argued that the effect of green roofs on canyon air temperatures is of greater significance than on surface air layer. Green roofs appear to be an inefficient tool to reduce canyon air temperature directly. Other blue-green infrastructure like green walls may have a larger temperature impact. However, anthropogenic heat sources have not been considered in this study. Indeed, HVAC (heating, ventilation and air conditioning) units are often installed on walls and produce large amounts of heat inside the canyons. Green roofs lead to cooler roof temperatures, and thus reduce the heat flux into the indoor environment and could therefore indirectly influence the canyon air temperatures significantly. There are further limitations to this study that deserve detailed investigation, notably the effect of heterogeneous geometry and plant albedo. Further research is also needed to assess other green infrastructure strategies like e.g. green walls, swales and parks.

3
Urban Large Eddy Simulation

3.1 Introduction

In Chapter 2 Urban Energy Balance modelling was used to predict the effect of green roofs under idealised topographic and atmospheric conditions. While this method can indeed be very useful to obtain information about large scale effects of blue-green solutions, a different approach has to be taken to study smaller scale features and local effects. One of the defining aspects of this problem is that on smaller scales the turbulent nature of the atmosphere and the details of the urban form are of great importance. Turbulence is a major contributor to fluxes of momentum, energy, moisture and other scalar quantities. Turbulence on the other hand is very heterogeneous and depends strongly on the local morphology and temperature distribution. The review article by Barlow (2014) gives a clear overview of the current understanding of the urban boundary layer, showing that especially buoyancy effects are still poorly understood.

Simulating urban flow requires solving the Navier-Stokes equations, which will be presented in section 3.2. This can only be done numerically, given the nonlinearities in the governing equations. In general, the Reynolds Number (Re) of the atmosphere is extremely high and current model resolution cannot capture all length scales of the turbulent air (Sagaut, 2000). For this reason, large eddy simulation (LES) is used in this thesis, which solves the equations of motion on a computational grid fine enough to capture the energetically dominant part of the turbulent spectrum, i.e. large eddies, while smaller eddies are parameterised. For the simulation of the urban flow a modified version of the Dutch Atmospheric Large Eddy Simulation tool (DALES Nieuwstadt & Brost, 1986, Cuijpers & Duynkerke, 1993, Heus et al., 2010), which has been used to study atmospheric processes for over 20 years, is employed. Recently DALES was extended with an immersed boundary method to simulate obstacles in the flow and study dispersion of pollutants in an urban environment (Tomas et al., 2015, 2016). This code formed the starting point for this dissertation. However, in the process of Tomas' work some essential features for atmospheric studies, most notably moist thermodynamic processes were removed. Thus, the missing physics were first reintroduced based on the standard DALES version (Ouwersloot, 2017). In sections 3.2 - 3.4 the numerics of DALES are introduced while from section 3.5 onwards my modification to the model are documented; namely the treatment of fluxes of momentum, temperature and water from the ground and the immersed boundaries.

3.2 Governing equations

The governing equations solved in DALES are within the Boussinesq approximation:

$$\frac{\partial \tilde{u}_{\mathrm{i}}}{\partial x_{\mathrm{i}}} = 0, \tag{3.1}$$

$$\frac{\partial \tilde{u}_{\mathrm{i}}}{\partial t} = -\frac{\partial \tilde{u}_{\mathrm{i}}\tilde{u}_{\mathrm{j}}}{\partial x_{\mathrm{j}}} - \frac{\partial \pi}{\partial x_{\mathrm{i}}} + \frac{g}{\theta_0}\tilde{\theta}_{\mathrm{v}}\delta_{\mathrm{i}3} + F_{\mathrm{i}} - \frac{\partial \tau_{\mathrm{ij}}}{\partial x_{\mathrm{j}}}, \tag{3.2}$$

$$\frac{\partial \tilde{\varphi}}{\partial t} = -\frac{\partial \tilde{u}_{\mathrm{j}}\tilde{\varphi}}{\partial x_{\mathrm{j}}} - \frac{\partial R_{\varphi,\mathrm{j}}}{\partial x_{\mathrm{j}}} + S_{\varphi}. \tag{3.3}$$

Here u_i is the component of the velocity vector along the base vector x_i. Time is denoted as t. The modified pressure is $\pi = \frac{\tilde{p}}{\rho_0} + \frac{2}{3}e$, where p is the pressure, ρ is the density of air and e is the subfilter-scale turbulence kinetic energy. Denoted by θ_v is the liquid water virtual potential temperature, δ_{ij} is the Kronecker delta, F_{i} represents other forcings and τ is the deviatoric part of the subfilter momentum flux. The variable φ can represent humidity, temperature, particulates or chemical species. The subfilter-scale scalar fluxes and scalar sources/sinks are R_φ and S_φ, respectively. Where multiple indices (i, j) appear summation following Einstein

notation is implied. The tildes denote spatially filtered mean variables. Filtering in DALES is implicit: the grid itself acts as the low-pass filter.
The total water content in the air (q_t) consists of specific humidity (q) and liquid water (q_l):

$$q_t = q + q_l \tag{3.4}$$

To calculate the buoyancy and the vertical acceleration virtual potential temperature θ_v is used. The virtual potential temperature can be approximated following Emanuel (1994):

$$\theta_v = \theta \left(1 - \left(1 - \frac{R_v}{R_d}\right) q_t - \frac{R_v}{R_d} q_l\right), \tag{3.5}$$

with

$$\theta = T\Pi^{-1}, \tag{3.6}$$

$$\Pi = \left(\frac{p}{p_0}\right)^{\frac{R_d}{c_d}}, \tag{3.7}$$

where θ is the potential temperature, Π is the Exner function, c_d is the heat capacity of dry air, R_d is the gas constant for dry air and R_v is the gas constant for water vapour. The subfilter stresses are modelled as

$$\tau_{ij} = -\mathcal{K}_m \left(\frac{\partial \tilde{u}_i}{\partial x_j} + \frac{\partial \tilde{u}_j}{\partial x_i}\right), \tag{3.8}$$

$$R_{\varphi,j} = -\mathcal{K}_h \frac{\partial \tilde{\varphi}}{\partial x_j} \tag{3.9}$$

where $\mathcal{K}_m$ represents the eddy viscosity and $\mathcal{K}_h$ the eddy diffusivity. Various sub-grid models are available in DALES to determine $\mathcal{K}_m$ and $\mathcal{K}_h$. Throughout this study the Vreman subgrid-scale model (Vreman, 2004) is used. The Vreman model is of similar complexity as the commonly used Smagorinsky model (Smagorinsky, 1963), but it behaves better in near-wall regions. The eddy viscosity is expressed as:

$$\mathcal{K}_m = C_\nu \sqrt{\frac{B_\beta}{A_{ij} A_{ij}}}, \tag{3.10}$$

where $C_\nu = 2.5C_\mathrm{s}^2 = 0.07$ is a constant model parameter related to the Smagorinsky constant C_s. The matrix A contains the derivatives of the velocity field.

$$A_\mathrm{ij} = \frac{\partial \tilde{u}_\mathrm{j}}{\partial x_\mathrm{i}}, \tag{3.11}$$

and B_β is given by

$$B_\beta = \beta_{11}\beta_{22} - \beta_{12}^2 + \beta_{11}\beta_{33} - \beta_{13}^2 + \beta_{22}\beta_{33} - \beta_{23}^2, \tag{3.12}$$

$$\beta_\mathrm{ij} = \Delta_\mathrm{m}^2 A_\mathrm{mi} A_\mathrm{mj}. \tag{3.13}$$

Explicitly this is:

$$\beta_{11} = \Delta^2 \left[\left(\frac{\partial \tilde{u}}{\partial x}\right)^2 + \left(\frac{\partial \tilde{u}}{\partial y}\right)^2 + \left(\frac{\partial \tilde{u}}{\partial z}\right)^2 \right], \tag{3.14}$$

$$\beta_{12} = \Delta^2 \left[\left(\frac{\partial \tilde{u}}{\partial x}\right)\left(\frac{\partial \tilde{v}}{\partial x}\right) + \left(\frac{\partial \tilde{u}}{\partial y}\right)\left(\frac{\partial \tilde{v}}{\partial y}\right) + \left(\frac{\partial \tilde{u}}{\partial z}\right)\left(\frac{\partial \tilde{v}}{\partial z}\right) \right], \tag{3.15}$$

$$\beta_{13} = \Delta^2 \left[\left(\frac{\partial \tilde{u}}{\partial x}\right)\left(\frac{\partial \tilde{w}}{\partial x}\right) + \left(\frac{\partial \tilde{u}}{\partial y}\right)\left(\frac{\partial \tilde{w}}{\partial y}\right) + \left(\frac{\partial \tilde{u}}{\partial z}\right)\left(\frac{\partial \tilde{w}}{\partial z}\right) \right], \tag{3.16}$$

$$\beta_{22} = \Delta^2 \left[\left(\frac{\partial \tilde{v}}{\partial x}\right)^2 + \left(\frac{\partial \tilde{v}}{\partial y}\right)^2 + \left(\frac{\partial \tilde{v}}{\partial z}\right)^2 \right], \tag{3.17}$$

$$\beta_{23} = \Delta^2 \left[\left(\frac{\partial \tilde{v}}{\partial x}\right)\left(\frac{\partial \tilde{w}}{\partial x}\right) + \left(\frac{\partial \tilde{v}}{\partial y}\right)\left(\frac{\partial \tilde{w}}{\partial y}\right) + \left(\frac{\partial \tilde{v}}{\partial z}\right)\left(\frac{\partial \tilde{w}}{\partial z}\right) \right], \tag{3.18}$$

$$\beta_{33} = \Delta^2 \left[\left(\frac{\partial \tilde{w}}{\partial x}\right)^2 + \left(\frac{\partial \tilde{w}}{\partial y}\right)^2 + \left(\frac{\partial \tilde{w}}{\partial z}\right)^2 \right]. \tag{3.19}$$

The eddy diffusivity is related to the eddy viscosity via a constant turbulent Prandtl number. The tildes (˜) will be omitted from here on for the rest of the thesis.

3.3 Numerical discretisation

DALES is based on an Arakawa C-grid (Arakawa & Lamb, 1977), see Figure 3.1. Pressure, and scalar concentrations (φ) are defined at cell centres and the three velocity components (u, v, w) are defined at the west side, the south side, and the bottom side of the grid cells, respectively. Numerical advection is calculated via a

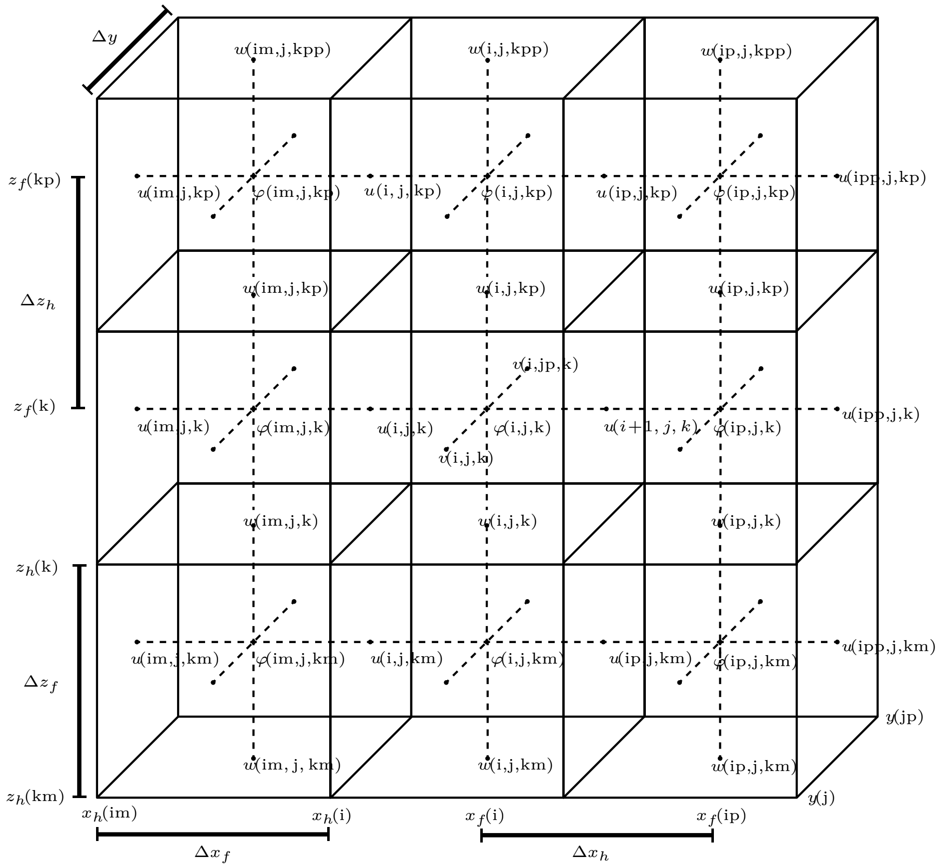

Figure 3.1: Staggered grid used in DALES. The subscripts p and m indicate an increase or decrease of the index by 1, respectively. The three velocity components (u, v, w) are defined at the west side, the south side, and the bottom side of each grid cells, scalar quantities are defined in the cell centre. The grid can be stretched vertically and along x, in which case Δz_f and Δz_h vary with height or Δx_f and Δx_h along x, respectively. Tildes (˜) are omitted.

second order central difference scheme.

$$\frac{\partial u\phi}{\partial x} = \frac{F_{\mathrm{i}+\frac{1}{2}} - F_{\mathrm{i}-\frac{1}{2}}}{\Delta x}, \tag{3.20}$$

$$F_{\mathrm{i}+\frac{1}{2}} = u_{\mathrm{i}+\frac{1}{2}} \frac{\phi_{\mathrm{i}} + \phi_{\mathrm{i}+1}}{2}, \tag{3.21}$$

$$F_{\mathrm{i}-\frac{1}{2}} = u_{\mathrm{i}-\frac{1}{2}} \frac{\phi_{\mathrm{i}} + \phi_{\mathrm{i}-1}}{2} \tag{3.22}$$

where $\phi = u, v, w, \varphi$. Time integration is done by a third order Runge-Kutta scheme, following Wicker & Skamarock (2002). The variable ϕ^{n+1} at $t + \Delta t$ is calculated as follows

$$\phi^{*} = \phi^{n} + \frac{\Delta t}{3} f(\phi^{n}), \tag{3.23}$$

$$\phi^{**} = \phi^{n} + \frac{\Delta t}{2} f(\phi^{*}), \tag{3.24}$$

$$\phi^{n+1} = \phi^{n} + \Delta t f(\phi^{**}), \tag{3.25}$$

where $f(\phi^n)$ is the right-hand side of the corresponding prognostic equation ((3.2), (3.3)). This numerical scheme is stable for a Courant-Friedrichs-Lewy number (Courant et al., 1928)

$$\mathrm{CFL} = \max\left(\mathrm{abs}\left(\frac{u_{\mathrm{i}}\Delta t}{\Delta x_{\mathrm{i}}}\right)\right) < 1.5 \tag{3.26}$$

and a diffusion number (Wesseling, 1996)

$$\delta = \sum_{\mathrm{i}=1}^{3} \frac{K_{\mathrm{m}}\Delta t}{\Delta x_{\mathrm{i}}^{2}} < 0.25. \tag{3.27}$$

DALES is written in Fortran and the code is parallelised using MPI. For the parallelisation the domain is sliced along the y-direction.

3.4 Immersed boundary method

Many problems in fluid dynamics feature the interaction between the fluid and a solid structure. Obstacles inside the flow often require methods like geometry conformal grids, which usually need to be manually created in a cumbersome process. It is common to refine the grid around an obstacle to avoid numerical instabilities caused by a body. This uses less computational resources than reducing the grid spacing in the entire domain, but can still lead to significantly longer simulation times compared to the same problem without obstacle since the pressure field cannot be solved using efficient fast Fourier transform methods.

To circumvent these issues, the immersed boundary method (IBM) was first developed by Peskin (1972). It allows to model complex geometries on a Cartesian grid by adding body force terms to the conservation equations of momentum and scalars. Since its initial development, numerous modifications and refinements to the immersed boundary method have been proposed. Improvements have been made by Mohd-Yusof (1997), Verzicco et al. (2000) and Fadlun et al. (2000). Mittal & Iaccarino (2005) provide an overview. An IBM has recently been implemented in DALES (Tomas et al., 2015) following Pourquie et al. (2009), Verzicco et al. (2000). This method has the advantage of being 2$^{\text{nd}}$-order accurate but is limited to rectangular, grid conformal obstacles. This limits somewhat the application of our model to real cities. The key feature of IBM is the imposition of extra forces on the flow, i.e. the momentum equation. The alignment of the obstacles with the Cartesian mesh allows to apply exact forcings for wall normal velocity components at the boundaries, such that all normal velocities vanish. In conjunction, boundary conditions for tangential velocities and scalars are needed. Tomas used DALES in a DNS-like manner and momentum flux was based on viscous shear stress. Temperature flux was then simply related to the momentum flux by the Prandtl number. The wall function also assumed neutral conditions and smooth walls. This approach is not satisfactory for urban applications. In the following sections the theory and implementation of new wall functions describing momentum, heat and water fluxes are described.

3.5 Wall functions

Nearly all urban surfaces can be considered to be aerodynamically rough. This means that the roughness elements on a surface are much larger than the thickness of the viscous sublayer which is adjacent to every interface between a fluid and a smooth surface. Mean turbulent quantities can thus vary drastically close to walls and processes near the wall cannot be resolved on the grid and therefore need to be modelled; these models typically take the form of wall functions. In this context and throughout chapter 3 any solid boundary is called a wall, not only vertical structures.

Classically in computational fluid dynamics wall functions are used to describe the resistance to momentum and heat transport through the very thin boundary layer in a turbulent flow, that cannot be resolved on the grid. In our studies of green infrastructure, the effect heat and moisture exchange is of particular interest, and wall functions are needed that describe the scalar and momentum exchanges at horizontal and vertical surfaces. Processes close to vertical walls are qualitatively different from horizontal walls, particularly in presence of buoyancy (e.g. Hölling & Herwig, 2005). However, vertical walls are commonly treated the same way as horizontal walls, namely the formation of a constant stress layer with logarithmic wind profile is assumed. This is due to the lack of established alternatives. Currently available wall functions for LES include for example Parente et al. (2011) for neutral conditions, Craft et al. (2006) and McDermott et al. (2017).
The goal of this section is to obtain a description of momentum flux (u_*^2), temperature flux ($\theta_{\mathrm{v}*} u_*$) and moisture flux ($q_* u_*$) at the walls given the tangential velocities and the temperature and humidity difference between the wall and the first fluid cell. On surfaces there is no mean perpendicular wind velocity and the fluxes are purely turbulent, i.e.:

$$u_*^2 = \left.\overline{u'_{\mathrm{P}} U'_{\mathrm{T}}}\right|_s , \tag{3.28}$$

$$\theta_{\mathrm{v}*} u_* = \left.\overline{u'_{\mathrm{P}} \theta'_{\mathrm{v}}}\right|_s , \tag{3.29}$$

$$q_* u_* = \left.\overline{u'_{\mathrm{P}} q'}\right|_s , \tag{3.30}$$

where U_{T} is the tangential wind speed and u_{P} is the velocity component perpendicular to the wall.

In what follows the selection and implementation of wall functions that are based on Dirichlet boundary conditions will be described; as for urban applications boundary conditions with given scalar values, as opposed to given fluxes, are better suited. Generally temperature data is much more readily available since it can be acquired from direct measurements and remote sensing observations.

A review of Monin-Obukhov similarity theory For atmospheric flow wall functions on horizontal surfaces are commonly based on similarity laws determined by

Buckingham Π analysis. Such similarity laws for the surface layer have been known since the fundamental paper of Obukhov (1946) and subsequent work together with A. Monin (Monin & Obukhov, 1954). Following Monin-Obukhov similarity theory (MOST) mean vertical gradients and turbulent characteristics in the stationary and horizontally homogeneous surface layer can only depend upon the surface stress, represented by the friction velocity $u_* = (\tau/\rho)^{1/2}$ [m s^{-1}], kinematic vertical heat flux $Q_0 = \rho c_\mathrm{p} \overline{w'\theta'_\mathrm{v}}$ [W m^{-2}], the buoyancy parameter $g/\overline{\theta_\mathrm{v}}$ [m s^{-2} K^{-1}] and the height above the surface z [m] (Businger et al., 1971). According to the Buckingham Π theorem a single dimensionless parameter can be formed from this set of variables, traditionally defined as

$$\zeta = \frac{z}{\hat{L}} = \frac{-\kappa g \overline{w'\theta'_\mathrm{v}} z}{\overline{\theta_\mathrm{v}} u_*^3} \qquad [-], \tag{3.31}$$

where

$$\hat{L} = \frac{-\overline{\theta} u_*^3}{\kappa g \overline{w'\theta'_\mathrm{v}}} \qquad [\mathrm{m}], \tag{3.32}$$

is the Obukhov length, g is the Earth's gravity [m s^{-2}] and $\kappa = 0.41$ is the von Kármán constant. Here the Obukhov length $\hat{L}$ signifies the height at which buoyancy production and shear production are of equal strength. The sign of $\hat{L}$ depends on the atmospheric stability. During stable stratification $\hat{L} > 0$, while during unstable stratification $\hat{L} < 0$. The Obukhov length becomes infinite in the limit of neutral stratification since $\overline{w'\theta'_\mathrm{v}} = 0$. All normalised quantities, like the dimensionless wind shear (ϕ_m) and dimensionless temperature gradient (ϕ_h) must thus be a universal function of ζ:

$$\phi_\mathrm{m}(\zeta) = \frac{\kappa z}{u_*} \frac{\partial u}{\partial z}, \tag{3.33}$$

$$\phi_\mathrm{h}(\zeta) = \frac{\kappa z}{\theta_{\mathrm{v}*}} \frac{\partial \theta_\mathrm{v}}{\partial z}, \tag{3.34}$$

where $\theta_{\mathrm{v}*} = -\overline{w'\theta'_\mathrm{v}}/u_*$ is the characteristic temperature. The equations (3.33) and (3.34) can be integrated following Panofsky (1963), Paulson (1970), Barker & Baxter

(1975) and Louis (1979) to obtain the velocity and temperature profiles, respectively.

$$u(z) = \frac{u_*}{\kappa}\left[\ln(z/z_0) - \psi_\mathrm{m}(\zeta) + \psi_\mathrm{m}(z_0/\hat{L})\right], \tag{3.35}$$

$$\theta_\mathrm{v}(z) - \theta_{\mathrm{v}\,0} = Pr_\mathrm{T}\frac{\theta_{\mathrm{v}\,*}}{\kappa}\left[\ln(z/z_0) - \psi_\mathrm{h}(\zeta) + \psi_\mathrm{h}(z_0/\hat{L})\right], \tag{3.36}$$

with

$$\psi_\mathrm{m}(x) = \int_0^x \frac{1-\phi_\mathrm{m}(\zeta')}{\zeta'}d\zeta', \tag{3.37}$$

$$\psi_\mathrm{h}(x) = \int_0^x \frac{1-\phi_\mathrm{h}(\zeta')}{\zeta'}d\zeta'. \tag{3.38}$$

The turbulent Prandtl number is $Pr_\mathrm{T} = 0.71$. The aerodynamic roughness length z_0 [m] can be understood as the height where the mean wind velocity is zero. It is noteworthy that z_0 is not equal to the height of the roughness elements, yet determined by them. The potential temperature at z_0 is $\theta_{\mathrm{v}\,0}$ and is assumed to be identical to the ground surface temperature θ_s. The functions ϕ_m and ϕ_h can be determined experimentally (e.g. Businger et al., 1971, Louis, 1979, Holtslag & De Bruin, 1988). By substituting equations (3.35) and (3.36) into equation (3.32) we obtain

$$\hat{L} = \frac{\overline{\theta_\mathrm{v}}u^2}{g\Delta\theta_\mathrm{v}}\frac{\left[\ln(z/z_0) - \psi_\mathrm{h}(\zeta) + \psi_\mathrm{h}(z_0/\hat{L})\right]}{\left[\ln(z/z_0) - \psi_\mathrm{m}(\zeta) + \psi_\mathrm{m}(z_0/\hat{L})\right]^2}, \tag{3.39}$$

giving an implicit relationship between Obukhov-Length $\hat{L}$ and the bulk Richardson number

$$Ri_\mathrm{B} = \frac{gz\Delta\theta_\mathrm{v}}{\overline{\theta_\mathrm{v}}u^2} \qquad [-]. \tag{3.40}$$

We are interested in the eddy fluxes u_*^2 and $\theta_{\mathrm{v}\,*}u_*$. These can be obtained from the profiles by first expressing (3.35) and (3.36) as

$$u(z) = \frac{u_*}{\kappa}\ln(z/z_0)\left[1 - \frac{\psi_\mathrm{m}(\zeta) - \psi_\mathrm{m}(z_0/\hat{L})}{\ln(\frac{z}{z_0})}\right], \tag{3.41}$$

$$\Delta\theta_\mathrm{v} = Pr\frac{\theta_{\mathrm{v}\,*}}{\kappa}\ln(z/z_0)\left[1 - \frac{\psi_\mathrm{h}(\zeta) - \psi_\mathrm{h}(z_0/\hat{L})}{\ln(\frac{z}{z_0})}\right]. \tag{3.42}$$

Rearranging (3.41) for u_* and (3.42) for $\theta_{\mathrm{v}*}$ and multiplying with (3.41) results in

$$u_*^2 = \frac{u^2\kappa^2}{\ln(z/z_0)^2} F_1\left(\frac{z}{z_0}, \hat{L}\right), \tag{3.43}$$

$$\theta_{\mathrm{v}*}u_* = \frac{\kappa\Delta\theta_{\mathrm{v}}}{Pr\ln(z/z_0)} F_2\left(\frac{z}{z_0}, \hat{L}\right) \frac{u\kappa}{\ln(z/z_0)} F_1\left(\frac{z}{z_0}, \hat{L}\right)^{1/2}, \tag{3.44}$$

where F_1 and F_2 are given by

$$F_1 = \left[1 - \frac{\psi_{\mathrm{m}}(\zeta) - \psi_{\mathrm{m}}(z_0/\hat{L})}{\ln(\frac{z}{z_0})}\right]^2, \tag{3.45}$$

$$F_2 = \left[1 - \frac{\psi_{\mathrm{h}}(\zeta) - \psi_{\mathrm{h}}(z_0/\hat{L})}{\ln(\frac{z}{z_0})}\right], \tag{3.46}$$

respectively. We can then use the existing relationship between the bulk Richardson number and the Obukhov length (3.39) to write

$$u_*^2 = u^2 \frac{\kappa^2}{\ln(z/z_0)^2} F_{\mathrm{m}}\left(\frac{z}{z_0}, Ri_B\right), \tag{3.47}$$

$$\theta_{\mathrm{v}*}u_* = u\Delta\theta_{\mathrm{v}} \frac{\kappa^2}{Pr\ln(z/z_0)^2} F_{\mathrm{h}}\left(\frac{z}{z_0}, Ri_B\right). \tag{3.48}$$

The functions F_{m} and F_{h} describe the relationship between the atmospheric temperature and wind profile and the corresponding surface fluxes. It is noteworthy that (3.47) and (3.48) are often written as

$$u_*^2 = C_d u^2, \tag{3.49}$$

$$\theta_{\mathrm{v}*}u_* = C_{\mathrm{h}} u \Delta\theta_{\mathrm{v}}, \tag{3.50}$$

where C_d [-] is the momentum transfer coefficient and C_{h} [-] is the heat transfer coefficient. The parametric functions F_{m} and F_{h} have been approximated by Louis (1979). Louis fitted analytical formulae to calculated values from Businger et al. (1971). The result for stable cases is

$$F_{\mathrm{m}} = F_{\mathrm{h}} = \frac{1}{(1 + b' Ri_{\mathrm{B}})^2}, \tag{3.51}$$

with $b' = 4.7$ and for unstable cases

$$F_\mathrm{i} = 1 - \frac{bRi_\mathrm{B}}{1 + c_\mathrm{i}|Ri_\mathrm{B}|^{1/2}}, \tag{3.52}$$

where $b = 9.4$. The parameter c_i is given by

$$c_\mathrm{i} = d_\mathrm{i} \frac{\kappa^2}{\ln\left(z/z_0\right)^2} b \left(\frac{z}{z_0}\right)^{1/2}, \tag{3.53}$$

with $d_\mathrm{m} = 7.4$ and $d_\mathrm{h} = 5.3$, where $i = m$ for momentum and $i = h$ for heat. Given the temperature and roughness of a surface and the velocity and temperature of the adjacent fluid cell the surface momentum and temperature flux could then be calculated.

Wall roughness for momentum and heat In an urban environment surfaces are generally not dynamically smooth. Protrusions such as window sills and shutters lead to roughness. Momentum transfer has a strong dependence on the form drag introduced by the pressure difference across those obstacles. However, for scalar transport no equivalent principle to pressure exists. In fact, it has been shown (Garratt, 1994) that for rough surfaces scalar transport becomes less efficient compared to momentum transport near the wall. We thus follow the approach of Cai (2012b) and Uno et al. (1995) to use a separate roughness length $z_\mathrm{T} \leq z_0$ for scalars. The wall roughness is often expressed as $\kappa B_\mathrm{h}^{-1} = \ln(z_0/z_\mathrm{T})$ and empirically depends on the roughness Reynolds number Re_* (Garratt, 1994):

$$Re_* = \frac{u_* z_0}{\nu}, \tag{3.54}$$

$$\kappa B_\mathrm{h}^{-1} = 6.2\kappa Re_*^{\frac{1}{4}} - 5. \tag{3.55}$$

Typical values for roughness Reynolds numbers are available in the literature for various surfaces types such as grass (e.g. also in Garratt, 1994).

It is assumed that the temperature at z_T, θ_T, is equal to the actual surface temperature θ_s. This leads to the problem that the temperature at the momentum roughness length z_0, $\theta_{\mathrm{v}\,0}$, is not known anymore and therefore $\Delta\theta_\mathrm{v} = \Delta\theta_0 = \theta_\mathrm{v}(z) - \theta_{\mathrm{v}\,0}$ and Ri_B cannot be evaluated directly. Consequently, additional steps to find $\theta_{\mathrm{v}\,0}$ need to

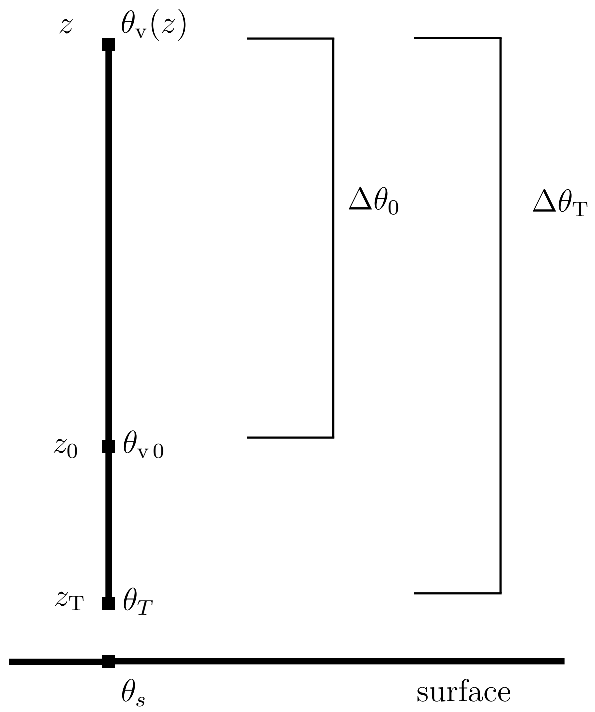

Figure 3.2: Schematic representation of potential temperatures θ and levels needed in the wall function. The surface roughness lengths for momentum and heat are z_0 and $z_{\rm T}$ with the corresponding temperatures $\theta_{\rm v0}$ and $\theta_{\rm T}$, respectively. At a distance z from the wall the temperature is $\theta_{\rm v}(z)$.

be introduced.

3.5.1 Wall function for momentum and temperature

A wall function following the one-step iterative approach of Uno et al. (1995) to calculate the heat and momentum transfer coefficients has been introduced into DALES. This approach has been employed in LES studies before (Cai, 2012b) and is very attractive given the fact that computational costs are low. The function takes the surface temperature ($\theta_{\rm s}$), temperature of the first fluid cell ($\theta_{\rm v}(z)$), wall tangential velocity in the first fluid cell (u) and the distance from the cell centre to the wall (z) as input and returns the momentum and temperature fluxes (u_*^2 and $\theta_{\rm v\,*}u_*$, respectively) with a single iteration. The various temperatures and vertical coordinates used in this scheme can be seen in Fig 3.2. First the bulk Richardson number $Ri_{\rm B\,T}$ (Eq 3.40) can be estimated based on the surface temperature, i.e. we assume $\Delta\theta_{\rm v} = \Delta\theta_{\rm T} = \theta_{\rm v}(z) - \theta_{\rm T}$. The stability functions $F_{\rm m}$ can then be evaluated according to Eq 3.51 or Eq 3.52. We then calculate $Ri_{\mathrm{B}\,0}$ according to

$$M(Ri_B) = Pr \ln\left(\frac{z}{z_0}\right) \frac{\sqrt{F_{\mathrm{m}}(Ri_B)}}{F_{\mathrm{h}}(Ri_B)} \tag{3.56}$$

$$Ri_{\mathrm{B}\,0} = Ri_{\mathrm{B}\,\mathrm{T}} - \frac{Ri_{\mathrm{B}\,\mathrm{T}} Pr A}{Pr A + M(Ri_{\mathrm{B}\,\mathrm{T}})} \tag{3.57}$$

where $A = \ln\left(\frac{z_0}{z_T}\right)$. $Ri_{\mathrm{B}\,0}$ is the estimate for Richardson number based on the temperature at z_0, $\theta_{\mathrm{v}\,0}$. Then F_{m}, F_{h} and M are reevaluated based on $Ri_{\mathrm{B}\,0}$. After obtaining $\Delta\theta_0$ from

$$\Delta\theta_0 = \Delta\theta_T \left[\frac{Pr A}{M(Ri_{\mathrm{B}\,0})} + 1\right]^{-1}, \tag{3.58}$$

the surface fluxes can be calculated using Eq 3.47 & 3.48. The resulting momentum transfer coefficients (C_d) and heat transfer coefficient (C_h) are shown in Figure 3.3 and 3.4, respectively. Figure 3.3 shows the dependence of the bulk transfer coefficient for momentum on the bulk Richardson number (Ri_B), Von Kármán constant, and the ratio between height and roughness height (z/z_0). If the von Kármán constant is chosen to be $\kappa = 0.35$, our implementation matches the original values from Uno et al. (1995). However, it is more generally agreed that κ is close to 0.4 and $\kappa = 0.41$ was chosen in DALES. It is also evident that both C_d and C_h increase for rougher walls (decreasing z/z_0).

This method is used for vertical walls as well, where z and Ri_B are defined perpendicular to the wall. By doing this, the Richardson number loses its context and one must be careful interpreting its values. This approach has been used by Cai (2012a,b) to study differential wall heating in a canyon and they argue that it is a reasonable approximation for forced convection cases. Processes near vertical walls are generally poorly understood and no other adequate wall function could be found in the literature.

3.5.2 Wall function for moisture

The moisture flux from roof and wall facets can be described identically to the heat flux (Eq. 3.36). However, it is not obvious what the moisture difference Δq between the wall and the atmosphere is, because water is usually not available directly on

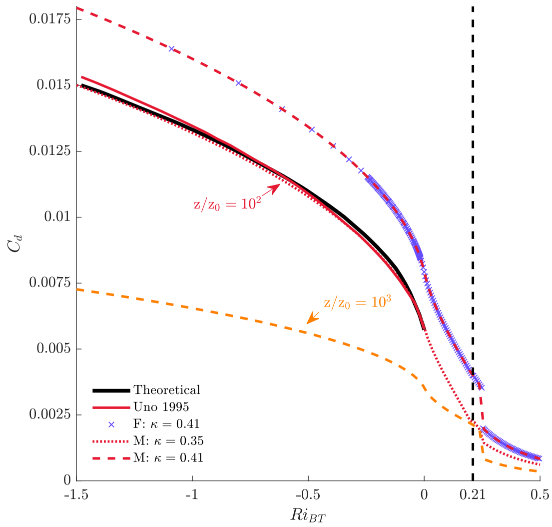

FIGURE 3.3: Bulk transfer coefficient for momentum C_d in terms of the bulk Richardson number Ri_{BT} and roughness length for $z/z_0 = [10^2, 10^3]$ with $z_0/z_T = 7.4$. Values for "Uno 1995" and "Theoretical" are reproduced after Uno et al. (1995). F denotes results from the LES model, and M indicates the use of MATLAB. The critical Richardson number (Ri_{c}) is 0.21.

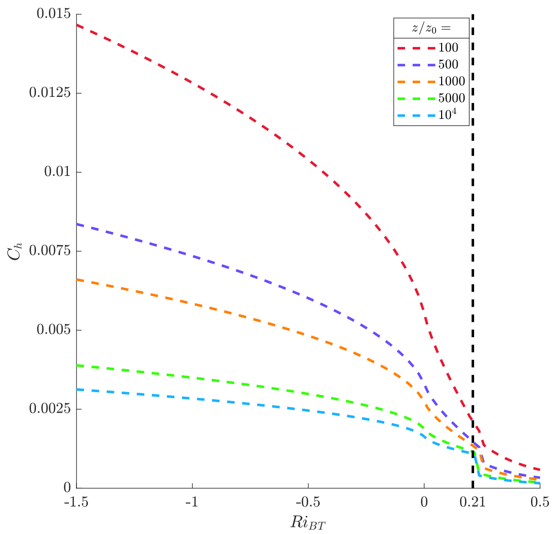

FIGURE 3.4: Bulk transfer coefficient for heat and moisture C_h in terms of the bulk Richardson number Ri_{BT} and $z_0/z_T = 7.4$. The critical Richardson number (Ri_{c}) is 0.21.

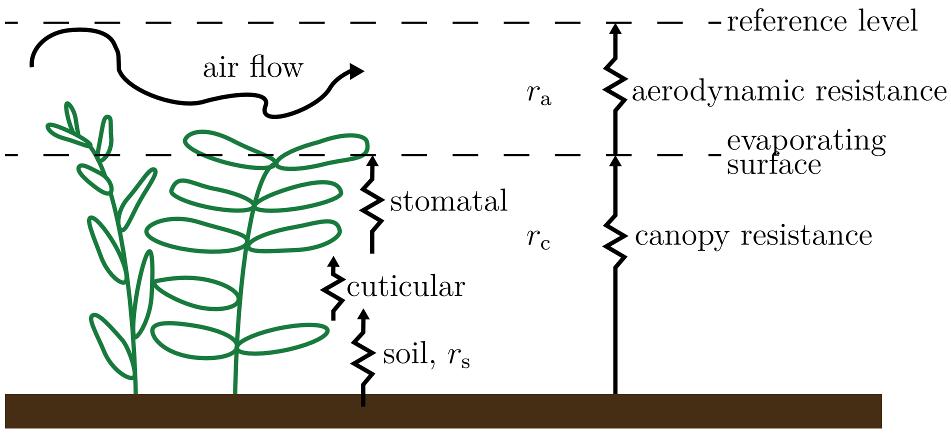

Figure 3.5: Diagram of the resistances encountered in a simplified soil-plant-atmosphere system. The water transport from the surface of the leaves or bare soil to the atmosphere is determined by the aerodynamic resistance r_a. If the evaporation is from bare soil, the soil resistance r_s has to be considered. Alternatively, the transport through plants encounters a canopy resistance r_c that describes the processes in cuticles and stomata.

the surface and therefore one cannot assume that the air close to the surface is saturated with water vapour. Furthermore, open water surfaces are as of yet uncommon on buildings and most of the flux will thus stem from vegetation or soil of green roofs/walls. Plants lose water through opening their stomata, but also through their outermost layer, the cuticle. A large number of processes is involved in transport of water in soil and plants. Indeed, the nature of the ground influences the roots and their water uptake; plants have a varying metabolism depending on age, size, season etc.. Modelling these processes is seldomly done in detail in atmospheric models. We thus utilise a modified Jarvis-Stewart (JS) approach (Jarvis, 1976, Stewart, 1988). This approach adds additional resistance to the transport of moisture from vegetation and soil to the atmosphere. The added resistance is based on empirical functions depending on plant and environmental parameters. The resistances for the plant canopy (r_c [s m^{-1}]) and for the soil (r_s [s m^{-1}]) can be expressed as:

$$r_c = \min\left(r_{max}, \frac{r_{c,min}}{LAI} f_1(K) f_2(W_G) f_3(T_s)\right) \tag{3.59}$$

$$r_s = \min\left(r_{max}, r_{s,min} f_2(W_G)\right) \tag{3.60}$$

where LAI [m^2 m^{-2}] is the leaf area index, the term f_1 is a function of net shortwave radiation K [W m^{-2}], f_2 depends on soil moisture content W_G [kg m^{-2}] and f_3 on the wall temperature T_s [K]. We follow Van den Hurk et al. (2000) for f_1 and f_2 and

Moene & van Dam (2014) for f_3 (see also (2.10)-(2.12)) and they are given by:

$$f_1^{-1} = \min\left(1, \frac{c_1 K + 0.05}{0.81(c_1 K + 1)}\right) \tag{3.61}$$

$$f_2^{-1} = \min\left(1, \max\left(0.001, \frac{W_\mathrm{G}/d - W_\mathrm{wilt}}{W_\mathrm{fc} - W_\mathrm{wilt}}\right)\right) \tag{3.62}$$

$$f_3^{-1} = \max\left(0.001, (1 - c_2(c_3 - T_\mathrm{s})^2)\right) \tag{3.63}$$

$$h_\mathrm{rel} = \max\left(0, \min\left(1, \frac{1}{2}\left[1 - \cos\left(\pi \frac{W_\mathrm{G}}{W_\mathrm{fc}}\right)\right]\right)\right) \tag{3.64}$$

where $c_1 = 0.004\mathrm{m}^2\,\mathrm{W}^{-1}$, $c_2 = 0.0016\mathrm{K}^{-2}$, $c_3 = 298\mathrm{K}$, d [m] is the thickness of the soil layer, W_wilt [$\mathrm{kg\,m^{-3}}$] is the soil moisture at the wilting point, W_fc [$\mathrm{kg\,m^{-3}}$] is the soil moisture at field capacity and h_rel [-] is the relative humidity above soil following Noilhan & Planton (1989). The moisture flux from roof and wall facets is then expressed as

$$q_* u_* = \frac{q_\mathrm{a} - q_\mathrm{sat}(T_\mathrm{s})}{\frac{1}{uC_\mathrm{h}} + r_\mathrm{c}} + \frac{q_\mathrm{a} - q_\mathrm{sat}(T_\mathrm{s}) h_\mathrm{rel}}{\frac{1}{uC_\mathrm{h}} + r_\mathrm{s}} \tag{3.65}$$

with the units [$\mathrm{kg\,kg^{-1}m\,s^{-1}}$]. The aerodynamic resistance $r_\mathrm{a} = (uC_\mathrm{h})^{-1}$ is obtained from the standard wall function (Eq. (3.48)) where the vegetation is considered with appropriate roughness lengths. To determine the saturation specific humidity q_sat [$\mathrm{kg\,kg^{-1}}$] we use empiric formulas from Bolton (1980) and Murphy & Koop (2005) that are accurate within normal temperature ranges encountered in cities:

$$p_\mathrm{sat} = 6.112 \exp\left(\frac{17.67(T - 273.15)}{T - 29.65}\right) \quad [\mathrm{hPa}] \tag{3.66}$$

$$q_\mathrm{sat} = 0.62198 \frac{p_\mathrm{sat}}{p - p_\mathrm{sat}} \quad [\mathrm{kgkg^{-1}}] \tag{3.67}$$

3.5.3 Integration into LES code

A schematic of the implementation and the order of several model routines are shown in Figure 3.6. Every time-step (except the initial one) starts with applying the conditions at the lateral boundaries, e.g. periodicity. Then the effects of moist thermodynamics, such as temperature changes due to evaporating and condensing water, are considered. In the advection step quantities are transported according to the resolved velocity field. The transport due to the non-resolved sub-grid processes is modelled directly after. Followed by additional forcings such as the Coriolis effect. Finally, the top and bottom boundary conditions are applied and the immersed

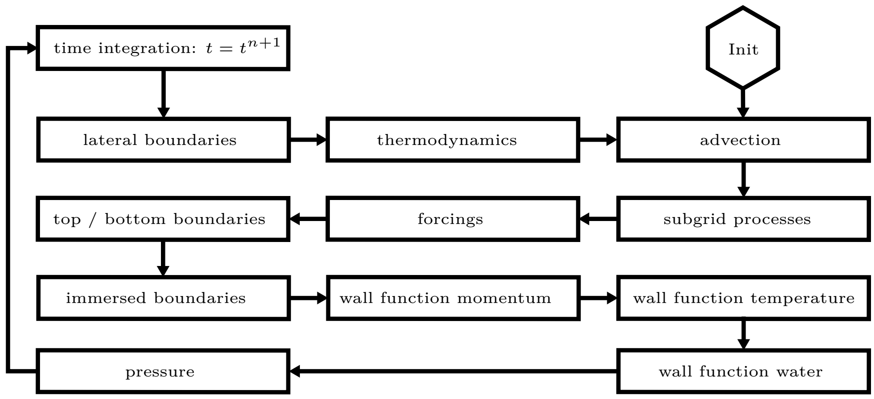

Figure 3.6: Schematic of the main routines in DALES.

boundary method ensures that there is no wind and transport into buildings. At this point the momentum, temperature and moisture fluxes from the wall functions are calculated for all surfaces based on their surfaces properties. The fluxes are then added to the prognostic equations (3.2) & (3.3) before time integration is done and a new time-step starts.

3.6 Verification

This section demonstrates the correct implementation of the wall function approaches (3.5.1 & 3.5.2). Comparison with experimental data is difficult. Wind-tunnel experiments are scarce since it is challenging to obtain realistic Richardson numbers in an experimental setup. The temperature difference between the air and the building-model surface can exceed 100K which makes controlling the wall temperatures arduous (Richards et al., 2006). Furthermore, the wall function depends on the Von Kármán constant (κ), whose cited value usually lies between 0.35-0.41. Often it is not explicitly stated which value of κ was used in a study. We have already shown in Figure 3.3 that the wall function replicates the original C_d from Uno et al. (1995). To ensure the correct behaviour of the wall function in an operational situation, we examine the momentum flux over flat terrain under neutral conditions. In the absence of any explicitly resolved form-drag the mean surface momentum flux has to balance the applied pressure force driving the LES simulation:

$$\left\langle u_*^2 \right\rangle = \frac{\partial p}{\partial x}\frac{L_z}{\rho} \tag{3.68}$$

3.6.1 Momentum

Recalling equation 3.47 we can calculate the surface momentum flux if the drag coefficient and tangential velocity are known. For a neutral case, with $z_0 = 0.01\text{m}$ and $\Delta z = 2\text{m}$ we find $C_d = 0.00793$ (see also Figure 3.3 for $Ri_{\text{BT}} = 0$). Figure 3.7 shows a comparison of the expected momentum flux to LES results for flows driven along x and y direction by a pressure gradient. The momentum flux calculated by the wall function in the LES matches the expected value given by the product of C_d and the tangential velocity U_T squared (see Eq 3.49) in all four cases. Furthermore the mean momentum flux is indeed balancing the applied pressure force. It can thus be concluded that the wall function for momentum is implemented correctly and is working properly.

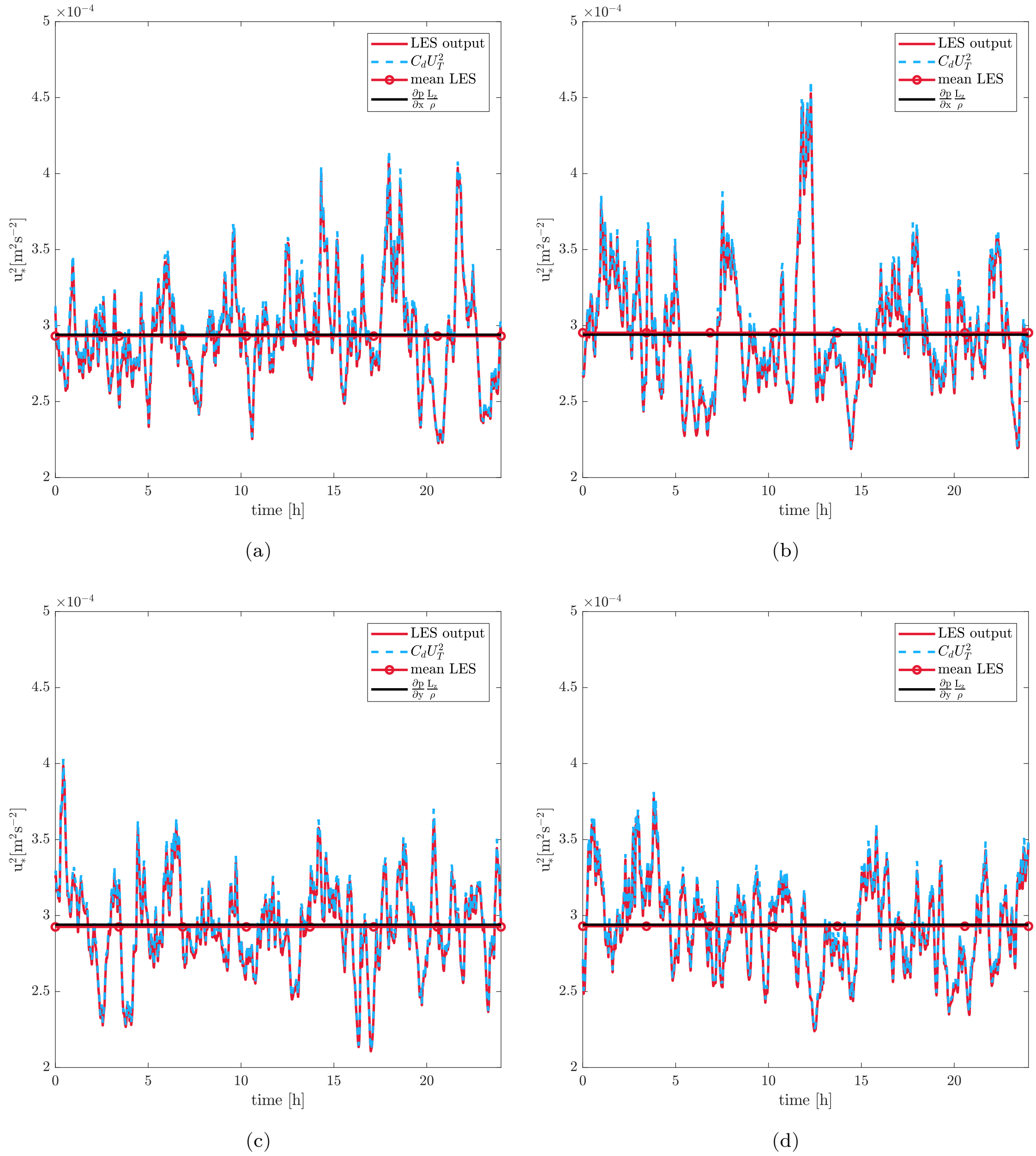

FIGURE 3.7: Surface momentum flux for a) $u > 0$ b) $u < 0$ c) $v > 0$ d) $v < 0$. Momentum flux (u_*^2) from LES output, reconstructed from velocity output ($C_d U_T^2$) and compared to the driving pressure force ($\frac{\partial p}{\partial x}\frac{L_z}{\rho}$; $\frac{\partial p}{\partial y}\frac{L_z}{\rho}$). Averaged over x and y. For (A) $\frac{\partial p}{\partial x} > 0$, (B) $\frac{\partial p}{\partial x} < 0$, (C) $\frac{\partial p}{\partial y} > 0$, (D) $\frac{\partial p}{\partial y} < 0$

3.6.2 Convective case

Verification of surface heat flux is more challenging. Results from DALES are compared directly to LES results from Cai (2012b), since in his study Cai compares the approach to wind-tunnel experiments of Kovar-Panskus et al. (2002) encountering a series of difficulties.

The simulation set-up is a flow over a canyon-like cavity (see Fig 3.8). The canyon is h = 18m high and l = 18m wide. The domain size is 24m × 40m × 90m with 80 × 40 × 91 grid cells. This results in a resolution of 0.3m × 1m × 0.3m inside the canyon; and a gradually vertically stretched grid above. The simulation is periodic in x and y and driven by a constant free-stream velocity $U_F = 2.5\text{m s}^{-1}$. Two cases are examined: 1) the downstream wall and roof are heated (T_0+9K, assisting case) 2) the upstream wall and roof are heated (T_0+9K, opposing case). In Case 1 the buoyancy flux from the heated downstream wall will assist the recirculation forming inside the canyon, while in Case 2 the additional buoyancy will oppose the general flow in the cavity. Figure 3.9 shows good agreement in the time averaged developed flow between results from DALES and Cai (2012b), for both the assisting and opposing case. Especially the location of the centre of the main circulation in the opposing case is remarkably similar.

In Figure 3.10 the mean temperature fields for both cases are compared and show excellent agreement. In the assisting case the heat is concentrated on the downstream canyon edge from where it is efficiently mixed with air aloft. The mean temperature inside the canyon is thus only slightly elevated. In the opposing case the downdraft along the heated wall leads to a more complicated flow patterns inside the canyon, effectively reducing the exchange between the canyon and the atmosphere. As a results, more heat is trapped inside the canyon, leading to increased temperatures. The quantitative agreement with Cai (2012b) confirms the correct implementation of the wall function for temperature for both horizontal and vertical walls.

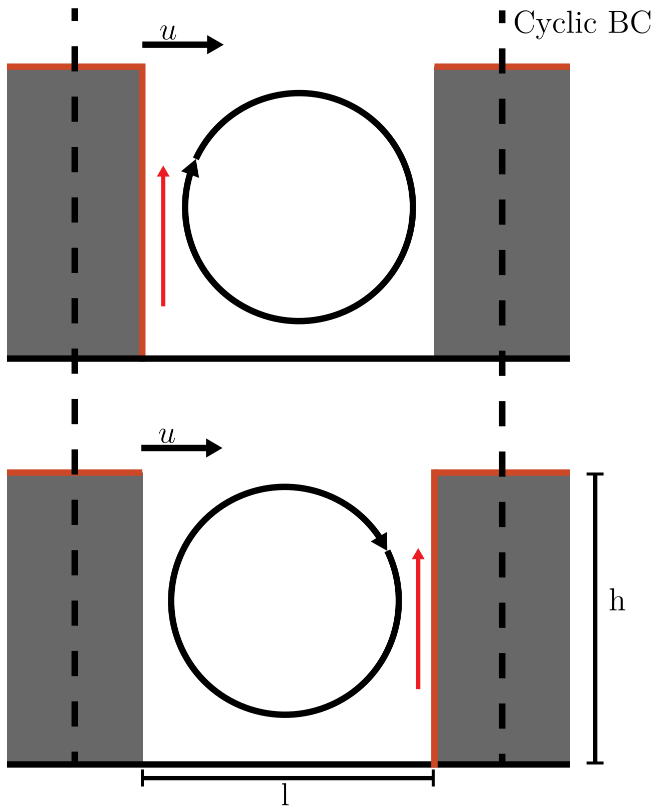

Figure 3.8: Schematic of the case setup in section 3.6.2 following Cai (2012b). The canyon has a height h and a width l. Red surfaces are heated. Top: Assisting case; Bottom: Opposing case.

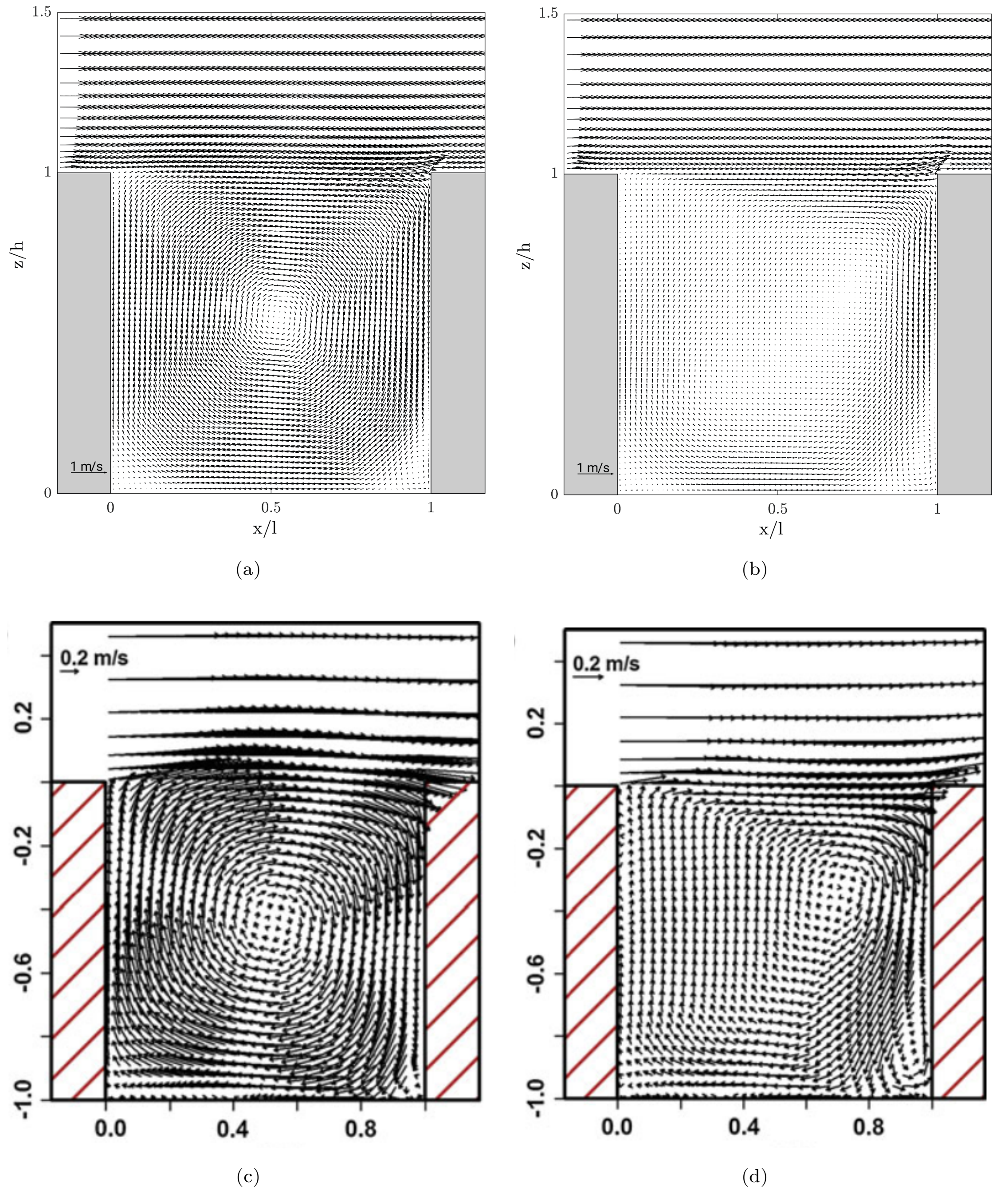

FIGURE 3.9: Mean velocity vectors (a&b) compared to Cai (2012b, c&d). Left column shows the assisting case, right column the opposing case.

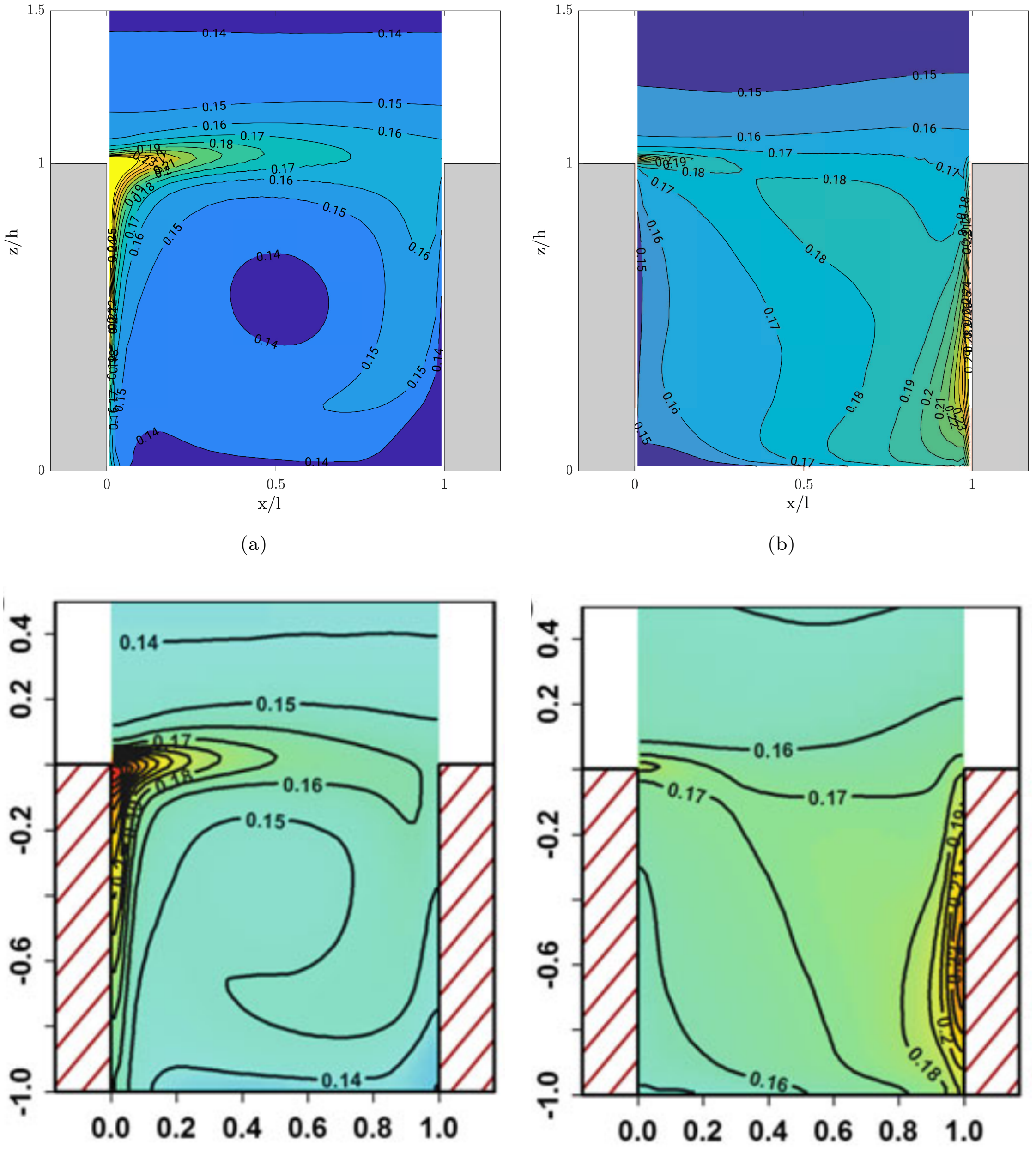

(a)

(b)

(c)

(d)

Figure 3.10: Mean temperature fields (a&b) compared to Cai (2012b, c&d), T_0 was subtracted. Left column shows the assisting case, right column the opposing case.

4

Surface energy balance & radiation

4.1 Introduction

In chapter 3.5 the wall functions describing the turbulent fluxes between atmosphere and surface were introduced and verified. The surface properties influencing these fluxes ($W_{\mathrm{G}}, T_{\mathrm{s}}$) can vary in time and are spatially heterogeneous. Most notably the surface temperatures are determined by the surface energy balance:

$$\frac{dQ}{dt} = (L^{\downarrow} - L^{\uparrow}) + (K^{\downarrow} - K^{\uparrow}) - (H + E + G). \tag{4.1}$$

Often Eq. (4.1) is considered for a large area, averaging out many local features: in urban energy balance models the horizontal scales are usually $10^2 - 10^4$m (Grimmond et al., 2010). Yet, from the perspective of a single surface all the terms are rather intricate. The turbulent sensible and latent heat flux from a single surface changes with every wind gust while the internal wall temperatures are much less sensitive and vary on much larger timescales, since a large amount of heat is stored in the material. Furthermore, the radiation terms depend strongly on the orientation of the surface, shading and the field of view. For example, if a large portion of the field of view of a surfaces comprises of other surfaces it likely receives only little direct sunlight, since it is often shaded. On the other hand it is likely to receive a large amount of longwave radiation from its surroundings as building walls are generally warmer than the sky. Due to the large spatial and temporal variability in surface

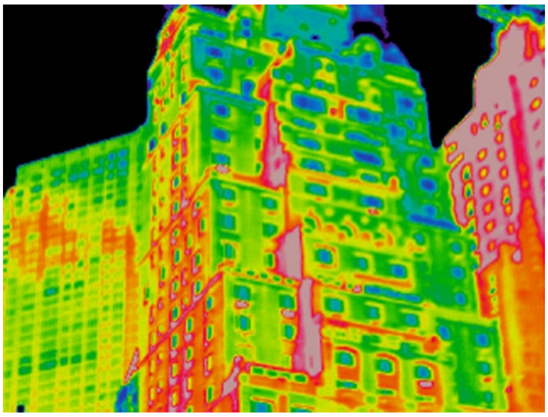

(a)

(b)

Figure 4.1: Image of Hampshire House, New York. a) Thermal image. Sunlight is incident from the left, leading to warmer facets (red). Walls at larger angles to the sun or in the shade appear cooler (blue). Windows are relatively cool since they absorb little sunlight and are in contact with colder indoor air. b) Normal photograph. From Nickolay Lamm (2018).

temperatures, especially in heterogeneous terrain, it is important to consider the surface energy balance carefully to achieve more realistic urban representation in LES models. To account for these effects, every surface in DALES is divided into several smaller facets. The process how these facets are created for the entire domain is described in section 4.2. The energy budget, including radiation, has to be evaluated for each facet. As outlined in section 1.2, equation (4.1) shows that the surface energy balance is influenced by sensible and latent heat flux, the ground heat flux, the incoming shortwave radiation ($K^{\downarrow}$), the reflected shortwave radiation ($K^{\uparrow}$), the incoming longwave radiation ($L^{\downarrow}$) and the outgoing longwave radiation ($L^{\uparrow}$).
This chapters will outline how all these terms are modelled in DALES. Before the shortwave budgets can be calculated it is necessary to consider shading and reflections, for this purpose view factors will be introduced in section 4.3.1. Shortwave radiation will be treated in chapters 4.3.2 and longwave radiation in section 4.3.3. Finally, section 4.4 documents the modelling of heat storage and ground heat flux.

4.2 Urban facets

As is evident in Figure 4.1 the surface temperatures of buildings and roads can be very heterogeneous. This can be caused by variable wind and radiation patterns or differing building materials. To get a good representation of the urban landscape it is thus advantageous to divide big surfaces into smaller patches. In general, decreasing the area of patches should lead to more accurate results but increases computational demand. However, if for example the urban fabric is not well known, increasing the resolution can actually be detrimental to the models performance. DALES accepts grid-conforming immersed boundaries, i.e. cuboids, and for the calculation of the surface energy balance it is necessary that each side of those blocks is either entirely internal (i.e. towards the inside of a building), or external (i.e. towards the outdoor environment). Accepting these constraints simultaneously leads to a finer representation of the surface. Every topographic element, like a building, is sliced into smaller blocks. An example is shown in Figure 4.2. To reduce the number of elements, all blocks that are entirely inside a building can be merged with neighbouring blocks as long as they continue to form a cuboid.

Suspended and overhanging structures are currently not supported. Thereby every block has only five sides that need be considered. The sides of a block are flat surfaces and will be called facets for the remainder of the thesis. All facets are numbered according to their orientation for easier referencing (1=top, 2=west, 3=east, 4=north, 5=south) as shown in Figure 4.3. Facets represent all types of surfaces present in the urban landscape, such as roofs, walls, roads and green roofs. Every facet is thus also assigned properties accordingly, needed for the wall function and energy balance calculation. These are the momentum roughness length z_0 [m], the heat roughness length $z_{0\mathrm{h}}$ [m], the shortwave albedo α [-] and the longwave emissivity ϵ [-]. Furthermore, every facet consists of multiple layers each with properties: thickness d [m], density ρ [kg m^{-3}], specific heat capacity c_p [J kg^{-1} K^{-1}] and thermal conductivity λ [W m^{-1} K^{-1}]. The last three terms can be combined to form the thermal diffusivity $\varkappa = \lambda/(\rho c_\mathrm{p})$ [m^2 s^{-1}].

Furthermore, additional facets have to be introduced due to the fact that the ground surface is not given as a topographic element. Voids between building-blocks (i.e. roads, parks, etc.) need to be populated with facets. The floor facets immediately adjoining a building are given the same length as the corresponding wall facets and a width of one grid cell. This is necessary to correctly calculate radiative exchange between two facets with a common edge, as described in section 4.3.1. The rest of the floor is then filled with rectangles, restrained by a maximum side length. Alternatively, if the nature and configuration of the floor is known in more detail the

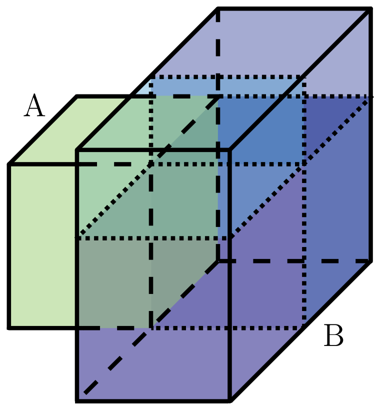

Figure 4.2: A building consisting of two blocks A and B. Block A (■) remains intact, block B will be divided into four smaller blocks (■,■,■,■), so all faces are either entirely on the in- or outside of the building.

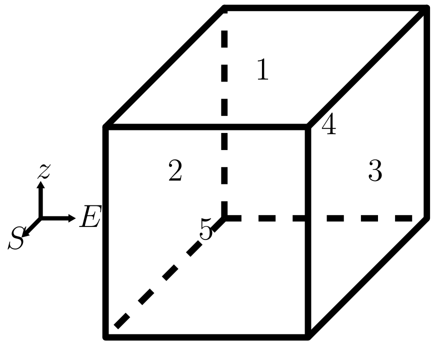

Figure 4.3: Numbering of block facets for easier referencing (1=top, 2=west, 3=east, 4=north, 5=south).

facets can be created accordingly and be specified using the facet properties.

Domain boundaries Following Krayenhoff & Voogt (2007) we add a wall along the domain edge of a height equal to the mean building height in the domain. This wall is used to approximate the effect of the surrounding built environment on radiation, that cannot be captured within the model domain. These bounding wall facets are solely used for radiative calculations and do not appear in the LES simulation and have thus no direct effect on air flow. A sample geometry including buildings, floors and bounding wall can be seen in Figure 4.9. Once the geometry and all facets are defined the radiative exchanges can be calculated. The process of generating blocks has been automated entirely and will be discuss in detail in chapter 5.

4.3 Radiation

4.3.1 View factors

To calculate the radiative exchanges between two facets their geometric relation to one another has to be determined and the radiative processes need to be described. To achieve this there are commonly two alternative approaches pursued in the complex urban structure: 1) Ray tracing and Monte Carlo simulation; and 2) radiosity approach with configuration factors. For very complex or curved surfaces radiative exchange is commonly determined by tracing randomized rays of a Monte Carlo simulation with considerable computational effort. This approach becomes more and more feasible with increasing computational power and specialised GPU computing platforms like CUDA. A big advantage of this approach is its potential to also handle specular reflections. Ray tracing models have for example been used to study urban photovoltaic energy potential (Erdélyi et al., 2014) and urban climate and meteorology (Krayenhoff et al., 2014, Girard et al., 2017).
However, for planar surfaces, as are present in this study, the radiosity approach is generally still faster (Walker et al., 2010). In this approach it is assumed that the radiosity across a facet is uniform. This allows the separation of the geometric relation between two facets from the radiative process itself (Howell et al., 2010). View factors (configuration factors) describe this geometric relation. View factors

are often encountered in the context of urban climate in the form of sky view factors (see section 4.3.1) and canyon view factors. However, the usage here is more general and describes the radiative exchange of any two surfaces. The radiosity approach has also been used to study urban climate (e.g. Aoyagi & Takahashi, 2012, Resler et al., 2017). The approach currently employed follows Rao & Sastri (1996), who found Gaussian quadrature to be capable to accurately calculate view factors. It has to be noted at this point that several conventional assumptions were made regarding the radiation and radiative properties of all the facets (e.g. Krayenhoff et al., 2014, Howell et al., 2010), namely

- no wavelength dependency, except the separation into short- and longwave,
- facets are "grey" in the longwave regime, i.e. absorptivity = emissivity,
- facets are isothermal,
- reflections are diffuse,
- emitted radiation is diffuse,
- the radiosity (leaving radiant flux) is uniform across the facet.

For calculating both longwave and shortwave radiation, view factors are used. The view factor $\psi_{i,j}$ is defined as the ratio of radiation leaving the surface of facet i hitting surface of facet j, divided by the total amount of radiation leaving facet i. View factors thus take values between 0 and 1 and $\sum_{j \in q} \psi_{i,j} = 1$, where q is the set of all facets that can be seen by i (including the sky). All view factors $\psi_{i,j}$ between any two facets i and j have to be calculated. This makes the number of calculations needed $\mathcal{O}(n^2)$. Several numerical methods exist to calculate view factors between surfaces, since in most cases the analytical solutions to the problem are not known. Generally the view factor between two finite areas i and j is given by

$$\psi_{i,j} = \frac{1}{A_i} \int_{\mathrm{A_i}} \int_{\mathrm{A_j}} \frac{\cos\Theta_i \cos\Theta_j}{\pi \mathcal{S}^2} dA_j dA_i, \tag{4.2}$$

where $\mathcal{S}$ is the length of the vector connecting the infinitesimal elements dA_i and dA_j and Θ is the angle between this connecting vector and the normal vector on dA_i or dA_j respectively (see Figure 4.5).

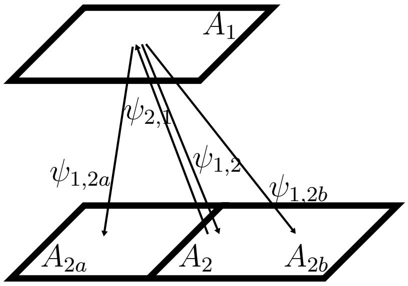

Figure 4.4: The view factor ψ for two surfaces 1 and 2 of area A_1 and A_2, respectively, are reciprocally related (Eq. (4.3)). The view factors between surface 1 and surfaces 2a and 2b added together result in the view factor between surface 1 and surface 2 (Eq. (4.4)).

The analytical evaluation of Eq. (4.2) is only possible in special cases and various methods to obtain the view factors have been discussed in the literature (Sparrow, 1961, Hottel & Sarofim, 1967, Howell et al., 2010). There are two general rules in view factor algebra: the reciprocal relationship of view factors; and the additive relationship of view factors (Threlkeld, 1970). The two relationships are illustrated in Figure 4.4. The first rule states that for two surfaces 1 and 2 of area A_1 and A_2, respectively, the view factors are reciprocally related

$$\psi_{1,2} = \frac{A_2}{A_1}\psi_{2,1}. \tag{4.3}$$

The second rule states that when we subdivide surface 2 into smaller surfaces 2a and 2b of area $A_{2\mathrm{a}}$ and $A_{2\mathrm{b}}$, respectively, the total amount of radiative energy emitted from 1 and impinging on 2 (=2a+2b) remains unchanged:

$$\psi_{1,2} = \psi_{1,2a+2b} = \psi_{1,2a} + \psi_{1,2b}. \tag{4.4}$$

The fact that view factors only depend on the geometry of the problem and do thus generally not change during the simulation, allows one to calculate all $\psi_{i,j}$ *a priori* and store the resulting matrix as input to the LES model.

Numerical integration is required to obtain the view factors. Considerable computational savings can be achieved by replacing the integration over two areas in equation (4.2) by integration over two surface boundaries (Rao & Sastri, 1996). This can be done using Stokes' theorem (see Appendix A.1). The view factor can then be expressed as

$$\psi_{i,j} = \frac{1}{2\pi A_i} \oint_{\mathrm{C}_i} \oint_{\mathrm{C}_j} [\ln(\mathcal{S}) dx_j dx_i + \ln(\mathcal{S}) dy_j dy_i + \ln(\mathcal{S}) dz_j dz_i] \tag{4.5}$$

where $\mathcal{S}$ is the distance between two infinitesimal line segments along the contours. The numerical integration of $\ln(\mathcal{S})$ is done using 6^{th} order Gauss-Legendre quadrature (Appendix A.2), which is effective and accurate for straight-edged contours (Rao & Sastri, 1996). The logarithm of $\mathcal{S}$ can vary substantially if the two line segments are close and $\mathcal{S}$ is small, in which case the precision is increased by using higher order quadrature. The evaluation of equation (4.5) is impossible in the case that the two contours share a common edge, because $\ln(\mathcal{S}) = \ln(0) = -\infty$. Ambirajan & Venkateshan (1993) provide an exact analytical solution for the contribution from the element on the common edge of the two surfaces to the overall view factor:

$$\Delta\psi_{i,j} = \frac{L_{\mathrm{c}}^2}{2\pi} \left(\frac{3}{2} - \ln\left(L_{\mathrm{c}}\right) \right) \tag{4.6}$$

where L_{c} is the length of the common edge. Since all facets are straight-edged, the only error in this approach lies in the approximation of $\ln(\mathcal{S})$ within the elemental intervals of the integration. High order quadratures thus ensure accurate numerical results.

Blocked view & shadowing View factors can be calculated using equations (4.5) and (4.6) as long as both facets can see each other entirely. Three important exceptions can be identified:

1. The facets cannot see each other at all, given their position and orientation.
2. A facet intersects the plane defined by the other facet (see Figure 4.6(a)).
3. The view is (partly) blocked by another surface (see Figure 4.6(b)).

The first case occurs frequently. E.g. any west facing facet cannot possibly see any other west facing facet or any facet that is entirely to the east. This relationship is reciprocal. For every facet pair it is thus first determined if they are in each other's field of view, and if not, $\psi_{i,j}$ and $\psi_{j,i}$ are immediately set to 0.

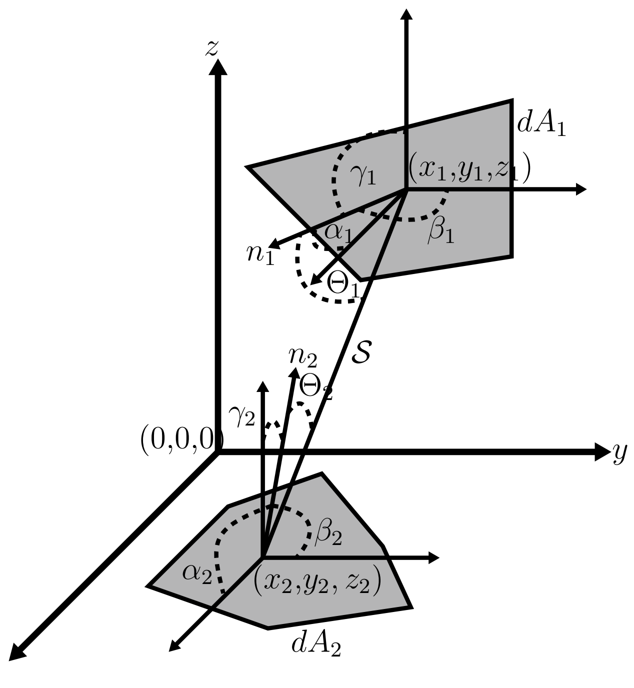

Figure 4.5: Differential areas dA_1 and dA_2. The angles between the normal vector n and the unit vectors are α, β and γ, respectively. $\mathcal{S}$ is the vector connecting dA_1 and dA_2.

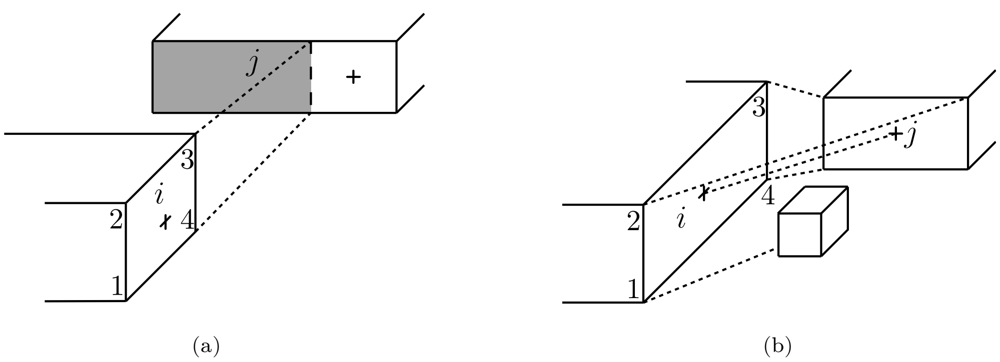

Figure 4.6: (a) The plane of facet i intersects facet j. The view factors can be correctly calculated between i and the unshaded part of j. (b) The view between corner 1 of facet i and the corresponding corner of facet j is blocked, resulting in $p_{\mathrm{b}} = 0.875$.

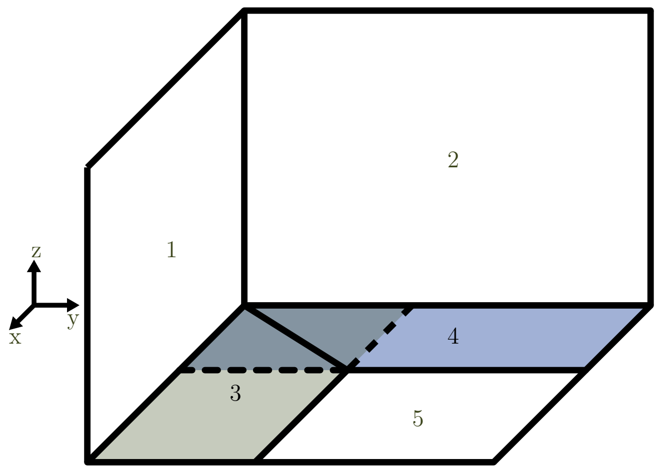

Figure 4.7: Overlapping floor facets (dashed lines, dark grey area) get split diagonally resulting in two trapezoidal facets 3 & 4.

The second problem can be circumvented by cropping the intersecting facet along the intersection line. The view factors can then be calculated using the now smaller facet and the result remains accurate.

There is no straightforward solution to the third problem, assessing if the view between two facets is blocked. Depending on how the facets are arranged and the geometry of the object blocking their view, determining a precise view factor can be difficult. To avoid computationally expensive solutions such as Monte Carlo simulations we determine a percentage p_b the facets can see of each other and multiply ψ with that percentage. To obtain p_b we define five points, the four corners and the centre, on every facet and determine if they can see the corresponding point on the other facet (see Figure 4.6(b)). The weight of the centre is 50% and the weight of each corner 12.5%.

Three sided corners In section 4.2 it was described that floor facets need to be added around buildings of the same length as the adjoining wall facet. This leads to overlapping floor facets in three sided corners (where the two walls and the floor meet). To calculate the view factors the overlapping facets are thus cut diagonally (see Figure 4.7). The view factors between the now trapezoidal floor facets and any other facet can then be calculated with the standard method.

Sky view factor The sky view factor ($\psi_{\mathrm{sky},i}$) denotes the fraction of radiation leaving i that enters the sky vault and does not impinge on any other facet. It is the residual view factor after summing over all facets: $\psi_{\text{sky},i} = 1 - \sum_{\text{j}=1}^{p} \psi_{i,j}$, where p is the total number of facets. The sky view factor is also used to determine how much diffusive radiation from the sky any facet receives. Sky view factors have been used intensively to study the UHI (e.g. Oke, 1981, 1988, Arnfield, 2003, Svensson, 2004, Zhu et al., 2013).

4.3.2 Shortwave radiation budget

The net shortwave radiation K on a facet i is defined as

$$K_i = K_i^{\downarrow} - K_i^{\uparrow} \qquad [\text{Wm}^{-2}], \tag{4.7}$$

assuming no transmission of radiation through the surface. In this case the shortwave absorptivity ($\varsigma_{\text{S},i}$) and the albedo (α_i) of the surface are directly related

$$\alpha_i = 1 - \varsigma_{\text{S},i} \qquad [-], \tag{4.8}$$

and the reflected shortwave radiation ($K^{\uparrow}$) can be expressed as

$$K_i^{\uparrow} = \alpha_i K_i^{\downarrow} = (1 - \varsigma_{\text{S},i}) K_i^{\downarrow} \qquad [\text{Wm}^{-2}]. \tag{4.9}$$

The incoming shortwave radiation ($K_i^{\downarrow}$) can be divided into three parts (Oke et al., 2017): direct solar radiation (S_i), diffuse radiation from the sky (D_i) and diffusely reflected radiation from other facets (R_i):

$$K_i^{\downarrow} = S_i + D_i + R_i \qquad [\text{Wm}^{-2}]. \tag{4.10}$$

It is important to consider all three components. Many of the urban facets can be completely shaded, thus $S_i = 0$, but potentially receive diffuse radiation from the sky or reflected radiation from other facets.

Direct solar radiation The direct solar radiation on a facet (Wu, 1995) is defined as

$$S_i = I \cos(\upsilon - \xi_i) \cos(\chi_i) f_{\text{e},i} \qquad [\text{Wm}^{-2}]. \tag{4.11}$$

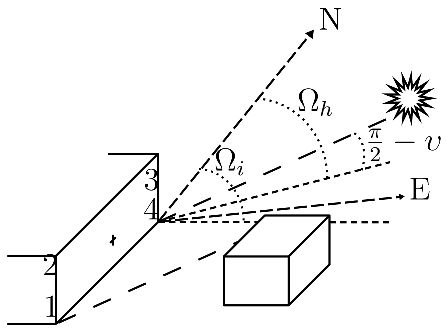

Figure 4.8: Angles describing the relation between a facet and the sun. Ω are the azimuth angles from North and υ the zenith angle (the complement to the elevation angle).

The solar irradiance (I) is a model input and can be a constant or follow a diurnal cycle; it is assumed that all effects of atmospheric turbidity and clouds are included. The effect of geometry is captured by the sunlit fraction of the facet $f_{\mathrm{e},i}$, the two cosines account for the orientation of the facet in relation to the sun. The angle υ is the solar zenith and ξ_i the slope angle of the facet (i.e. $\xi_i = 0$ for a horizontal facet and $\xi_i = \pi/2$ for a vertical facet). The angle χ_i is constructed in the following way

$$\chi_i = \begin{cases} \pi/2, & \text{if surface faces away from sun} \\ 0, & \text{elseif the surface is horizontal} \\ |\Omega_h - \Omega_i|. & \text{else} \end{cases}$$

where Ω_h is the solar azimuth and Ω_i is the azimuth of facet i (see Figure 4.8). Like the solar irradiance, the solar zenith and azimuth angles are also model inputs. Solar angles for all coordinates, dates and times can be readily obtained from online sources such as the "Solar Position Calculator" from the National Oceanic and Atmospheric Administration (NOAA, 2018).

The facet azimuth angles are also used to determine whether the facet is shaded or not. If $|\Omega_h - \Omega_i|$ is larger than $\pi/2$, the facet is not oriented towards the sun and is thus self-shaded. If the facet i is not self-shaded the sun might still be blocked by another facet j. Therefore, the path between every non-self-shaded facet and the sun is calculated and checked if it intersects with any other facet. This can potentially lead to considerable errors, since for large facets it is not evident from which point the path to the sun should be constructed. To alleviate this problem somewhat, we use the same principle as for view factors and calculate the sunlit status for the four corners and the centre of the facet, where the centre contributes 50% and each corner

12.5% to the total sunlit fraction $f_{\mathrm{e},i}$ (see section 4.3.1).

Diffuse shortwave radiation The diffuse radiation (D_i) is caused by light scattering in the sky and is given by

$$D_i = \psi_{\mathrm{sky},i} D_{\mathrm{sky}} \qquad [\mathrm{Wm}^{-2}], \tag{4.12}$$

where D_{sky}, the total diffuse sky radiation, is a model input. The sky view factor $\psi_{\mathrm{sky},i}$, is dependent on the urban geometry and has to be calculated for every facet as detailed in section 4.3.1. In equation (4.12) we ignore the directionality of D_{sky}, which is in reality anisotropic, and can thus use $\psi_{\mathrm{sky},i}$ directly to calculate the fraction of diffuse sky radiation impinging on i.

Reflected shortwave radiation Shortwave radiation reflected by the environment has to be considered as well. All reflections are currently assumed to be perfectly diffusive (Lambertian), i.e. the amount of reflected light on a given surface is distributed equally in all directions. This is necessary to utilise view factors but does, by definition, not allow specular reflections. The amount of reflected light arriving at facet i is thus given by

$$R_i = \sum_{\mathrm{j}=1}^{p} \psi_{j,i} K_j^{\uparrow} \qquad [\mathrm{Wm}^{-2}] \tag{4.13}$$

where $\psi_{j,i}$ is the view factor between facet j and i and p is the total number of facets.

Shortwave algorithm The view factors for all pairs (i, j) can be calculated beforehand, as outlined in section 4.3.1. To account for multiple reflections, the calculation of $K_i^{\uparrow}$ (Eq. (4.9)-(4.13)) has to be iterated for all facets using following scheme:

- first reflection ($n = 0$)

  1. calculate all initial $K_{i,0}^{\downarrow} = S_i + D_i$ ((4.11), (4.12))
  2. calculate all initial $K_{i,0}^{\uparrow}$ (4.9)

3. calculate all $R_{i,0}$ (4.13)
4. recalculate all $K^{\downarrow}_{i,1} = K^{\downarrow}_{i,0} + R_{i,0}$

- iterate following steps for $n = 1, 2, ...,$ until all changes are below a desired threshold ϵ_{k}:

1. only the additional reflected radiation from the previous iteration is considered for further reflections, i.e. $K^{\uparrow}_{i,n} = \alpha_i R_{i,n-1}$
2. recalculate all $R_{i,n}$ based on the updated $K^{\uparrow}_{n}$
3. update all $K^{\downarrow}_{i,n+1} = K^{\downarrow}_{i,n} + R_{i,n}$
4. test for cancellation: $\max_i \left((K^{\downarrow}_{i,n+1} - K^{\downarrow}_{i,n})/K^{\downarrow}_{i,n} \right) \leq \epsilon_{\mathrm{k}}$

Thereafter $K^{\downarrow}$ and thus, according to (4.9), also $K^{\uparrow}$ are known for all facets.
This algorithm converges quickly, usually <10 iterations for <1% error, since albedos are generally low resulting in a large fraction of the radiation being absorbed and additional parts being lost towards the sky with every cycle. The convergence of this algorithm is studied in section 4.3.4 and an example can be seen in Fig 4.11.

4.3.3 Longwave budget

The net longwave radiation L consists of three components.

$$L_i = \varsigma_{\mathrm{L},i}(\psi_{\mathrm{sky},i} L^{\downarrow}_{\mathrm{sky}} + L^{\downarrow}_{\mathrm{env},i}) - L^{\uparrow}_i \qquad [\mathrm{Wm}^{-2}], \tag{4.14}$$

where $\varsigma_{\mathrm{L},i}$ is the longwave absorptivity and $L^{\downarrow}_{\mathrm{env},i}$ is the incoming longwave radiation from other facets. The incoming longwave radiation from the sky ($L^{\downarrow}_{\mathrm{sky}}$) is given as a model input. $L^{\uparrow}_i$ is the outgoing longwave radiation depending on the surface temperature $T_{\mathrm{s},i}$ according to the Stefan-Boltzmann law

$$L^{\uparrow}_i = \sigma \epsilon_i T^4_{\mathrm{s},i} \qquad [\mathrm{Wm}^{-2}], \tag{4.15}$$

with the Stefan-Boltzmann constant $\sigma \approx 5.67 \times 10^{-8}$W m^{-2} K^{-4} and ϵ_i is the emissivity of facet i. Since $\varsigma_{\mathrm{L},i}$ is generally close to unity for normal building materials, no reflections are considered for longwave radiation. The incoming longwave radiation from the other facets is given by:

$$L^{\downarrow}_{\mathrm{env},i} = \sigma \sum_{\mathrm{j=1}}^{p} \psi_{j,i} \epsilon_j T^4_{\mathrm{s},j} \qquad [\mathrm{Wm}^{-2}] \tag{4.16}$$

where p again is the total number of facets, $\psi_{j,i}$ is the view factor between facet j and i, ϵ_j is the emissivity of facet j and $T_{\mathrm{s},j}$ is the surface temperature of facet j.

4.3.4 Verification

This section illustrates the division of blocks, bounding walls and floors into facets based on an example arrangement of urban elements. The resulting facets can be seen in Figure 4.9. The sample elements were chosen to have a large variety of geometric relations between facets for which view factors can be determined analytically. The bounding walls representing the surrounding urban landscape in terms of radiation are included as well. View factors calculated by the method outlined in section 4.3.1 (ψ_c) are compared to analytical solutions (ψ_p, see Appendix A.3). In cases where the view between two facets is impeded as outlined in section 4.3.1 no analytical solution is known and a range is provided in which the calculated view factor has to fall. Table 4.1 provides a sample of the results.

Table 4.1: Comparison of view factors calculated by the method outlined in section 4.3.1 compared to analytical calculations. For partly blocked view the known analytical range in which the calculated view factors should lie is given. See Fig 4.9 for facet numbers.

Comparison of view factors					
Facet pair	Analytic: ψ_p	Calc.: ψ_c	Abs. error: ψ_c-ψ_p	Rel. error.: $\psi_c/\psi_p - 1$	Description
13-17	0.0686	0.0686	0.0000	0%	Identical, parallel, directly opposed
8-44	0.0222	0.0222	0.0000	0%	Parallel
13-44	0.0083	0.0083	0.0000	0%	Parallel
5-72	0.2570	0.2570	0.0000	0%	Perpendicular, common edge
32-110	0.0452	0.0452	0.0000	0%	Perpendicular
37-111	0.0852	0.0851	-0.0001	-0.11%	Perpendicular
8-134	0.0046	0.0046	0.0000	0%	Perpendicular
46-99	0.1200	0.1190	-0.0010	-0.83%	Three sided corner
54-103	0.1200	0.1190	-0.0010	-0.83%	Three sided corner
10-120	0.0023	0.0023	0.0000	0%	Self shaded
56-61	0.0539	0.0539	0.0000	0%	Self shaded
4-10	0.016-0.065	0.0328	0.0169 to -0.0328	105.5% to -50%	Partly blocked
4-131	0.0019 - 0.0033	0.0029	0.0009 to -0.0004	49.0% to -12.5%	Partly blocked
35-61	0.0532 - 0.0604	0.0453	-0.0079 to -0.0151	-15% to -25%	Partly blocked
35-68	0.0043 - 0.0109	0.0082	0.0039 to -0.0027	90.5% to -25%	Partly blocked

It is evident that unobstructed view factors are accurate within 1% relative error. View factors between self shaded facets are equally accurate. For partly blocked view the calculated ψ_c are defined as a percentage of the unobstructed view factor. In most cases ψ_c lies within the provided range. Yet, in cases where the two facets are close, but the two facet centres cannot see each other, ψ_c can underestimate the actual value of ψ. The shaded fraction of each facet is shown in Figure 4.10 for a solar azimuth angle (Ω_h) of 112.5° from north (→ east-southeast) and a solar zenith angle (υ) of 45°. Calculating the actual outline of the shadow is possible, albeit computationally more expensive, and also shown in Figure 4.10. Comparing the calculated shaded fraction as explained in section 4.3.2 to the shadow pattern shows good agreement for most facets. Only some south facing facets (i.e. facets 19 & 46)

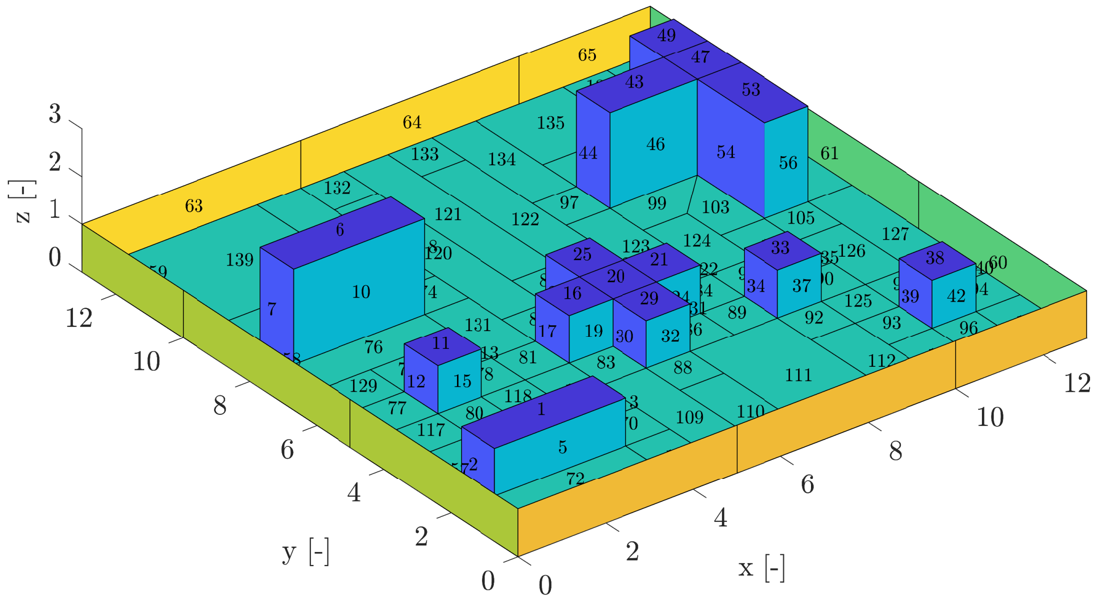

Figure 4.9: Blocks after assigning facets. The indices of the facets are displayed and the facets are coloured based on their type and orientation: Wall north, Wall west, Wall south, Wall east, Floor, Block south, Block west, Block top. Facets 99 and 103 are trapezoidal since they form a three sided corner with facets 46 and 54.

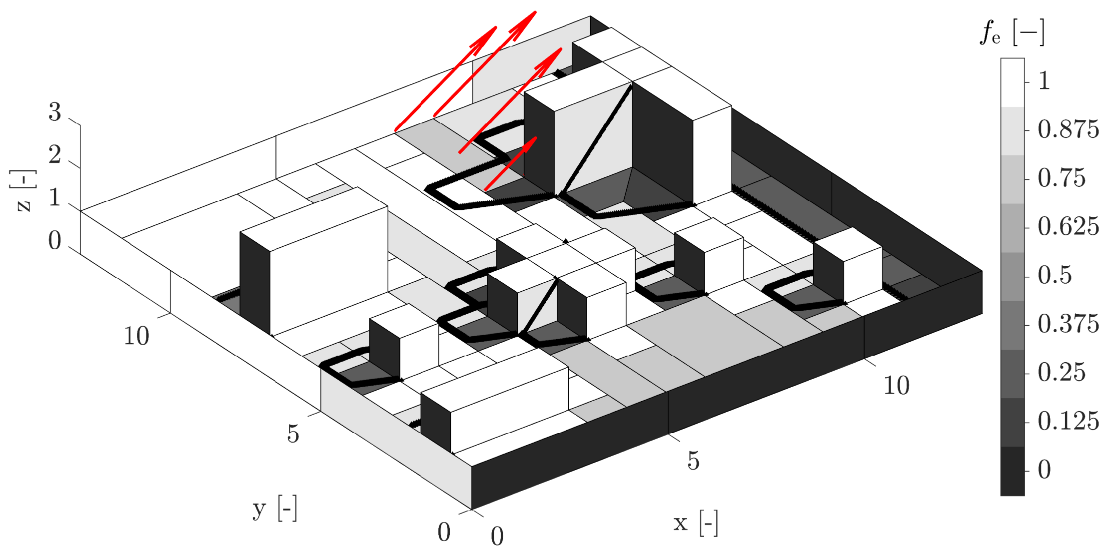

Figure 4.10: Facets colour based on their sunlit fraction ($f_{\mathrm{e},i}$). The vectors from all five points on facet 134 to the sun are shown, two of which intersect with a building resulting in a sunlit fraction of 75%. The outline of the actual shadows in thick black lines.

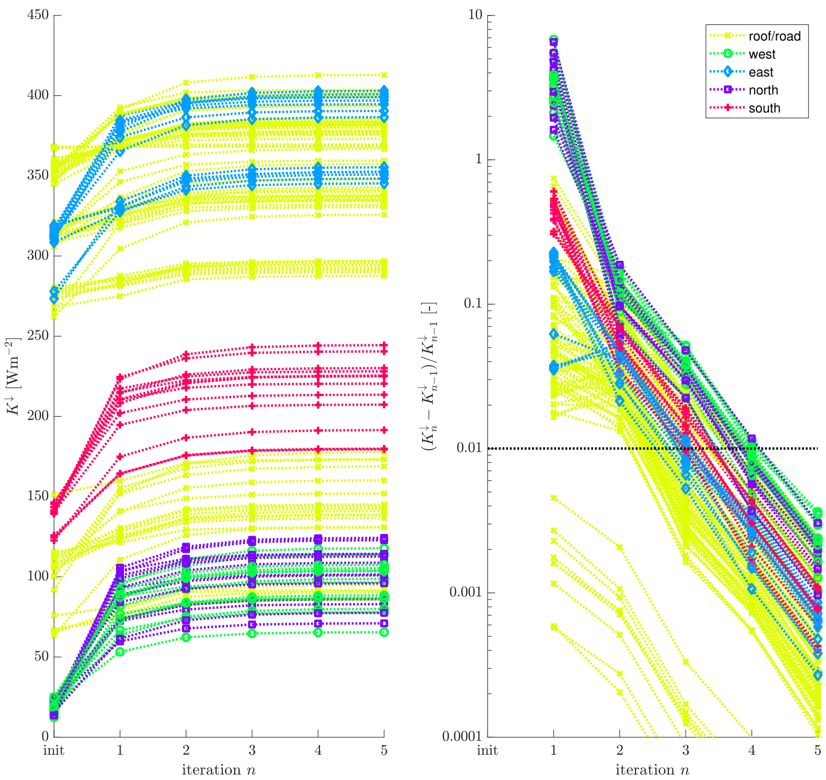

Figure 4.11: Left: Evolution of incoming shortwave radiation (K$^{\downarrow}$) during the iterative process as described in 4.3.2. Right: Relative change of total incoming shortwave radiation between iterations. The threshold $\epsilon_k = 1\%$ was chosen. The lines are coloured according to the orientation of the facet as can be seen in Fig 4.9: ↦, ↦, ↦, ↦, ↦.

are poorly represented in this example, since the outline of the shadow barely misses the centre point of the facet, which weighs 50% in the calculation. How well the shading of a facet is represented depends thus on the solar elevation and azimuth and can generally be improved if the sun's visibility is checked for more points on the facets surface.

The iteration of the shortwave radiation is shown in Figure 4.11. The iteration process is described in section 4.3.2. Every facet receives initially direct shortwave radiation from the sun depending on its orientation and shading and diffusive radiation from the sky. The reflected radiation received can be quite substantial, but the additional amount decreases quickly with further iterations. A threshold of 1% change was reached within 5 steps for all facets. In cases where the reflectance of the facets is extremely high, a slightly larger number of steps might be required. This is, however, unlikely in urban applications.Harman et al. (2004) recommend to consider one reflection event for radiation in urban canyons and above analysis shows that 5 reflections will suffice in a completely heterogeneous urban morphology. The absolute errors quickly fall below an acceptable threshold of 1W m^{-2}, or so. It is concluded that the view factors calculations are accurate enough to calculate the energy balance of urban facets. Notably the absolute errors from the view factor calculation, the shading and reflections, ultimately affecting the energy balance, are small.

4.4 Surface energy budget of ground, wall and roof facets.

To calculate the temperature evolution of every facet, we assume that every wall and roof consists of k layers of building material (see Fig. 4.12). The temperature at the interface of layer $k \in \{1, ..., K\}$ and $k+1$ is defined as T_k. Furthermore, let T_K be the indoor temperature of the facet and $T_0 = T_s$ be the outdoor surface temperature used for calculating radiation and convective heat fluxes. At every instant T_0 is given by the balance of energy fluxes at the surface:

$$-\Gamma_i(T_0) = K_i + L_i(T_0) + H_i(T_0). \tag{4.17}$$

According to section 2.2 dry conditions are assumed and no water is available for evaporation on non-vegetated surfaces and consequently the latent heat flux is omitted. The values of H are the time mean fluxes provided by the wall function, K only depends on the position of the sun and the incoming longwave radiation ($\varsigma_{\mathrm{L},i}(\psi_{\mathrm{sky},i} L^{\downarrow}_{\mathrm{sky}} + L^{\downarrow}_{\mathrm{env},i})$) can be calculated from the other facets temperatures. The two remaining unknown terms are $L^{\uparrow}_i$ and the surface conductive heat flux Γ_i.
A defining aspect of this problem is that the boundary condition at the surface, which drives the energy exchange with the wall, is strongly non-linear and, under the assumption that the surface heat flux (Γ_i) is purely conductive, i.e.

$$\Gamma_i = \lambda \frac{\partial T}{\partial z}\bigg|_s, \tag{4.18}$$

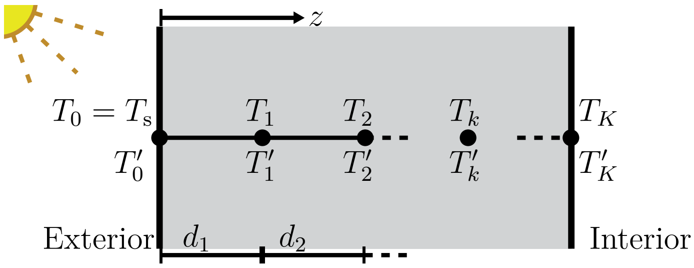

Figure 4.12: Grid layout used to model conductive heat flux. The wall or roof is divided into K layers of thickness d_K. The coordinate z points into wall the from the exterior surface. Temperatures (T) and temperature gradients (T') are defined at the layer edges.

Eq. (4.17) can be written as

$$\lambda \left.\frac{\partial T}{\partial z}\right|_s = \epsilon \sigma T_0^4 + r, \tag{4.19}$$

where $r = -(K + H + L^{\downarrow})$, λ is the thermal conductivity in W m^{-1} K^{-1} and z is pointing into the layer. This boundary condition requires information about both the temperature and its gradient at the boundary, and it would thus be very useful to have a numerical method for which these both are available at the same location without approximation. Conventional finite difference and finite volume approaches do not have this feature.

Shown in Figure 4.12 is the grid layout that will be adopted in this work to represent the temperature distribution in the facet. The variables are distributed in pairs of the temperature T_k and its gradient $T' = \left.\frac{\partial T_k}{\partial z}\right|_k$ on the cell edges, implying that there are $2(K+1)$ unknowns if the facet is discretised into K layers. This grid layout is not conventional, but is closely related to Hermitian interpolation (Peyret & Taylor, 2012) and has been used for the prediction of non-hydrostatic free-surface flow (Van Reeuwijk, 2007).

A solution will be constructed using a set of piecewise continuous quadratic polynomials, which will turn out to be splines. Consider a second order polynomial

$$T(z) = a + bz + cz^2 \tag{4.20}$$

valid over the interval $z_k < z < z_{k+1}$. Defining $T(z_k) = T_k$, $T(z_{k+1}) = T_{k+1}$, $T'(z_k) = T'_k$ and $T'(z_{k+1}) = T'_{k+1}$, it is straightforward to demonstrate that the quadratic is consistent with the following relation between the temperatures and its derivatives

$$\frac{1}{2}\left(T'_k + T'_{k+1}\right) = \frac{T_{k+1} - T_k}{d_{k+1}}, \tag{4.21}$$

where $d_{k+1} = z_{k+1} - z_k$. The coefficients a, b, c are determined by requiring that $T(z_k) = T_k$, $T(z_{k+1}) = T_{k+1}$ and $T'(z_k) = T'_k$, with result

$$T(z) = \frac{(z - z_k)(z_{k+1} - z)}{2d_{k+1}}\left(T'_k - T'_{k+1}\right) + \frac{z_{k+1} - z}{d_{k+1}}T_k + \frac{z - z_k}{d_{k+1}}T_{k+1}. \tag{4.22}$$

Here, (4.21) was used to make the representation symmetrical in the arguments. By evaluating the temperature and its gradient at z_k and z_{k+1} it becomes clear that (4.22) indeed satisfies the requirements of a spline, as a set of these functions produces a curve which is continuous in both the temperature and the gradient of the temperature. An important property of (4.22) is that, assuming the mean temperature in the layer is given by

$$\frac{1}{d_{k+1}}\int_{z_k}^{z_{k+1}} T(z)dz = \frac{1}{2}(T_k + T_{k+1}) + \frac{d_{k+1}}{12}(T'_k - T'_{k+1}). \tag{4.23}$$

The sum of the changes in mean temperatures across all layers corresponds to the heat storage term from equations (1.1) and (2.1). The temperature evolution inside the facet is described by an unsteady heat equation of the form

$$\frac{\partial T}{\partial t} = \frac{\partial}{\partial z}\left(\varkappa\frac{\partial T}{\partial z}\right), \tag{4.24}$$

where $\varkappa$ is the thermal diffusivity in m^2 s^{-1}. Integrating this equation over the interval $z_k < z < z_{k+1}$ and substituting (4.23) results in the relation

$$\frac{d}{dt}\left(\frac{d_{k+1}}{2}(T_k + T_{k+1}) + \frac{d_{k+1}^2}{12}(T'_k - T'_{k+1})\right) = \varkappa(z_{k+1})T'_{k+1} - \varkappa(z_k)T'_k. \tag{4.25}$$

The facet consists of K layers, implying that there are $2(K+1)$ unknowns. Equations (4.21) and (4.25) provide $2K$ equations, and two boundary conditions provide the final two equations to close the system.

Compact form At $z = 0$, we will apply the surface energy balance equation. The outgoing longwave radiation is expressed in the form

$$L_i^{\uparrow} = \left(\epsilon_i \sigma T_0^3\right) T_0. \tag{4.26}$$

At the building interior we impose a constant temperature[1] $T_K = T_B$, $\frac{dT_K}{dt} = 0$. In matrix form, the system of equations is then given by

$$\begin{bmatrix} 1 & 0 & \dots & \dots & 0 \\ \frac{1}{2} & \frac{1}{2} & 0 & \dots & 0 \\ 0 & \frac{1}{2} & \frac{1}{2} & \dots & 0 \\ & & \ddots & \ddots & \\ 0 & 0 & \dots & \frac{1}{2} & \frac{1}{2} \end{bmatrix} \begin{bmatrix} T_0' \\ T_1' \\ \vdots \\ \vdots \\ T_K' \end{bmatrix} = \begin{bmatrix} c_1 \\ 0 \\ \vdots \\ \vdots \\ 0 \end{bmatrix} + \begin{bmatrix} c_2 & 0 & \dots & \dots & 0 \\ \frac{-1}{d_1} & \frac{1}{d_1} & 0 & \dots & 0 \\ 0 & \frac{-1}{d_2} & \frac{1}{d_2} & \dots & 0 \\ & & \ddots & \ddots & \\ 0 & 0 & \dots & \frac{-1}{d_K} & \frac{1}{d_K} \end{bmatrix} \begin{bmatrix} T_0 \\ T_1 \\ \vdots \\ \vdots \\ T_K \end{bmatrix} \tag{4.27}$$

$$\begin{aligned} &\begin{bmatrix} \frac{d_1}{2} & \frac{d_1}{2} & 0 & \dots & 0 \\ 0 & \frac{d_2}{2} & \frac{d_2}{2} & \dots & 0 \\ & & \ddots & \ddots & \\ 0 & 0 & \dots & \frac{d_K}{2} & \frac{d_K}{2} \\ 0 & 0 & \dots & \dots & 1 \end{bmatrix} \frac{d}{dt} \begin{bmatrix} T_0 \\ T_1 \\ \vdots \\ \vdots \\ T_K \end{bmatrix} + \begin{bmatrix} \frac{d_1^2}{12} & \frac{-d_1^2}{12} & 0 & \dots & 0 \\ 0 & \frac{d_2^2}{12} & \frac{-d_2^2}{12} & \dots & 0 \\ & & \ddots & \ddots & \\ 0 & 0 & \dots & \frac{d_K^2}{12} & \frac{-d_K^2}{12} \\ 0 & 0 & \dots & \dots & 0 \end{bmatrix} \frac{d}{dt} \begin{bmatrix} T_0' \\ T_1' \\ \vdots \\ \vdots \\ T_K' \end{bmatrix} \\ &= \begin{bmatrix} -\varkappa(z_0) & \varkappa(z_1) & 0 & \dots & 0 \\ 0 & -\varkappa(z_1) & \varkappa(z_2) & \dots & 0 \\ & & \ddots & \ddots & \\ 0 & 0 & \dots & -\varkappa(z_{K-1}) & \varkappa(z_K) \\ 0 & 0 & \dots & \dots & 0 \end{bmatrix} \begin{bmatrix} T_0' \\ T_1' \\ \vdots \\ \vdots \\ T_K' \end{bmatrix}, \end{aligned} \tag{4.28}$$

with $c_1 = -(K_i + \varsigma_{\mathrm{L},i}(\psi_{\mathrm{sky},i} L^{\downarrow}_{\mathrm{sky},i} + L^{\downarrow}_{\mathrm{env},i}) + H_i)/\lambda_1$ and $c_2 = \epsilon_i \sigma T_0^3/\lambda_1$. Equations

[1] While for thick roads this is a realistic boundary conditions, for walls and roofs this implies that the indoor environment must be kept at a constant temperature through HVAC. Modelling the heat output from HVAC should thus be considered in the future.

(4.27) and (4.28) can be compactly written in the following form:

$$\begin{aligned} A\mathbf{T}' &= \mathbf{b} + B\mathbf{T}, &(4.29)\\ C\frac{d}{dt}\mathbf{T} + D\frac{d}{dt}\mathbf{T}' &= E\mathbf{T}'. &(4.30) \end{aligned}$$

After rearranging and substitution of (4.29) into (4.30) we obtain;

$$(C + DA^{-1}B)\frac{d\mathbf{T}}{dt} = EA^{-1}B\mathbf{T} + EA^{-1}\mathbf{b}, \tag{4.31}$$

where $^{-1}$ indicates matrix inversion. Note that we have assumed here that $\mathbf{b}$ does not change during the integration step for simplicity. Time integration is done with a fully implicit backward Euler step. Defining $F = C + DA^{-1}B$, $G = EA^{-1}B$ and $\mathbf{c} = EA^{-1}\mathbf{b}$ this results in

$$F\frac{\mathbf{T}^{n+1} - \mathbf{T}^{n}}{\Delta t_{\mathrm{E}}} = G\mathbf{T}^{n+1} + \mathbf{c}, \tag{4.32}$$

which can be rearranged as

$$\mathbf{T}^{n+1} = (F - G\Delta t)^{-1}(F\mathbf{T}^{n} + \mathbf{c}\Delta t_{\mathrm{E}}), \tag{4.33}$$

where Δt_{E} is the time-step between updates of the surface energy budgets. Note that the terms in c_1 are based on the temperatures from the previous time-step. This is necessary to avoid iteration over all facets during time integration, but should be considered when choosing Δt_{E}.

Ground heat flux In this scheme the heat flux into the building interior or into the ground (G_i) is analogous to the surface conductive heat flux and can be calculated as

$$G_i = \lambda(z_K)T'_K. \tag{4.34}$$

4.4.1 Surface energy and water budget of vegetated surfaces

The surface energy budget of vegetated surfaces follows the description in section 4.4 very closely. Since no tall vegetation is currently being considered, we represented vegetated surfaces as normal facets. The facet properties can be chosen accordingly, e.g. green roofs are often thicker than conventional roofs and vegetation albedo differs from building materials. To represent the additional roughness introduced by vegetation z_0 and z_T can be adapted.
Additional to the terms in Eq (4.17) the latent heat flux E is being introduced:

$$K_i + L_i(T_0) + H_i(T_0) + E_i(T_0) + G_i(T_0) = 0, \tag{4.35}$$

The values of E are the time mean fluxes provided by the wall function for moisture and are based on the surface properties from the previous time-step.
The soil moisture content is then updated according to the water balance of facets:

$$W_{\mathrm{G},i}^{n+1} = \max\left(0, W_{\mathrm{G},i}^{n} + \frac{E_i}{L_\mathrm{v}}\Delta t_\mathrm{E} + P^n\right), \tag{4.36}$$

where L_v is the latent heat of vaporization and P^n is the additional water supply during this time-step. Furthermore the terms for plant canopy resistances, soil resistance and relative humidity at soil level used in the wall function for moisture (3.5.2) are adjusted based on the new values of the green roof temperature, soil moisture and radiation.

4.4.2 Integration into LES

The modified version of DALES, including immersed boundaries, wall functions and the surface energy balance is called DALES-Urban. A schematic how the surface energy balance is implemented can be seen in Fig 4.13. The calculation of the energy and water budget is not done at every LES time-step (Δt), since the timescales associated with the facets[1] are generally much larger than the atmospheric ones. The routines to update the energy balance are thus only invoked after several Δt. In every iteration of the main routines the surface fluxes are thus accumulated. If

[1] LES timescales are usually in the order of tenths of seconds while it takes roughly two minutes to heat a 1cm thick layer of concrete by 1K assuming a high heat storage flux of 200W m^{-2}.

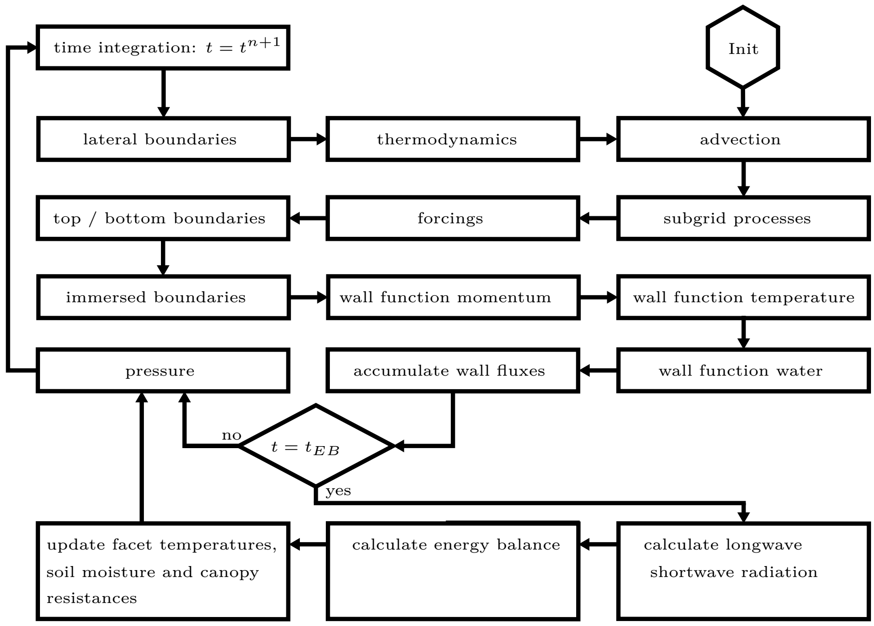

Figure 4.13: Schematic of the main routines in DALES-Urban including the energy and water balance of the surface facets.

between two energy balance time-steps m LES time-steps occur, the mean latent and sensible heat fluxes during that time period can be calculated as

$$E_i = \frac{1}{\Delta t_\mathrm{E}} \sum_{k=1}^{m} E_i^k \Delta t^k, \tag{4.37}$$

$$H_i = \frac{1}{\Delta t_\mathrm{E}} \sum_{k=1}^{m} H_i^k \Delta t^k. \tag{4.38}$$

Further, the external forcings such as water supply (P), solar irradiance (I), total diffuse sky radiation (D_sky) and longwave sky radiation ($L^{\downarrow}_\mathrm{sky}$) have to be known for every energy balance time-step. After m time-steps the longwave and shortwave budget are computed, the water budget is calculated according to Eq. (4.36) using the values obtained from Eq. 4.37 & 4.38. The new facet temperatures are calculated following Eq. (4.33) and subsequently the facet properties are updated accordingly.

4.4.3 Verification of the conductive heat flux and facet temperatures

To verify the proposed model to close the surface energy balance and obtain the wall heat flux, an idealised case has been studied: a single wall with thickness $d = 36\,\mathrm{cm}$, uniform thermal conductivity $\lambda = 0.615\ \mathrm{W\,m^{-1}\,K^{-1}}$ and thermal diffusivity $\varkappa = 2{\cdot}10^{-7}\ \mathrm{m^2\,s^{-1}}$. These material properties correspond to a generic brick wall. The inner boundary of the wall was kept at a constant temperature T_B=300K and an idealised temperature flux corresponding to a mid-latitude summer day of $\phi_\mathrm{s} = \phi_0 \cos(\omega t)$ was applied to the surface, with $\phi_0 = 5 \cdot 10^{-5}\mathrm{K\,m\,s^{-1}}$ and earth angular velocity $\omega \approx 2\pi/(86400\mathrm{s})$. For such a case exists an analytical solution of the form:

$$T(z,t) = T_B + \frac{\phi_0}{\varkappa}\sqrt{\frac{\varkappa}{\omega}} \exp\left(-z\sqrt{\frac{\omega}{2\varkappa}}\right) \cos\left(\omega t - z\sqrt{\frac{\omega}{2\varkappa}} - \frac{\pi}{4}\right). \tag{4.39}$$

Apart from comparing with the analytical solution, our wall model will be compared to a conventional scheme based on second order finite difference method in space and 4$^{\text{th}}$-order Runge-Kutta time integration method. The comparison was done in MATLAB. The time series of the surface temperature and the temperature profiles inside the wall can be seen in Figure 4.14. Using eight layers or more, both methods clearly capture the temperature profile closely and give accurate estimations of the surface temperatures. With fewer layers the new method performs better in predicting the surface temperature, yet with less than four points (3 layers) the piecewise quadratic splines don't represent the internal temperature profile very well. The proposed method works well and performs similar to a standard finite difference scheme but allows us to directly impose the energy balance at the surface without interpolation Figure 4.15(a) shows the relative root-mean-square errors of the surface temperature (RMSE $\mathrm{T_s}$) and the entire temperature profile (RMSE T) over the course of one day. The scheme is second order accurate in terms of spatial discretisation. For large numbers of layers the error become basically constant, but small. This can be explained by the fact that the analytical solution is only valid for an infinitely thick wall and a small error is thus introduced at the interior side of the wall. This is also supported by the fact that surface temperatures are captured more accurately than the entire profile. The time integration is numerically stable and large time-steps can be chosen. The root-mean-square errors depending on Δt can be seen in 4.15(b). The relationship is linear. The time required to solve the energy balance also depends on the number of points as can be seen in Figure 4.16. The time constraint comes from the matrix inversion or matrix left division which is computationally expensive for large matrices. The deviation from the linear relationship for very small numbers of layers is caused by the large percentage of total execution time spent on overhead. The time spent on looping over the number of layers is small, while e.g. the time for MATLAB to compile the script and allocate auxiliary variables remains nearly unchanged.

From this analysis we recommend using four to eight points in a typical wall, since less lead to inaccuracies and more increase the computational cost without providing much benefit. While there is no clear constraint for the time intervals we can for example choose that the typical temperature changes close to the surface are in the order of $\Delta T = 1\mathrm{K}$ for a given expected change of surface energy flux (ϕ') within said time interval. The penetration depth Δd associated with the time Δt_{E} is given by

$$\Delta d = \frac{\sqrt{2}}{\sqrt{\frac{1}{\Delta t_{\mathrm{E}} \varkappa}}} \tag{4.40}$$

We can then approximate the heat stored during time Δt_E and compare it to the change in surface flux during that time:

$$\Delta T \cdot A \cdot \Delta d \cdot \rho_c c_{\mathrm{c}} = A \cdot \phi' \cdot \rho_c c_{\mathrm{c}} \cdot \Delta t_{\mathrm{E}} \tag{4.41}$$

where A is an area and $\rho_c c_{\mathrm{c}}$ is the product of density and specific heat capacity of the wall. These terms drop out and are just for clarification. Solving for Δt_{E} yields

$$\Delta t_{\mathrm{E}} = \frac{2\varkappa \Delta T^2}{\phi'^2} \tag{4.42}$$

For above wall properties and an estimate of $\phi' = \max(\frac{d\phi_0}{dt}) \cdot \Delta t_E$ that results in a $\Delta t_E \leq 3100\mathrm{s}$. For an LES case where wall fluxes vary more substantially in a short time, the resulting timescales are $\Delta t_E \leq 360\mathrm{s}$.

4.5 Verification of the surface energy balance in DALES-Urban

To study the behaviour of the surface energy balance in DALES-Urban a simple case has been set up. The boundary conditions are periodic in x and y and a zero-flux boundary is imposed at the top. The geometry and shading pattern are shown in Figure 4.17. The focus here lies in the interaction of LES, wall function and surface

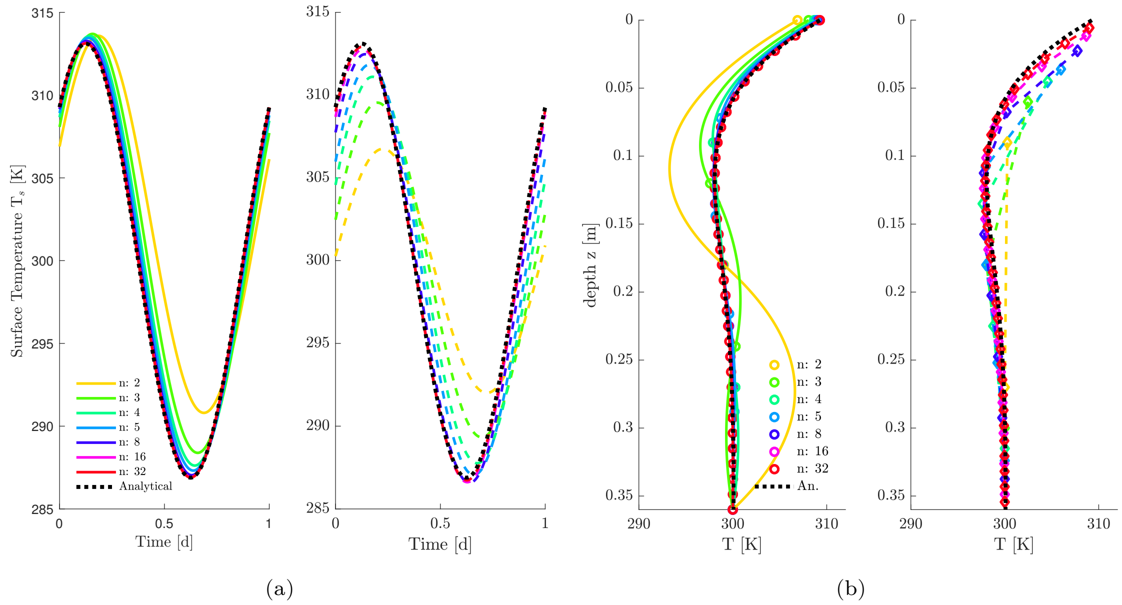

FIGURE 4.14: Proposed method to calculate the wall heat flux and surface energy budget (full lines) compared to a standard finite difference approach (dashed lines) and the analytical steady state solution (black). a) Surface temperature evolution. b) Temperature profiles at midday.

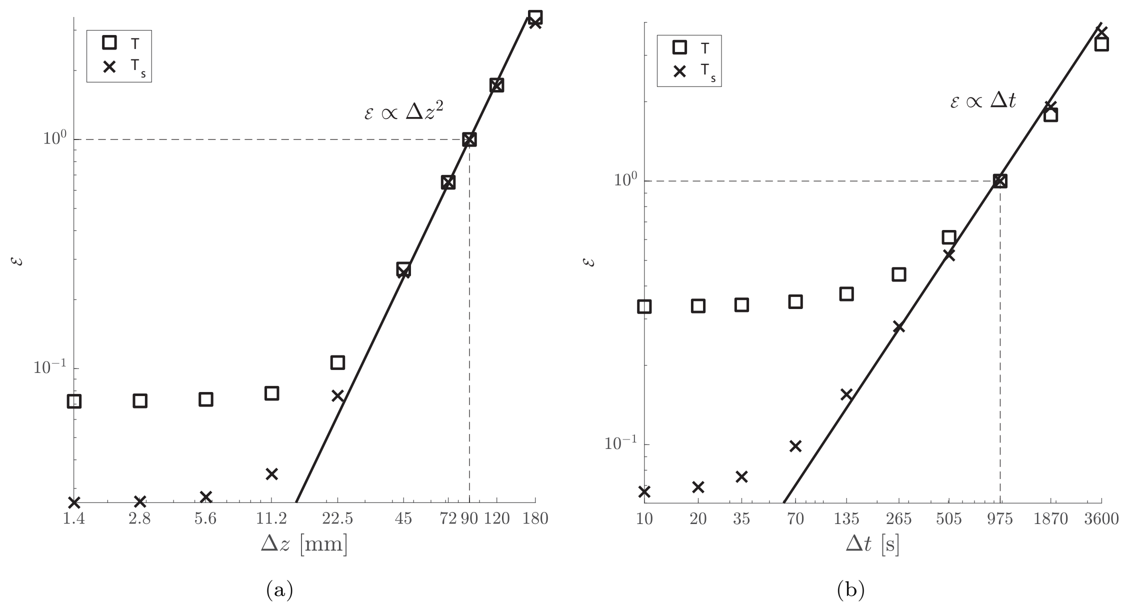

FIGURE 4.15: Relative root-mean-square error ($\mathcal{E}$) of the method (see section 4.4) to calculate ground heat flux for varying numbers of wall layers (a) and time-step (b).

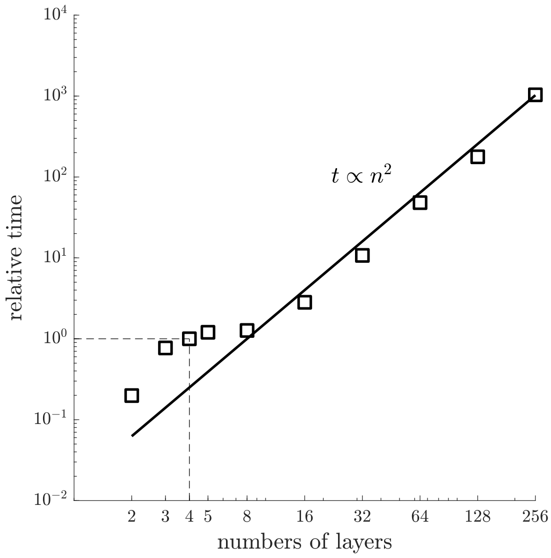

FIGURE 4.16: Runtime of the method (see section 4.4) to calculate ground heat flux for varying numbers of wall layers.

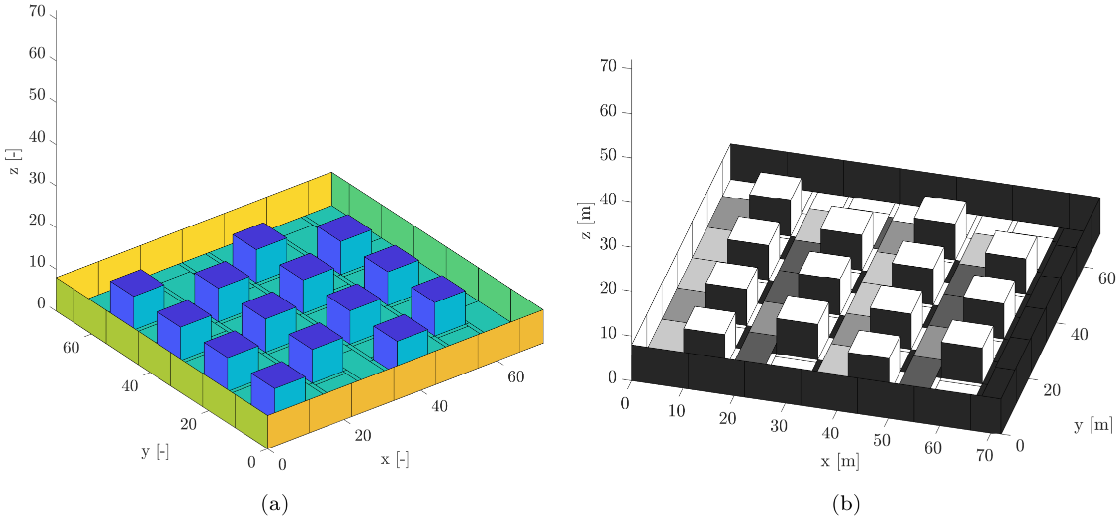

FIGURE 4.17: Geometry and shading of the surface energy balance test case. The facets are coloured based on their type and orientation: Wall north Wall west Wall south Wall east Floor Block south Block west Block top.

Table 4.2: Scenario parameters for the verification of the SEB in DALES-Urban. The solar and radiation settings roughly correspond to Miami, Fl at 10:30 on July 25 (Jenkins, Thomas and Bolivar-Mendoza, Gabriel, 2018). The material properties correspond to concrete (The Engineering Toolbox, 2018).

Property	Value
Domain size	$72 \times 72 \times 72$m
Solar elevation	45°
Solar azimuth	90°, E
I	750W m^{-2}
D_{sky}	100W m^{-2}
$L^{\downarrow}_{\mathrm{sky}}$	200W m^{-2}
Facet albedo	0.5
Facet emissivity	0.85
Nr. of wall layers	3
Wall thickness	3×0.1m
Road thickness	3×0.33m
Freestream velocity U	2m s^{-1}
Building temp.	301K
Initial air temp.	300K

energy balance. The sensible heat flux H is calculated by the wall function at every LES time-step ($O(1s)$) and the heat is added/removed from the fluid. This flux is integrated between energy balance time-steps by using Eq. (4.38) with $\Delta t_{\mathrm{E}} = 300$s. For the boundary conditions chosen, the temperature change of the fluid has to equal the total energy flux from the surface. Figure 4.18 shows that the sum of the sensible heat fluxes from all facets indeed matches the internal energy change precisely. This confirms that the heat fluxes from the wall are correctly added to the fluid cells in DALES-Urban.

Figure 4.19(a) shows the temperature evolution of all facets. It is evident that the temperatures will largely be influenced by the solar radiation, accordingly east-facing facets are the warmest. Furthermore, one of the roof facets was given green roof properties, resulting in lower surface temperatures and it clearly stands apart from the other roofs. Figure 4.19(b) shows the surface fluxes of a single road facet. Net shortwave radiation K is unchanged throughout the simulation and L only varies slightly since most facets don't experience a large surface temperature change. The sensible heat flux H show fluctuations due to the turbulent nature of the flow. Figure

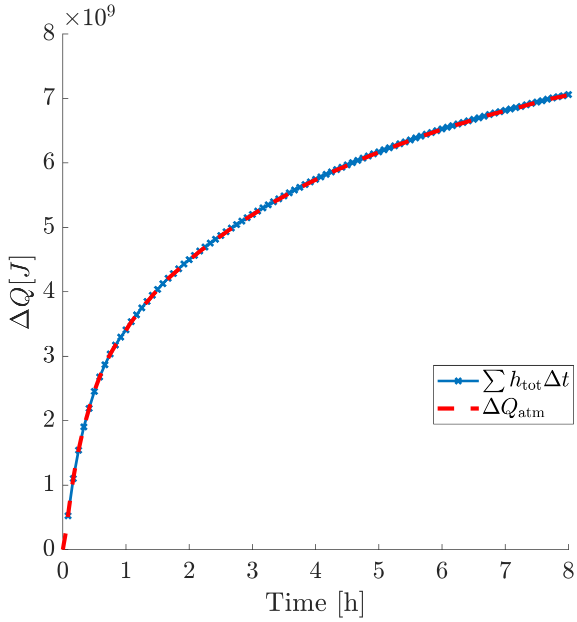

Figure 4.18: Total accumulated heat flux from all facets ($\sum h_{\text{tot}}\Delta t$) compared to the total energy change in the air (i.e. air temperature, ΔQ_{atm}) for the simulation case described in section 4.5.

4.19(b) also demonstrates that the net flux ($K + L + H$) matches the ground heat flux / surface temperature gradient ($\lambda \frac{\partial T_s}{\partial z}$) predicted by the energy balance, verifying that the energy balance is correctly linked to the wall functions.

Comparison to MTEB The case presented in this section is very idealised and is thus well suited to be studied with the MTEB model from chapter 2 as well. Most of the parameters can be carried over directly. Solar/radiation properties, air temperature and surface properties are identical to Table 4.2. To obtain the idealised canyon geometry in MTEB we can consider the total area covered by buildings and roads. This results in a building width $b = 72 \cdot (14 \cdot 8^2)/(72^2) = 12.44$m, canyon width $l = 72 - 12.44 = 59.56$m and a building height $h = 8$m. The initial surface temperatures in MTEB were chosen to be the mean of the corresponding facets in DALES-Urban. The energy balance of the entire domain is determined by the balance of the net shortwave and net longwave at the top. The effective albedo of the morphology can be calculated in DALES-Urban since the absorbed shortwave of all facets and the incoming shortwave at the top is known. Whereas all the facets have an albedo of 0.5 the resulting effective albedo is ≈ 0.35 due to radiation trapping. In MTEB the resulting effective albedo is 0.37 and thus in good agreement. The net longwave on the other hand evolves during the simulations since the surface

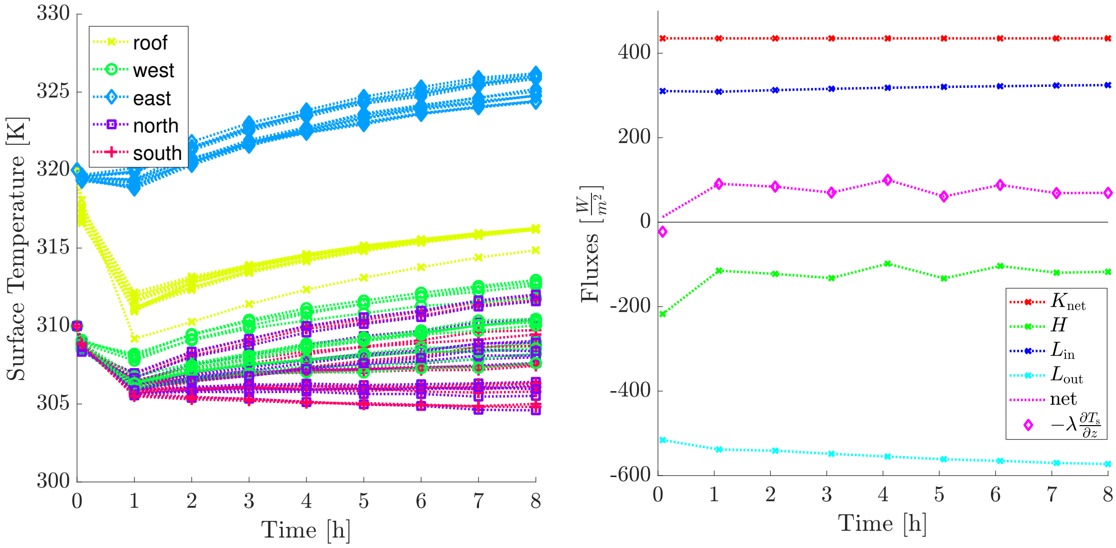

(a) (b)

Figure 4.19: Temperature evolution of all building facets (a) and all the energy fluxes of a single floor facet (b). Shown are initial values, the mean over the first 300s and the 300s-means leading up to every full hour. For the simulation case described in section 4.5. The orientation of the facets can be seen in Fig 4.17(a): $\mapsto$, $\mapsto$, $\mapsto$, $\mapsto$, $\mapsto$.

temperatures change. Figure 4.20 shows the total energy in the system over time for both the DALES-Urban and MTEB runs. The canyon in MTEB does not have a heat capacity, this leads to an initial jump of energy in the system at the start of the simulation. Over time the two curves agree well. Since the two models are completely independent this is a good indication that the surface scheme in DALES-Urban produces plausible results.

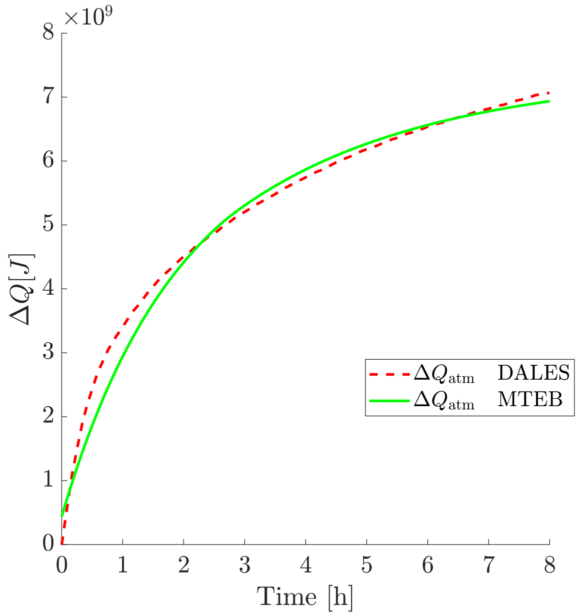

Figure 4.20: Comparison between DALES and MTEB of the total energy change of the air over time.

5
Demonstration of model capabilities

5.1 Introduction

To highlight the capabilities of the model developed in this dissertation, this chapter discusses the effect the installation of a green roof on a single building has on the local microclimate. Green roof installations are often considered to be beneficial for the local climate and were a focus of the Blue-Green dream project. As part of this project, a green roof was installed on an auxiliary building of Imperial College London, called “Eastside”. Other PhD research projects are and were concerned with the green roof performance, studying different vegetations or how to achieve better integration of such building measures in architectural and planning processes. The green roof is also instrumented with various measurement devices for atmospheric and soil properties. A detailed validation of DALES-Urban against measurements is beyond the scope of this thesis. “Eastside” nevertheless offers a good opportunity to employ the new version of DALES-Urban and investigate the effect of a green roof on the air flow and temperatures in its vicinity.

5.2 Case set-up

The test area is the Imperial College campus in South Kensington, London. The green roof was installed on the “Eastside” building (see Fig. 5.1). The meteorological conditions were those of 21st June 2017, the hottest day in Heathrow, London in 2017.

Figure 5.1: Top: “Eastside” building (orange box) and surrounding in South Kensington, London from Google Maps (2018). Bottom: LIDAR data of the same area from UK Environment Agency (2018).

Air temperatures reached 35°C at around 16:00h, wind was easterly and the sun was at an elevation of 36° and an azimuth of 130° from north, counterclockwise.
Before the simulation the morphology input files had to be prepared. The building heights were derived from geospatial data. All manipulations of vector data were done with geographic information systems (SAGA GIS & QGIS), and the resulting raster data was refined in MATLAB. Since building height geo-information is not always available for free for all areas the building mask of the British Ordnance Sur-

vey and 50cm resolution LIDAR data of the British Environment Agency (see Fig. 5.1) were used to obtain the building height (EDINA, 2018). Every building was assigned a typical height $h = 0.5(h_{\text{mean}} + h_{\text{max}})$, where h_{mean} is the average height of all the LIDAR pixels within a given building and h_{max} is the maximum height of said building. The resulting structures thus have flat roofs and the heterogeneity that can exist on top of a single building is not captured. The selected area of interest was then cropped and rasterised in the desired resolution. The rasterised data of building heights can in fact be treated as a grayscale image and a MATLAB routine was developed to automate the further image processing. Small gaps along the building walls were closed, small objects and any pixel with only one neighbour removed. Finally, depressions inside buildings (courtyards, etc.) were filled. The result is shown in Figure 5.2. These modifications simplify the landscape and reduce the number of blocks in the domain. A newer version of the pre-processing does not fill large courtyards, since this is not strictly necessary. Yet, small depressions should be removed since the circulation in such enclosures cannot be accurately represented by the LES model.

The buildings were thereafter sliced as explained in section 4.2, the ground was populated with road facets and a bounding wall was created. The results of this division can be seen in Figure 5.3. View factors between the facets were then calculated and stored. For simplicity all facets were assumed to have identical properties shown in Table 5.1. The horizontal domain size is 960m×480m with a resolution of 2.5m in each dimension. Vertically the grid was 2.5m within the canopy and gradually stretched above to a total height of 768m, resulting in 384×192×192 grid points. The simulation (10h) was run on 16 CPUs on a single workstation for $\approx$ 125 hours. The lateral boundary conditions were periodic and 7 hours of neutral conditions were simulated to allow the development of turbulence in the domain. The facets were initialised with outside temperatures corresponding to their radiative equilibrium and a linear internal temperature profile. The radiative equilibrium temperatures are generally too hot and for applied studies of the urban environment it is important to consider these initial conditions carefully. It was assumed that unlimited water for evaporation was available in the soil. The atmosphere was set to a uniform temperature of 300K. The spin-up was then continued for an additional hour to allow the development of thermal effects and convection. After 8 hours two simulations

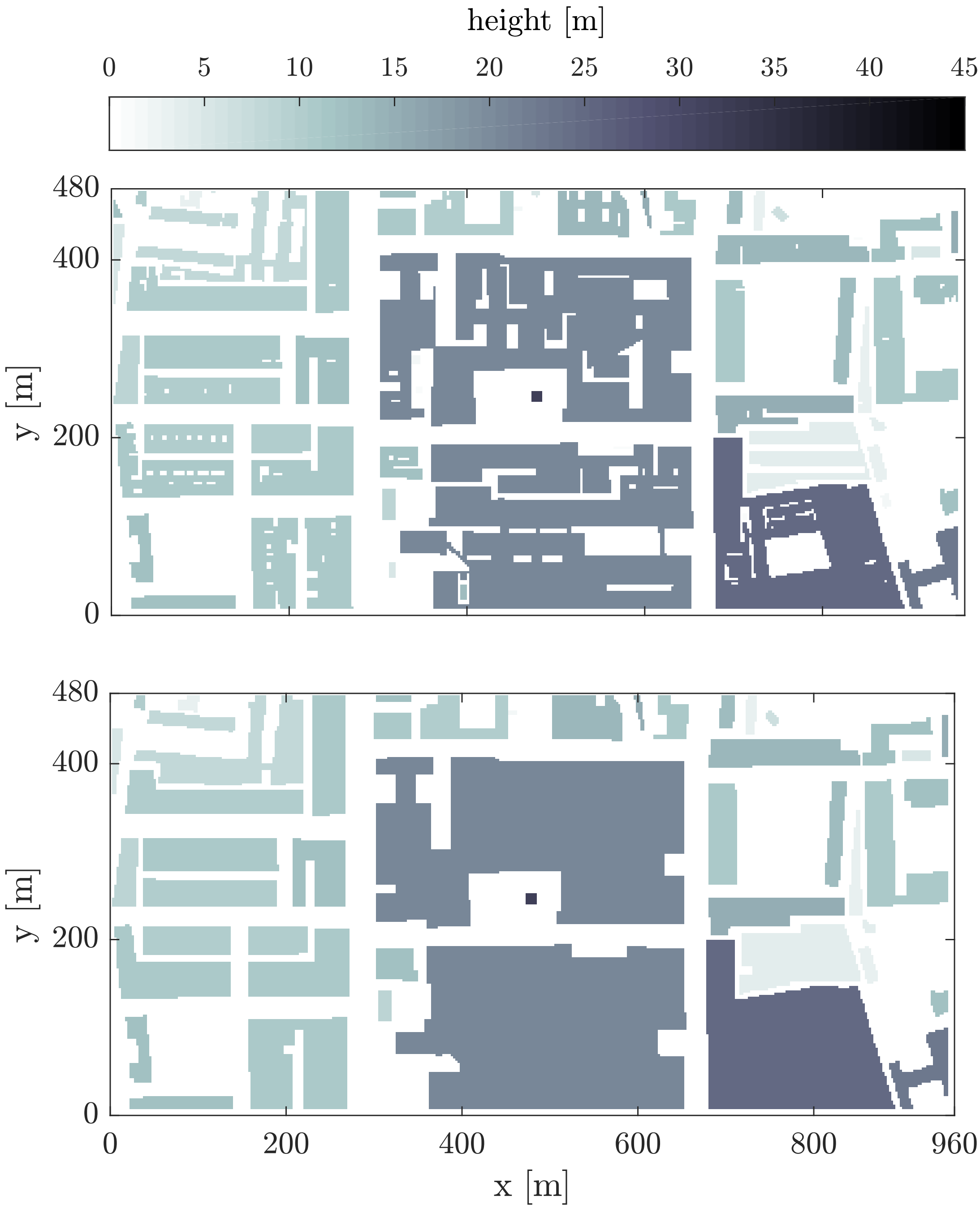

FIGURE 5.2: Original gridded topography (top) and after refinement (bottom). 2.5m resolution of a 960m x 480m area (384×192 pixels).

Wall properties							
z_0 [m]	z_T [m]	α	ϵ	d [m]	ρc_p $[\frac{\mathrm{J}}{\mathrm{m^3K}}]$	λ $[\frac{\mathrm{W}}{\mathrm{mK}}]$	κ $[\frac{\mathrm{m^2}}{\mathrm{s}}]$
0.05	0.00035	0.5	0.85	3×0.12	$2.5 \cdot 10^6$	1	$4 \cdot 10^{-7}$

TABLE 5.1: Wall properties of facets in the "Eastside" simulation. The defined material properties corresponds to concrete (Asadi et al., 2018, The Engineering Toolbox, 2018).

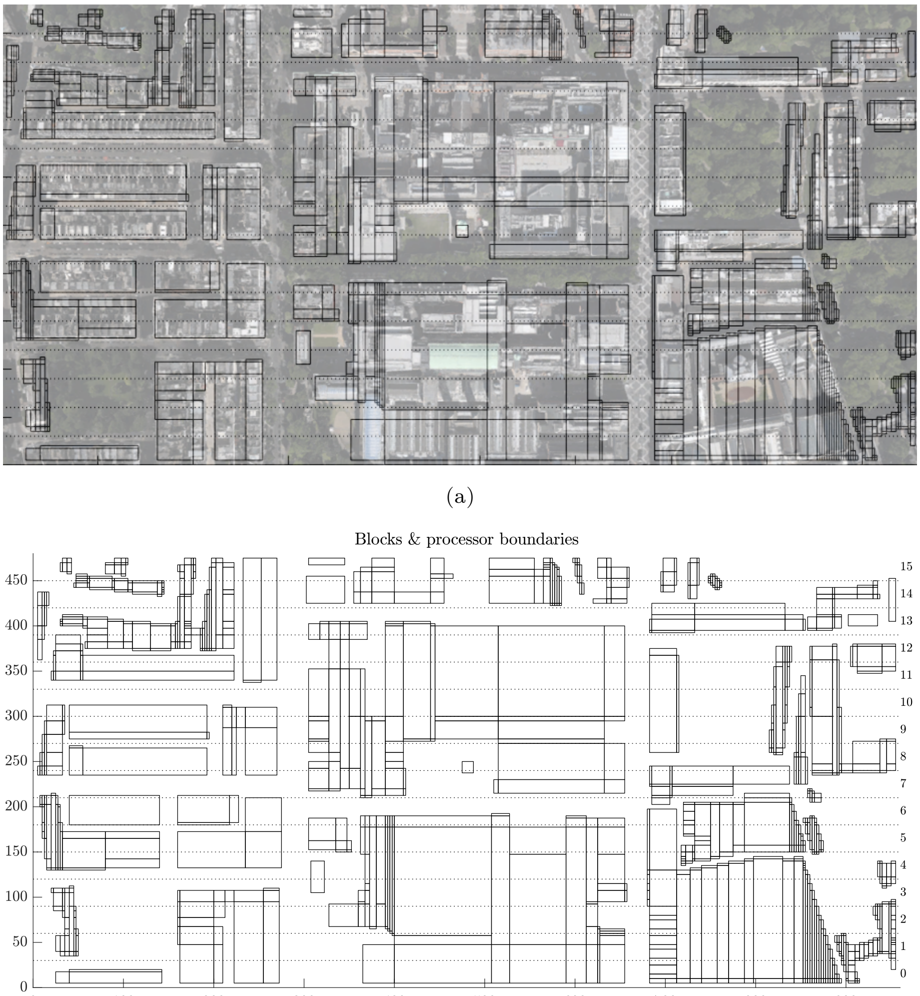

(a)

(b)

Figure 5.3: Morphology of South Kensington Campus and surroundings divided into building blocks and overlaid over aerial image.

with and without green roof on "Eastside" were run for an additional hour and then compared.

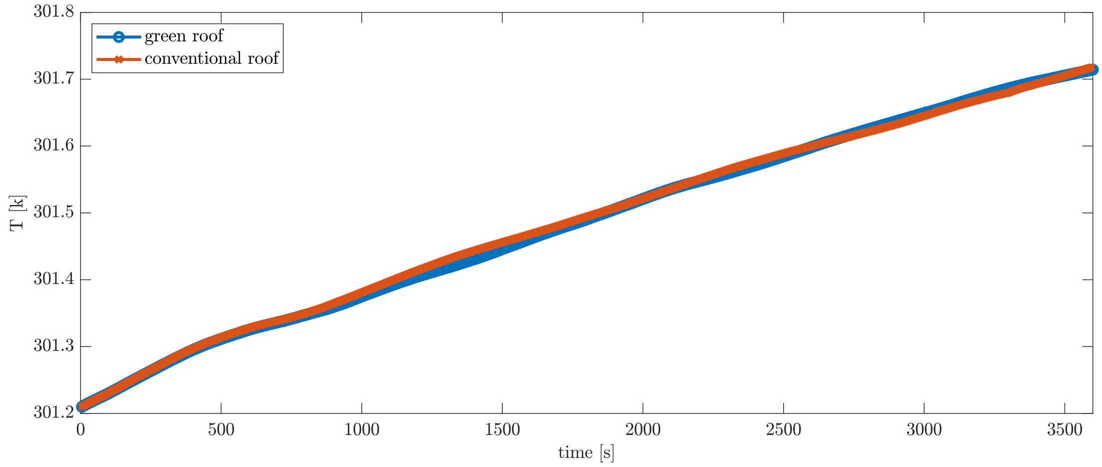

FIGURE 5.4: Domain averaged temperature evolution.

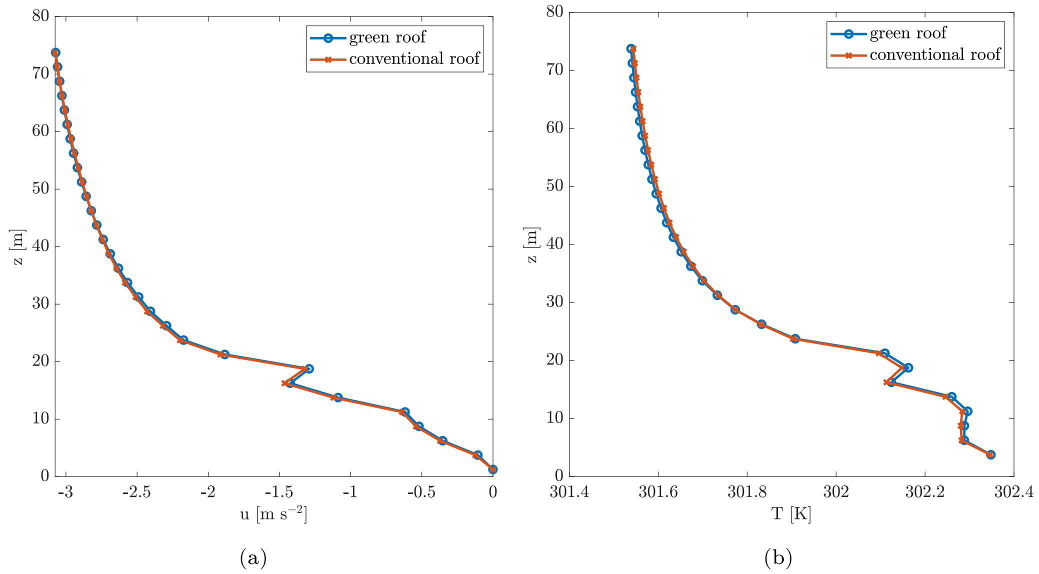

FIGURE 5.5: a) Time and horizontally averaged u-velocity profile for the "Eastside" simulations with and without green roof. b) Time and horizontally averaged temperature profiles.

5.3 Results

Wind It is to be noted that due to the nature of the simulations differences in velocities and scalar quantities can be caused by a number of effects and not just the direct presence of the green roof. The slight perturbation of the initial and boundary conditions can lead to substantial differences after some time and due to the strongly coupled nature of the system complex flow patterns can emerge and turbulent structures can persist for a prolonged period. Furthermore transient processes are present, driven by the slow warming of the entire domain. In Figure 5.4 we can see how the average fluid temperature evolves over time. Since the simulations were periodic in the x- and y-dimension the total amount of energy in the domain increases over time. This is caused by the overall positive radiative energy balance at the surface. The mean quantities of the simulations will consequently evolve over time and ideally ensembles runs would be studied for better statistics. Figure 5.5 shows the time and horizontally averaged u-velocity and temperature profiles for the two runs. It is evident that the presence of the green roof does neither affect the average velocities nor the average temperature in any substantial way, as can be expected. The mean temperatures in the urban canopy even appear to be slightly elevated whereas the temperatures above the obstacles are marginally lower. This could be caused by reduced mixing. Yet, the difference is minuscule and cannot be attributed to the green roof without any further investigation.

Figure 5.6(a) shows the streamlines of the u and w components of the velocity field for the simulation with a conventional roof. In slice 2 in the centre of the "Eastside" building a clear recirculation area can be identified on the leeward side of the building. On the northern edge the recirculation zone is pressed against the building, while it moves away from the building and dissolves completely on the southern end. This is caused by a slightly northerly wind in the building wake leading to diverging flow on the southern side and a complete breakup of the recirculation there. This effect is somewhat more pronounced in the simulation with green roof (Fig 5.6(b)). In this case the streamlines of slice 1 all skim over the building downstream of "Eastside". In addition to the streamlines, the w-velocity differences between the two cases are shown as contour slices. The vertical velocities at the southern end are more positive for the green roof case, whereas w is generally more negative at building height an below on slice 3. In the simulation with green roof the flow thus exhibits stronger convergence in the northern part of the courtyard and correspondingly stronger divergence on the southern end. However, this effect is most likely not directly caused by the green roof. Larger scale flow patterns dominate over the localised roughness and buoyancy effects of the vegetation. The large impact of both corners and the alignment of buildings and gaps on the flow demonstrates that air flow around 3D structures is complex and that CFD models are necessary to accurately capture the flow in an urban environment. Indeed, the flow cannot be categorised as one of the three canonical flow regimes for uniformly spaced buildings (isolated roughness flow, wake interference flow and skimming flow; Oke (1988)).

In Figure 5.7(a) the one hour mean u velocity profiles upstream, on top and downstream of “Eastside” are shown. The profiles are generally very similar. The differences in the approaching flow are difficult to interpret and likely only indirect effects of the green roof as mentioned in the initial sentences of this paragraph. Also the fact that the green roof is rougher is not clearly evident. This is also not to be expected, since the roof is simply to short for the flow to lose a considerable amount of momentum. Comparing the three profiles at location c) gives another view on the flow pattern in the building wake. In profile 1c the u velocities are near zero. Profile 2c reveals the clear recirculation, with a $u > 0$ reverse flow close to the bottom. Whereas 3c exhibits negative u-velocities throughout the building wake, with slightly higher velocities for the green roof case.

Air temperature and humidity While cooler roof temperatures can be significant for indoor climate, most of the outdoor activities take place on street level. LES is ideal to study how the air from above the roofs is transported and mixed throughout the atmosphere. In Figure 5.7(b) the one hour mean temperature profiles upstream, on top and downstream of the “Eastside” are shown. All profiles clearly show convective conditions, with the warmest temperatures closer to the surface. The green roof case shows a constant mean temperature or even a small decrease from location a to b on the lowest level (1.25m above the roof). This indicates that the heat flux from the vegetated surface is smaller than the average the approaching flow previously encountered. The conventional roof on the other hand generally shows an increase from location a to b in temperature of the first level.
Figure 5.8(a) shows the difference between one-hour means of the temperature fields from a simulation with and without the green roof. It is evident that air temperatures change much less than the 10K change of the facet temperatures, even directly above the vegetated surface. The time an air parcel takes to pass over the area is in the order of seconds, limiting the amount of heat that can be exchanged. Maximum air temperature reductions are thus in the order of 1K. Most of the temperature reduction is focused downstream of the roof at roof elevation. Vertical mixing in the building wake leads to temperature reductions of 0.2-0.3K on street level. The temperature difference on and before the northern leading edge of the green roof is likely either caused due to the periodicity of the system or different time averaged flow behaviour between the two simulations. When studying human comfort humid-

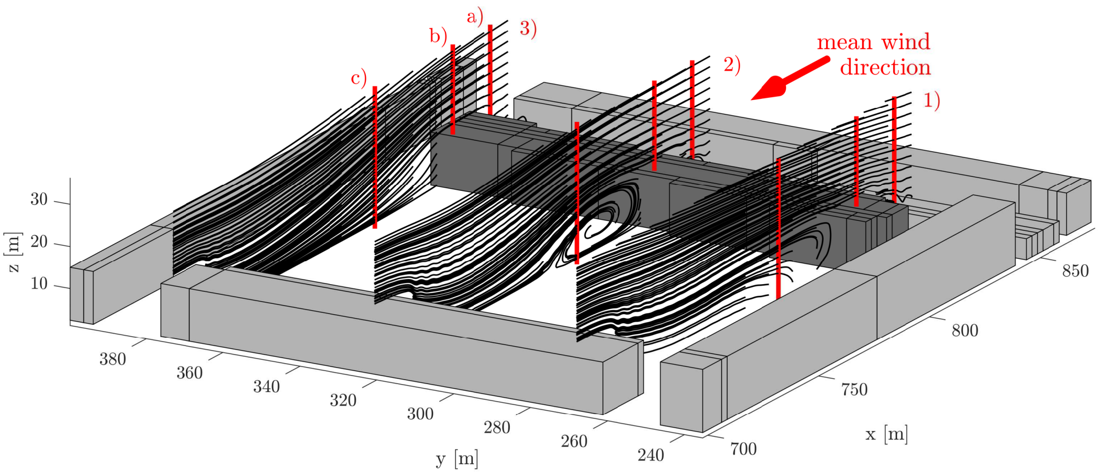

(a) Streamlines conventional roof

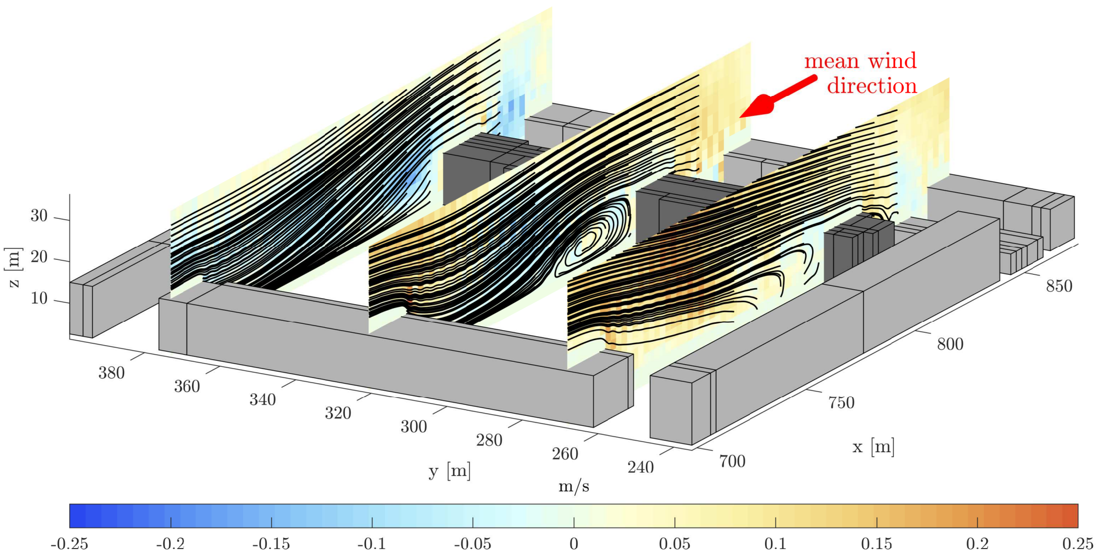

(b) Streamlines green roof & Δw

Figure 5.6: a) Streamlines of the (u, w) velocity field for the simulation with conventional roof. The locations of the velocity profiles in Figure 5.7 are marked in red. b) Streamlines (u, w) for the simulation with green roof and contours for vertical velocity differences ($w_{\mathrm{GR}} - w_{\mathrm{conv.}}$). "Eastside" building coloured in darker grey.

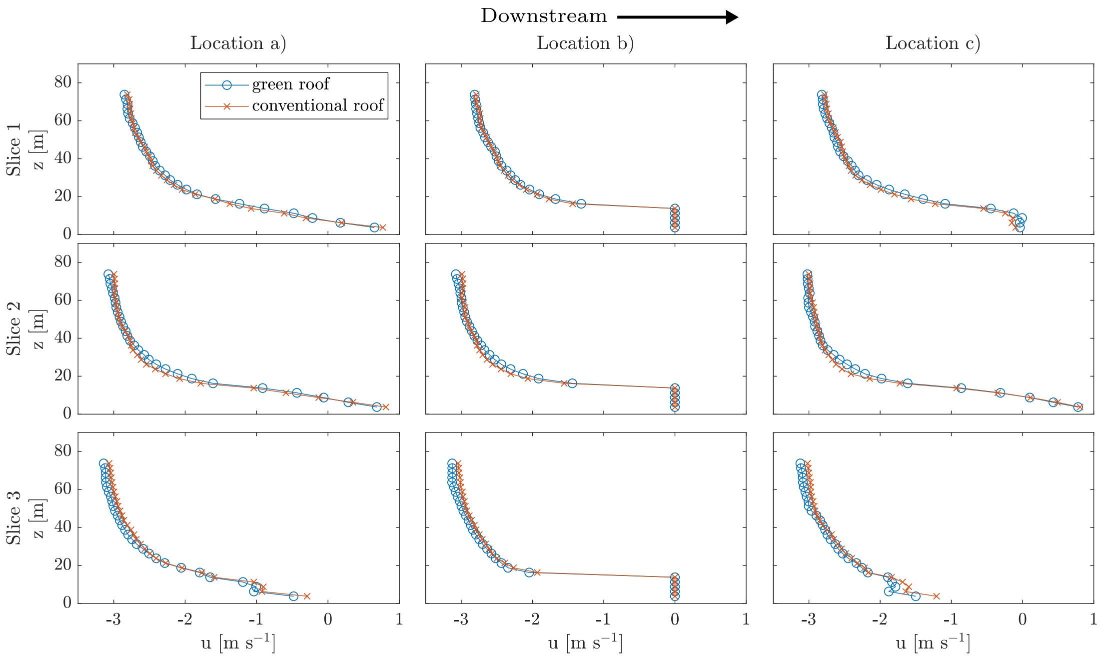

(a) Velocity profiles

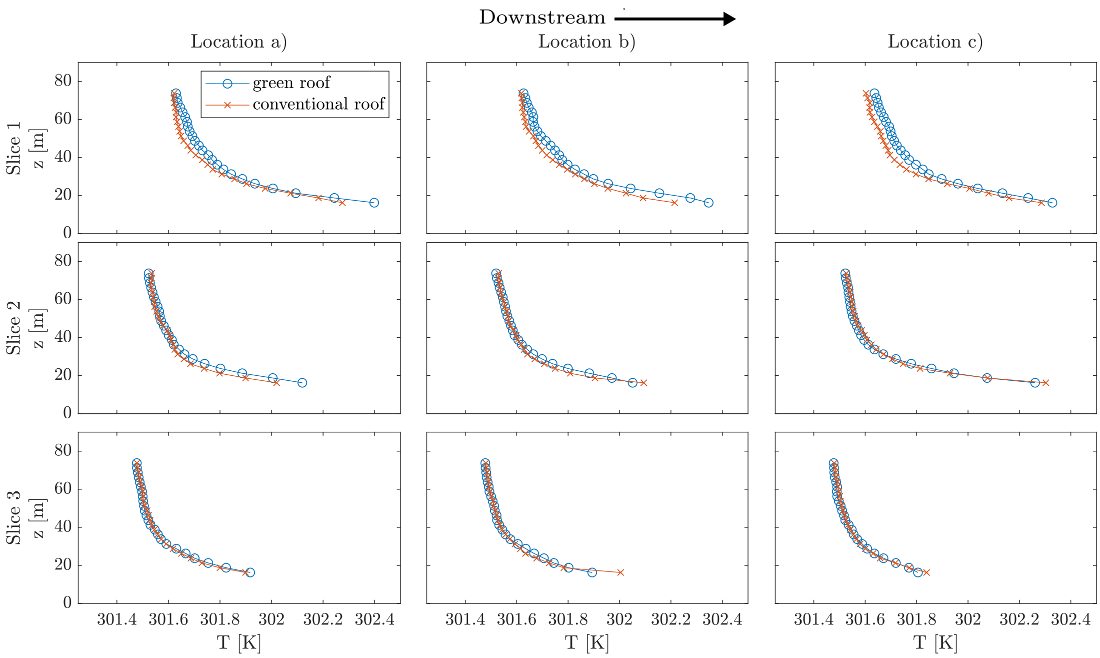

(b) Temperature profiles

Figure 5.7: a) Mean velocity profiles at nine locations around the "Eastside" building. The three profiles in the same row form a group: upstream, on top and downstream of the building. b) Mean temperature profiles at the same locations. The locations of the profiles can be seen in Figure 5.6(a).

ity plays an important factor as well. Figure 5.8(b) shows the difference between one-hour means of the specific humidity field from a simulation with and without the green roof. We can observe clear downward mixing in the building wake. Since there is no other humidity source in the domain, the humidity difference can be attributed entirely to the presence of the green roof. On street level a mean increase in specific humidity of $0.01\mathrm{g\,kg^{-1}} - 0.1\mathrm{g\,kg^{-1}}$ can be observed. This corresponds to a almost insignificant difference in relative humidity, since at 30°C a relative humidity change of 1% equals a specific humidity change of $\approx 0.3\mathrm{g\,kg^{-1}}$.

Facet temperatures Facet temperatures at the end of the simulation are visualised in Figure 5.9(a). Temperature maxima occur in west and south facing walls exposed to the sun, with temperatures up to 335K or 62°C. North and East facing facets on the other hand are close to the air temperature of $\approx 303K$ (not visible). While roofs are exposed to a large shortwave forcing, the sensible heat flux is usually larger than for vertical surfaces due to the higher tangential wind velocities, leading to somewhat cooler surfaces. The green roof stands clearly apart from other roofs; the temperature remains also very close to the air temperature even though it is directly exposed to the sun. The resulting latent heat flux from soil and vegetation leads to a surface temperature reduction of $\approx$ 10K. This can also be seen when comparing the internal temperature profiles of a simulation with and without green roof in Figure 5.9(b). The temperature profiles between the four resolved points were reconstructed following Eq. 4.22. From Figure 5.9(b) it is also evident that the initial temperatures of the roofs were chosen too high and the roof has been cooling down over time highlighting the importance of accurate initial conditions. Yet, this is nearly impossible to avoid since the internal temperature profiles are usually not known and depend on past environmental conditions due to their long associated timescale.

Figure 5.10 shows the temperature evolution and surface energy fluxes of the "Eastside" roof for both cases. The surface temperatures of both the conventional and green roof decrease over the course of the simulation. The temperature reduction is largely driven by the latent heat flux (E) and by the sensible heat flux (H) for the green and the conventional roof, respectively. For the green roof the radiative fluxes on the facet surface almost balance. Net shortwave radiation (K_{net}) does not

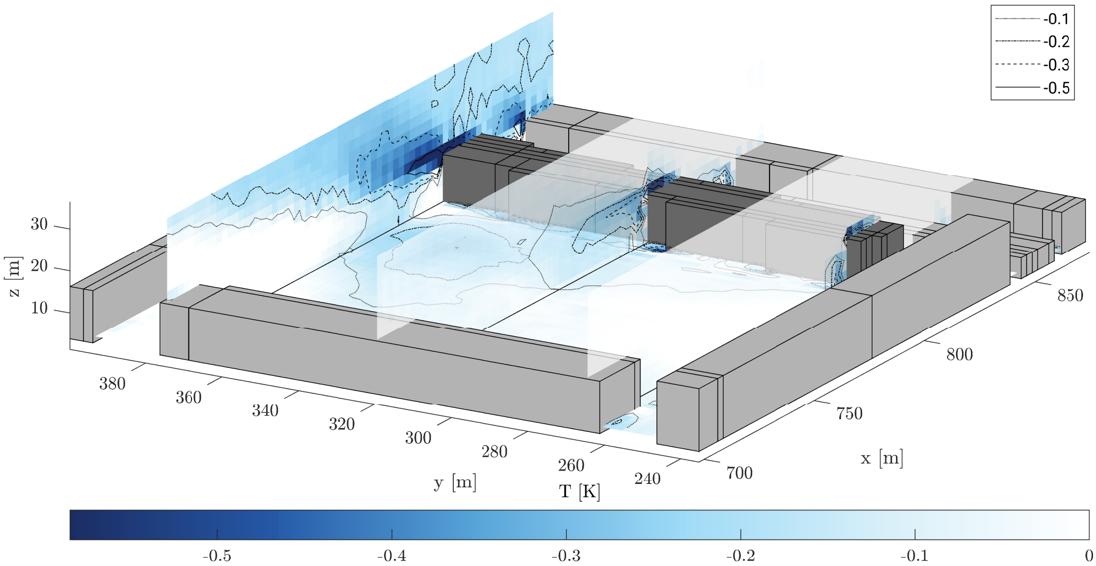

(a) Temperature difference $T_{\mathrm{GR}} - T$

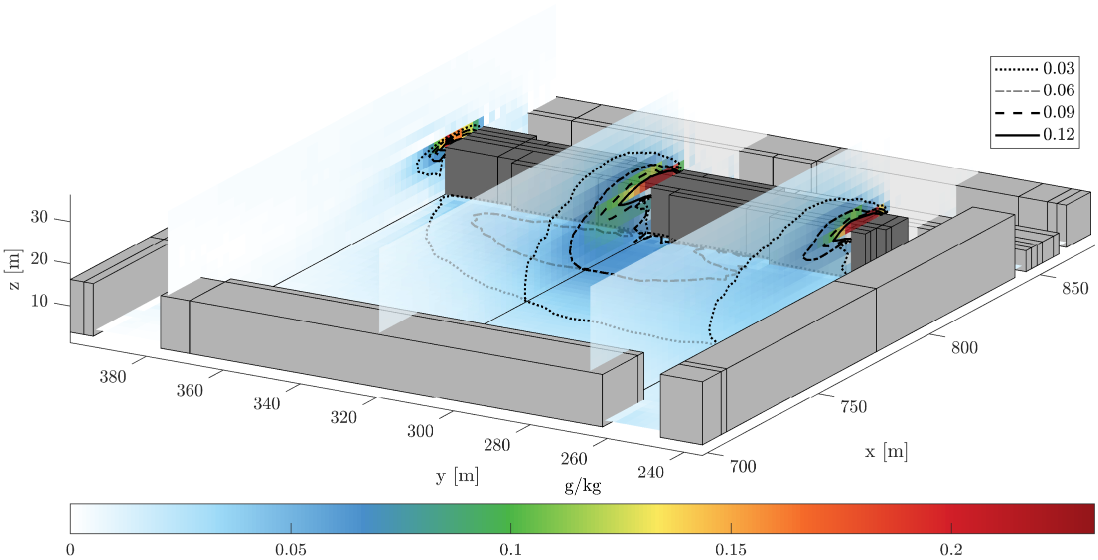

(b) Specific humidity difference $q_{\mathrm{GR}} - q$

FIGURE 5.8: Three vertical and one horizontal slices through difference between one-hour means of simulations with $(T_{\mathrm{GR}}, q_{\mathrm{GR}})$ and without green roof (T, q). "Eastside" building coloured in darker grey.

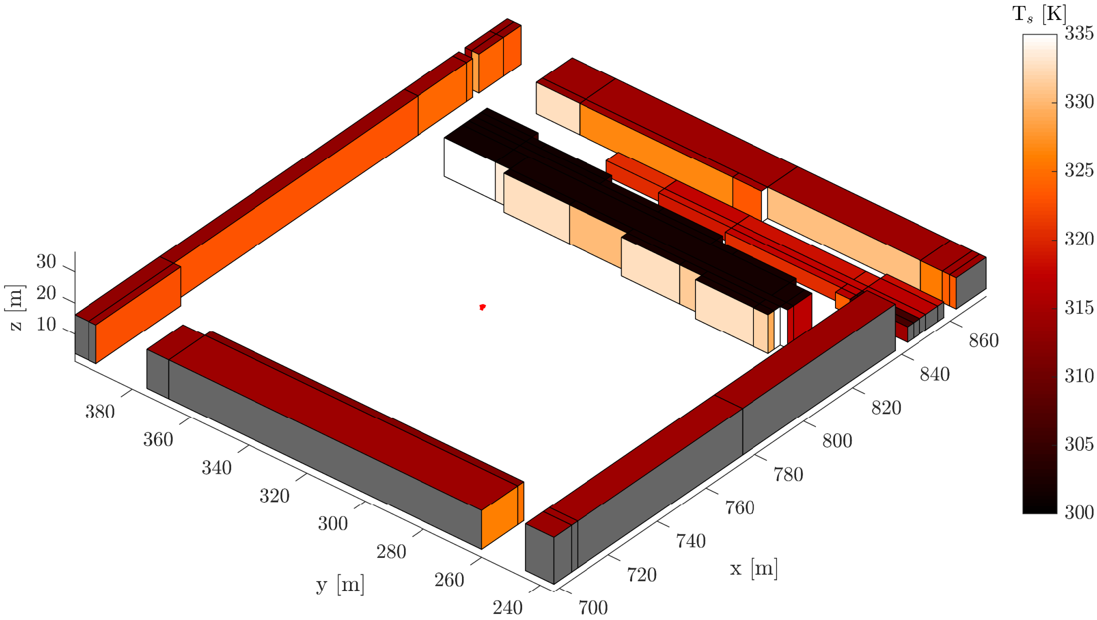

(a) Facet temperatures

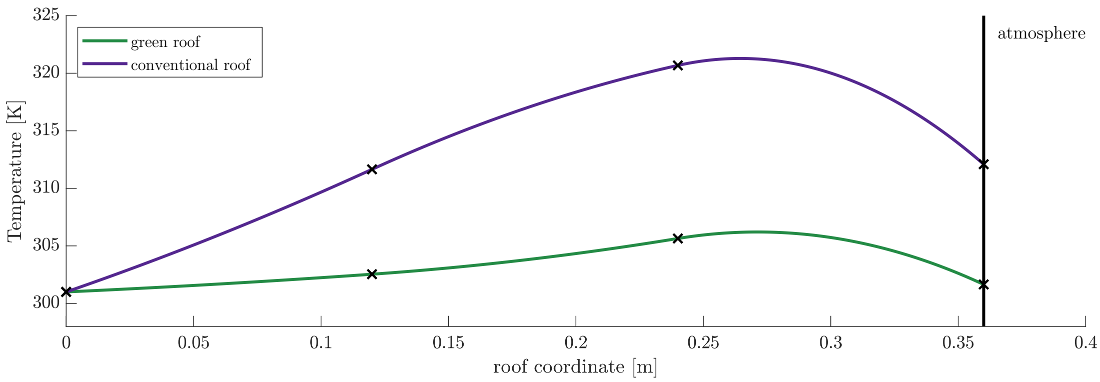

(b) Temperature profiles in roofs

Figure 5.9: a) "Eastside" building and surrounding with building facets coloured based on their surface temperature. Floors are not colored for clarity, grey surfaces are building internal. View from direction of the sun. b) Internal roof temperature profiles for simulations with and without green roof on the "Eastside" building. The roof coordinate is the reverse of the depth z defined in Fig 4.12. It points from the roof interior to the outside.

change during the simulation, since the solar position does not change. There is a minute shift in incoming longwave radiation (L_{in}) due to the temperature change of surrounding facets. However, only a tiny fraction of the field of view of a roof facet on “Eastside” is occupied by other facets; the sky constitutes the largest part. The magnitude of the emitted longwave (L_{out}) follows the Stefan-Boltzmann law and decreases along with the facet temperature. The remaining three fluxes are the surface conductive heat flux ($\lambda\frac{\partial T_{\text{s}}}{\partial z}$), the sensible and the latent heat flux. These three fluxes vary more substantially on short timescales. The surface energy balance was calculated every ten seconds and thus the turbulent fluctuations of the sensible and latent heat flux can still be distinguished. For the green roof the sensible heat flux is relatively small, since the temperature difference to the air is minor. The net energy loss that leads to the cooling is thus caused by evapotranspiration from the vegetation. The latent heat flux is also a function of the temperature difference to the air and we can see a decline over time. For the conventional roof the radiative fluxes are close to balance as well, but no evapotranspiration is possible and $E = 0$. The strong temperature difference initially leads to very large sensible heat fluxes. The large temperature gradient within the roof further causes substantial heat conduction into the roof. As the surface cools down these fluxes also taper off.
In Table 5.2 the surface energy fluxes of the green roof at the end of the simulation are listed together with values from the literature. The value of the incoming longwave radiation appears to be somewhat small compared to Feng et al. (FENG, 2010) and presumably also compared to Heusinger & Weber (HEU, 2017). The site studied by HEU was located in Berlin Brandenburg Airport, Germany, and the summer shortwave radiation is thus comparable to London. However they report a net radiation of 350W m^{-2} contrasting the 82.5W m^{-2} on “Eastside”. The sensible and latent heat fluxes are similar to the values found by FENG for a well irrigated extensive green roof. HEU on the other hand measure over a prolonged time in summer and water was not always available, the latent heat flux is thus small and the Bowen ratio ($\beta = H/E$) is also > 1. However, in general one expects an irrigated green roof to have $\beta < 1$ (e.g. Cirkel et al., 2018). The ground heat flux is comparable and generally relatively small. The residual heat flux leads to a temperature change of the roof. Since the facets of “Eastside” were initially quite hot, the residual is negative and the green roof cools down. This is not to be expected at the warmest point of

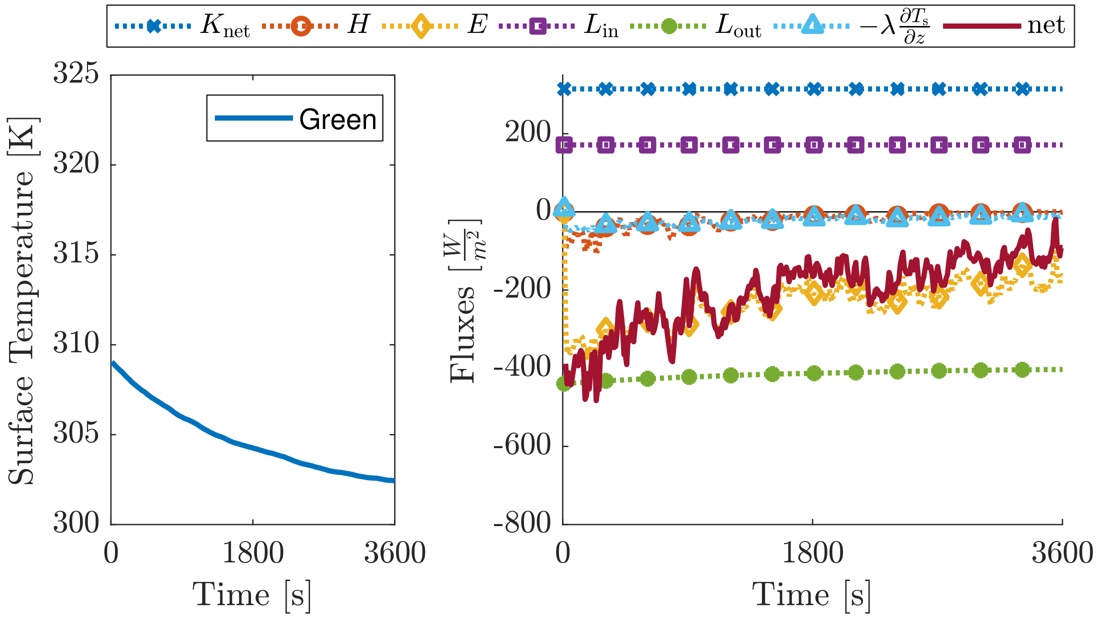

(a)

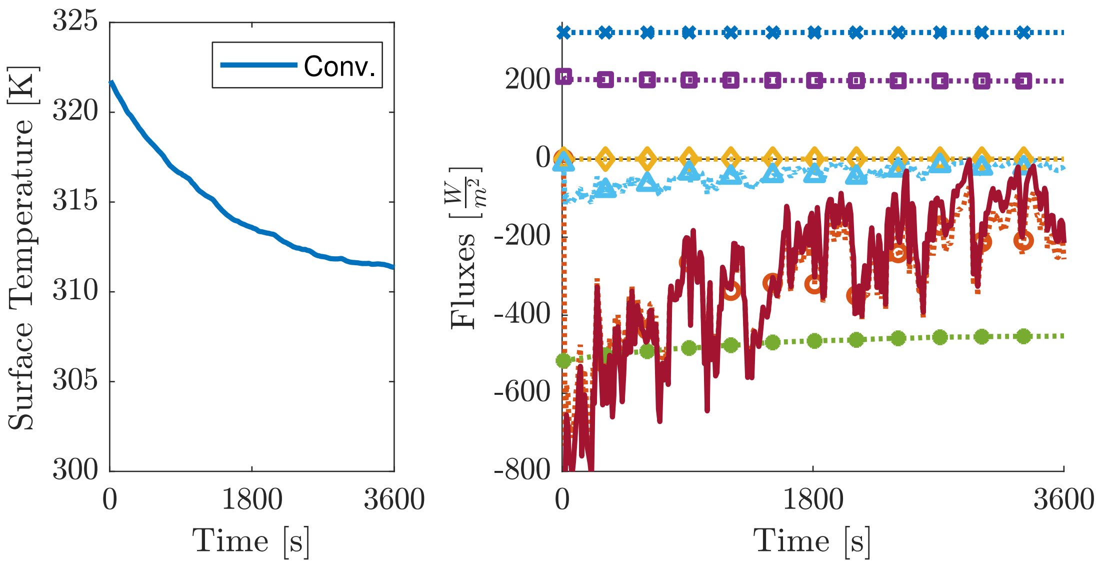

(b)

Figure 5.10: a) temperature evolution of a green roof facet and the corresponding surface energy fluxes. b) temperature evolution of a conventional roof facet and the corresponding surface energy fluxes. The markers are for the sake of clarity, the data was plotted every 10s and the markers do not correspond to particular data points.

the day as also clearly illustrated by the positive residuals in HEU and FENG.

Table 5.2: Energy fluxes of the green roof at the end of "Eastside" simulation compared to values from the literature. All values in W m^{-2}.[1] Heusinger & Weber (2017) only give the total net radiation, including L_{net}.

	K_{net}	L_{in}	L_{out}	H	E	G	residual
DALES-Urban	314.5	171.2	-403.2	-0.2	-163.5	-9.8	-91
Feng et al. (2010)	390	445	-500	-28	-139	-23	145
Heusinger & Weber (2017)	350[1]	-	-	-190	-70	-30	60

6 Conclusion & recommendations

The aims of this thesis were to develop the capabilities to predict the effect of vegetation on the urban microclimate. In particular the creation of an integrated modelling tool for urban planning and the extension of LES for urban applications; including radiation, wall fluxes, vegetation and heat storage. This chapter is organised as follows. Section 6.1 contains a summary of the work presented in this thesis. Section 6.2 provides some lessons learned and recommendations for modelling the urban environment and in section 6.3 ongoing and possible further work on the models is discussed. Finally, the thesis closes with the acknowledgments 6.4.

6.1 Contributions

Population growth and climate change forces cities to prepare for water scarcity and heat spells (IPCC, 2014), posing severe threats to future health and stability of cities. These problems are related to the urban heat island (UHI) effect, caused by difference of radiation, anthropogenic heating and material between rural and urban environments (Oke, 1982, Rosenzweig et al., 2015). Greening of façades and roofs can potentially mitigate the urban heat island effect (Getter & Rowe, 2006, Castleton et al., 2010, Santamouris, 2014). High resolution modelling tools to predict the effects of mitigation strategies are not commonly available as of yet, as a large number of scales and physical processes are involved in the formation of the urban microclimate. In this thesis my work on developing modelling tools to assess the impact of vegetation on the urban climate has been documented. Two models were modified to include many relevant processes of the urban environment. Below a summary of each chapter is presented and how the work relates to the objectives listed in section 1.7

Chapter 2 focused on evaluating the effect of evaporative cooling on outdoor air temperatures in an urban environment on a neighbourhood scale. For this purpose the urban energy balance model TEB (Masson, 2000) was extended to include an atmospheric surface layer and a green roof representation. The new model MTEB (Suter et al., 2017) can be used to quickly study a large variety of different urban structures, green roof surface covers and meteorological conditions. Specifically, it can be examined how the temperature reduction through green roofs relates to the evaporation rates and water availability. MTEB is well suited to be run as an integrated model and to assess the effect of vegetation on the local temperature on a neighbourhood scale.

Chapter 3 describes the large eddy simulation model DALES and how morphologic elements are handled. To study small scale urban features and local effects the UEB approach from chapter 2 is ill-suited. A defining aspect of the urban microclimate is that on small scales the turbulent nature of the atmosphere and the details of the urban structure and fabric are of great importance. Turbulence is a major contributor to fluxes of momentum, energy, moisture and other scalar quantities. Turbulence itself on the other hand is very heterogeneous and depends strongly on the local morphology and temperature distribution. For these reasons the established Dutch Atmospheric Large Eddy Simulation tool (Heus et al., 2010, Tomas et al., 2015) was adapted for urban applications (DALES-Urban). The governing equations and numerical discretisation follow the original DALES. To study the effect of green infrastructure the effect of heat and moisture exchange is of particular interest, and wall functions were introduced into DALES to model scalar and momentum exchanges at horizontal and vertical surfaces based on work by Uno et al. (1995), who consider different surface roughnesses for momentum and heat. A modified Jarvis-Stewart approach was used to model evapotranspiration from vegetated surfaces and the transport of water trough plants. This method can be combined seamlessly with the transfer coefficients from the standard wall function. Different building materials and surface roughnesses can be represented by changing the momentum and heat roughness lengths.

Chapter 4 documents the treatment of radiation, the calculation of ground heat flux and the surface energy balance. Urban surfaces experience a large spatial and temporal variability in surface temperatures and fluxes, especially in heterogeneous terrain. To better account for these effects in DALES-Urban, all surfaces are divided into several smaller facets based on the urban morphology. Facets represent all types of surfaces of the urban landscape, such as roofs, walls, roads and green roofs. The properties of every facet, needed for the wall function and energy balance calculation, are assigned individually according to the surface they represent. To calculate radiative exchange we followed the radiosity approach of Rao & Sastri (1996). Long- and shortwave radiative exchange processes between facets are based on view factors which can be calculated and stored prior to LES simulations. To account for the effect of the extending urban landscape outside the model domain a bounding wall was introduced. The incoming solar radiation is being evaluated for every facet depending on its orientation to the sun and the shadowing through other buildings. The effects of shadowing and blocked view between facets is considered by determining a percentage p_{b} the facets can see of each other. To calculate the temperature evolution of surfaces, every facet is divided into multiple layers. A model for ground heat flux where the temperature and temperature gradient are collocated was developed. The method is related to Hermitian interpolation (Peyret & Taylor, 2012, Van Reeuwijk, 2007). This method provides the surface temperature which is needed for the calculation of longwave radiation, allows the use wall functions and is simultaneously suited to close the surface energy budget. Thus, heat storage and thermal inertia, important aspects of the UHI, can be reliably represented in the DALES-Urban framework. Furthermore the information about ground heat flux allows to estimate the energy consumption for heating or cooling the building interiors and therefore estimates of the heat release through HVAC are also possible.

In Chapter 5 an application of the model was demonstrated through the investigation of a single green roof on the "Eastside" building during a hot summer day.

Prior to the simulation the pre-processing steps to obtain the urban morphology from LIDAR data and the creation of all the urban facets are shown. This test case clearly highlights the capabilities for future investigation of the urban microclimate with the newly developed model. DALES-Urban offers 3D velocity, temperature, humidity and passive scalar fields in a high temporal resolution. Furthermore for every facet the surface energy fluxes, the layer temperatures and layer temperatures gradients are available. All this information is relevant to investigate the UHI and the urban microclimate in detail.

6.2 Conclusions

The aim of this dissertations was to explore the impact of green infrastructure on the urban microclimate. The results of chapter 2, which was based on the MTEB model, revealed a linear relationship between air temperature and evaporation rates. This relation shows that green roofs have a limited capability to reduce the UHI, unless very large quantities of water are being evaporated. Indeed, water availability appears to be the limiting factor in general. For London, with a mean summer precipitation of about 1.5mm day^{-1}, we find an average temperature reduction of 0.4K if all the water above urban areas could be retained and evaporated. Green roofs further appear to be rather inefficient in reducing mean street level air temperatures directly. These findings agree with values from the literature. Green walls could not be studied but are being considered by a MSc student (Thorgeirsson, 2018). It can be expected that these are much more efficient in reducing street level temperatures as they are situated in the street canyons rather than on the roof.

DALES-Urban was used in chapter 5 to simulate the effect on the microclimate of a green roof on the “Eastside” building in the South Kensington area. The presence of a green roof leads to an air temperature reduction of $\approx$ 0.5K in the direct vicinity of the roof. Downstream the effect is quickly diluted and road level temperatures in the recirculation area of the building are lowered by $\approx$ 0.1K. Specific humidity is elevated by a marginal amount ($\approx$ 0.05g kg^{-1}) in the recirculation area due to evapotranspiration from the vegetation. These results corroborate that the effect of a small green roof area on the local microclimate is rather limited, both in terms of magnitude and in its area of influence.

This dissertation clearly demonstrates that a one-size-fits all model does not exist. Depending on the intended use of a model, different modelling strategies will be required. Urban planners need models that provide nearly real-time feedback which makes models like MTEB very attractive, as it is able to provide reasonably accurate predictions within a very short time. LES is on the other side of the spectrum. It is computationally expensive, but provides unprecedented spatial and temporal detail to the predictions. A simulation technique which sits between these two extremes is RANS, which models the turbulence entirely and considers average flow fields only. Hence, RANS is much less computationally expensive and often used to study flow around buildings (Blocken, 2018). However, for transient and unsteady problems LES is better suited, including problems like personal exposure (Nielsen, 2015). Overall the performance of LES should be superior to RANS simulations, producing more accurate and reliable results. However, there is as of yet a lack of best practice guidelines for obstacle resolving LES, concerning sub-grid models, in/out-flow conditions, grid resolution etc. (Blocken & Gualtieri, 2012, Blocken, 2018, Gousseau et al., 2013).

It is crucial that detailed field data is collected that can be used to validate LES studies. The "Eastside" building was fully instrumented, but the main focus was on the green roof itself. As a consequence, only basic local meteorological information is available which can be expected to make it hard to constrain the data. This is particularly true since DALES-Urban is spatially and temporally resolved. Indeed, appropriate selection of the boundary conditions is crucial as these can strongly affect the local microclimate. Point measurements are insufficient to constrain the data, and measurements techniques like LIDAR are extremely helpful for validation purposes. The measurements should be augmented by detailed radiation measurements to determine surface fluxes and temperatures. Imaging techniques like infrared imaging could be of use.

6.3 Future work

Considerable effort was invested in making sure that all the model parts of DALES work as intended and are combined in a functioning model. Nevertheless, no full validation of the entire model against measurements and observations has been done to date. A green roof is installed and instrumented on the "Eastside" building, offering an ideal validation case. The extent of such a task was unfortunately not achievable within the time-constraints of a single PhD. It is thus important that a careful validation is carried out. Furthermore, it would be extremely valuable to test the sensitivity of the model to various input parameters such as building materials, roughness lengths or the dependence of the building shapes on the grid size.

The capabilities developed in this dissertation allow for systematic investigation of a large variety of interesting urban phenomena: 1) the effect of the installation of green roofs and green walls on the local microclimate; 2) the urban microclimate in general, the effect of shading, albedo changes, turbulent structures in the urban boundary layer and suburban-urban transition; 3) the effects of thermal inertia on temperatures and the urban heat island effect.

Although not the focus of this work, the model can also be used to investigate urban dispersion of active and passive substances (Grylls et al., 2019). The current development was realised with studying hot and dry summer conditions in mind. Therefore, many important processes for other climatic and weather conditions are not considered. There are many opportunities to extend the model, some of which are currently pursued in my group at Imperial College. The introduction of tall vegetation such as trees is very interesting since trees are often discussed as possible remedies against exceedingly hot temperatures. In LES trees are a challenge, since they not only affect the radiative transfer, act as heat, moisture and momentum sources/sinks, but also affect the local turbulence. Another extension might be the inclusion of open water surfaces such as ponds, lakes and rivers. Such surfaces can be included in the current framework of urban facets and solely introducing a wall function describing the exchange processes might suffice.

Another extremely interesting aspect of urban climate is air conditioning. Especially during hot summer days heat exhaust from AC units could potentially contribute significantly to local peak outdoor temperatures. With the current wall model energy demand of ACs could for example be estimated depending on the wall heat flux. Some of the potential extensions of DALES are shown in Fig. 6.1. Some of these extensions might improve existing features, such as adding a model for soil moisture might more accurately predict the long-term behaviour of vegetated surfaces, especially under conditions where water is less readily available. If building

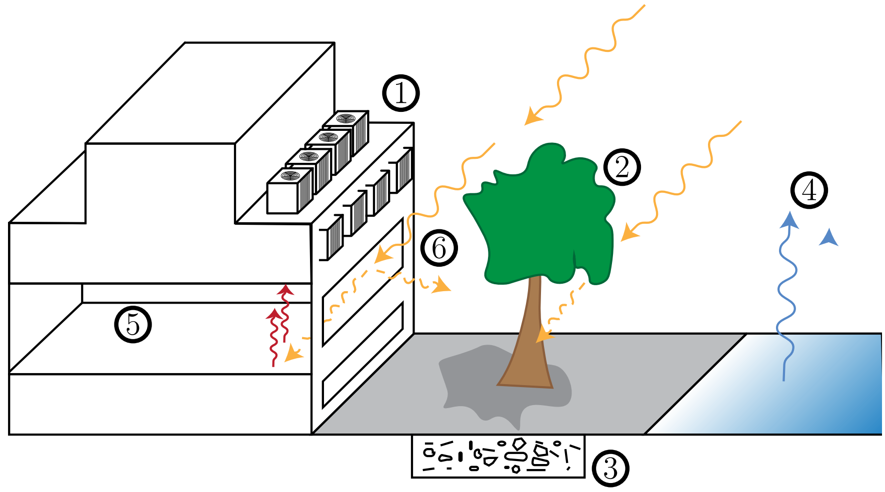

Figure 6.1: Processes that are potentially desirable to be implemented into DALES in the future: 1) Heating, ventilation and air conditioning (HVAC), 2) tall vegetation and trees, 3) model for soil moisture, 4) open water surfaces, 5) indoor climate and building energy balance, 6) radiation transmission and specular reflections.

energy balances are to be studied the inclusion of windows as semi-transparent surfaces is to be considered. MTEB also still offers many interesting future applications. Although other UEB models might already include more details of the urban environment, the relative simplicity of MTEB can be of great use when trying to understand the interplay of processes. It is also extremely helpful to have a fast model at hand to obtain estimates used for urban planning. Such estimates can further be compared to simulation results from DALES. Some future extensions to MTEB could include the implementation of HVAC, green walls or tall vegetation. It has to be concluded that studying the urban climate remains challenging and fascinating in the future. With computational advances offering the power to model ever more processes in greater detail. Urbanisation and climate change will continue to urge us to better understand the climate of cities. I am personally looking forward to future modelling and field research in this area and hope that my work contributes to its progress.

6.4 Acknowledgements

Developing a model to study the urban climate was, in order, interesting, demanding and frustrating. This thesis is extremely multidisciplinary and it was enthralling to learn so much in the processes. Within the Blue-Green dream alone we shared expertise in atmospheric science, fluid dynamics, architecture, hydrology and civil engineering. Add all the acquaintances during conferences, seminars and within the university. Requiring such a broad palette of skills also has its downsides. On a project basis, with multiple PhD students and supervisors, efficient collaboration is difficult and opportunities might have been missed. As an individual it easy to lose track of ongoing research in all the fields. For some physical phenomena science lacks the understanding and alternatives have to be found. However, development of DALES-Urban goes on and the prospect remains that the work done during my PhD is an important step and that it is in the nature of science that nothing is ever final.

I would like to thank my primary supervisor Maarten van Reeuwijk for the many helpful discussions and support during this project, allowing me to grow as a researcher. His tireless curiosity in environmental processes and how to model them has been an inspiration. In addition, I would like to thank Prof. Čedo Maksimović for his vision of bluer, greener cities in the future and the research opportunities this creates. I extend my thanks thank Matteo Malacarne for working on an early prototype of MTEB as part of his final year MEng project and I sincerely appreciate the valuable input of Ana Mijic and our discussions with her. Further I much appreciated the opportunity to study and work at TU Delft for one month offered by Prof. Harm Jonker. A special thanks goes to Liliane Auwerter for helping me create some of the drawings in this dissertation. Finally, I would like to thank all my friends and family for their love and support. The research for this work was supported by the European Institute of Technology, Climate KIC Innovation project Blue-Green Dream.

References

Ambirajan, A., & Venkateshan, S. P. (1993). Accurate determination of diffuse view factors between planar surfaces. *Int. J. Heat Mass Transf.*, *36*(8), 2203–2208. DOI `https://doi.org/10.1016/S0017-9310(05)80151-6`.

Aoyagi, T., & Takahashi, S. (2012). Development of an Urban Multilayer Radiation Scheme and Its Application to the Urban Surface Warming Potential. *Boundary-Layer Meteorol.*, *142*(2), 305–328. DOI `https://doi.org/10.1007/s10546-011-9679-0`.

Arakawa, A., & Lamb, V. R. (1977). Computational design of the basic dynamical processes of the UCLA general circulation model. In J. Chang (Ed.) *Methods Comput. Phys.*, vol. 17, (pp. 173–265). New York, NY, USA: Academic Press.

Arnfield, A. J. (2003). Two decades of urban climate research: A review of turbulence, exchanges of energy and water, and the urban heat island. *Int. J. Climatol.*, *23*(1), 1–26. DOI `https://doi.org/10.1002/joc.859`.

Asadi, I., Shafigh, P., Hassan, Z. F. B. A., & Mahyuddin, N. B. (2018). Thermal conductivity of concrete – a review. *Journal of Building Engineering*, *20*, 81 – 93. DOI `https://doi.org/10.1016/j.jobe.2018.07.002`.

Barker, E. H., & Baxter, T. L. (1975). A Note on the Computation of Atmospheric Surface Layer Fluxes for Use in Numerical Modeling. *J. Appl. Meteorol.*, *14*, 620–622. DOI `https://doi.org/10.1175/1520-0450(1975)014<0620:ANOTCO>2.0.CO;2`.

Barlow, J. F. (2014). Progress in observing and modelling the urban boundary layer. *Urban Clim.*, *10*, 216–240. DOI https://doi.org/10.1016/j.uclim.2014.03.011.

Best, M. J., Pryor, M., Clark, D. B., & Rooney, G. G. (2011). The Joint UK Land Environment Simulator (JULES), model description - Part 1: Energy and water fluxes. *Geosci. Model Dev.*, *4*, 677–699. DOI https://doi.org/10.5194/gmd-4-677-2011.

Blocken, B. (2018). Les over rans in building simulation for outdoor and indoor applications: A foregone conclusion? *Building Simulation*, *11*(5), 821–870. DOI https://doi.org/10.1007/s12273-018-0459-3.

Blocken, B., & Gualtieri, C. (2012). Ten iterative steps for model development and evaluation applied to computational fluid dynamics for environmental fluid mechanics. *Environmental Modelling and Software*, *33*, 1–22. DOI https://doi.org/10.1016/j.envsoft.2012.02.001.

Blue Green Dream (2018). Web presence of Blue Green Dream. URL http://bgd.org.uk accessed: 2018-03-27.

Bolton, D. (1980). The computation of equivalent potential temperature. *Mon. Weather Rev.*, *108*(7), 1046–1053. DOI https://doi.org/10.1175/1520-0493(1980)108%3C1046:TCOEPT%3E2.0.CO;2.

Bozovic, R., Maksimovic, C., Mijic, A., Smith, K., Suter, I., & van Reeuwijk, M. (2017). Blue Green Solutions. Tech. rep., Climate-KIC.

Businger, J. A., Wyngaard, J. C., Izumi, Y., & Bradley, E. F. (1971). Flux-Profile Relationships in the Atmospheric Surface Layer. *J. Atmos. Sci.*, *28*(2), 181–189. DOI https://doi.org/10.1175/1520-0469(1971)028<0181:FPRITA>2.0.CO;2.

Cai, X.-M. (2012a). Effects of differential wall heating in street canyons on dispersion and ventilation characteristics of a passive scalar. *Atmos. Environ.*, *51*, 268–277. DOI https://doi.org/10.1016/j.atmosenv.2012.01.010.

Cai, X.-M. (2012b). Effects of Wall Heating on Flow Characteristics in a Street Canyon. *Boundary-Layer Meteorol.*, *142*(3), 443–467. DOI https://doi.org/10.1007/s10546-011-9681-6.

Castleton, H. F., Stovin, V., Beck, S. B. M., & Davison, J. B. (2010). Green roofs; building energy savings and the potential for retrofit. *Energy Build.*, *42*(10), 1582–1591. DOI https://doi.org/doi.org/10.1016/j.enbuild.2010.05.004.

Cirkel, D. G., Voortman, B. R., Van Veen, T., & Bartholomeus, R. P. (2018). Evaporation from (blue-)green roofs: Assessing the benefits of a storage and capillary irrigation system based on measurements and modeling. *Water*, *10*(9). DOI https://doi.org/10.3390/w10091253.

Clark, D. B., Mercado, L. M., Sitch, S., Jones, C. D., Gedney, N., Best, M. J., Pryor, M., Rooney, G. G., Essery, R. L. H., Blyth, E., Boucher, O., Harding, R. J., Cox, P. M., Huntingford, C., & Cox, P. M. (2011). The Joint UK Land Environment Simulator (JULES), model description - Part 2: Carbon fluxes and vegetation dynamics. *Geosci. Model Dev.*, *4*(3), 701–722. DOI https://doi.org/10.5194/gmdd-4-641-2011.

Climate-KIC (2018). Web presence of Climate-KIC.
URL http://www.climate-kic.org accessed: 2018-03-27.

Courant, R., Friedrichs, K., & Lewy, H. (1928). Über die partiellen Differenzengleichungen der mathematischen Physik. *Math. Ann.*, *100*(1), 32–74. DOI https://doi.org/10.1007/BF01448839.

Craft, T. J., Gant, S. E., Gerasimov, A. V., Iacovides, H., & Launder, B. E. (2006). Development and application of wall-function treatments for turbulent forced and mixed convection flows. *Fluid Dyn. Res.*, *38*(2-3), 127. DOI https://doi.org/10.1016/j.fluiddyn.2004.11.002.

Cuijpers, J. W. M., & Duynkerke, P. G. (1993). Large Eddy Simulation of Trade Wind Cumulus Clouds. *J. Atmos. Sci.*, *50*(23), 3894–3908. DOI https://doi.org/10.1175/1520-0469(1993)050<3894:LESOTW>2.0.CO;2.

ECMWF (2013). IFS documentation - part III: Dynamics and numerical procedures. Tech. Rep. Cy40r1, European Centre for Medium-Range Weather Forecasts (ECMWF).

EDINA (2018). Digimap: Maps & geospatial data for UK academia.
URL https://edina.ac.uk accessed: 2018-02-01.

Ehrhard, J., Khatib, I. A., Winkler, C., Kunz, R., Moussiopoulos, N., & Ernst, G. (2000). The microscale model MIMO: development and assessment. *J. Wind Eng. Ind. Aerodyn.*, *85*(2), 163–176. DOI `https://doi.org/10.1016/S0167-6105(99)00137-3`.

Emanuel, K. A. (1994). *Atmospheric convection*. Oxford University Press on Demand.

Erdélyi, R., Wang, Y., Guo, W., Hanna, E., & Colantuono, G. (2014). Three-dimensional SOlar RAdiation Model (SORAM) and its application to 3-D urban planning. *Sol. Energy*, *101*, 63–73. DOI `https://doi.org/10.1016/j.solener.2013.12.023`.

Erell, E., Pearlmutter, D., & Williamson, T. (2011). *Urban microclimate - Designing the spaces between buildings*. Routledge, 1st ed.

European Commission (2012). The multifunctionality of Green Infrastructure. Tech. rep., European Commission - Environment.

Fadlun, E. A., Verzicco, R., Orlandi, P., & Mohd-Yusof, J. (2000). Combined immersed-boundary finite-difference methods for three-dimensional complex flow simulations. *J. Comput. Phys.*, *161*, 35–60. DOI `https://doi.org/10.1006/jcph.2000.6484`.

Feng, C., Meng, Q., & Zhang, Y. (2010). Theoretical and experimental analysis of the energy balance of extensive green roofs. *Energy and Buildings*, *42*(6), 959 – 965. DOI `https://doi.org/10.1016/j.enbuild.2009.12.014`.

Garratt, J. R. (1994). The atmospheric boundary layer. *Earth-Science Rev.*, *37*(1-2), 89–134.

Georgescu, M., Morefield, P. E., Bierwagen, B. G., & Weaver, C. P. (2014). Urban adaptation can roll back warming of emerging megapolitan regions. *Proc. Natl. Acad. Sci.*, *111*(8), 2909–2914. DOI `https://doi.org/10.1073/pnas.1322280111`.

Getter, K. L., & Rowe, D. B. (2006). The Role of Extensive Green Roofs in Sustainable Development. *HortScience*, *41*(5), 1276–1285.

Ghannam, K., Poggi, D., Porporato, A., & Katul, G. G. (2015). The Spatio-temporal Statistical Structure and Ergodic Behaviour of Scalar Turbulence Within a Rod Canopy. *Boundary-Layer Meteorol.*, *157*(3), 447–460. DOI https://doi.org/10.1007/s10546-015-0073-1.

Girard, P., Nadeau, D. F., Pardyjak, E. R., Overby, M., Willemsen, P., Stoll, R., Bailey, B. N., & Parlange, M. B. (2017). Evaluation of the QUIC-URB wind solver and QESRadiant radiation-transfer model using a dense array of urban meteorological observations. *Urban Clim.*, *24*, 657 – 674. DOI https://doi.org/10.1016/j.uclim.2017.08.006.

Google Maps (2018). Map of South Kensington, London, UK.
URL https://www.google.com/maps/@51.4987867,-0.1772725,890m/data=!3m1!1e3 accessed: 2018-06-29.

Gousseau, P., Blocken, B., & van Heijst, G. (2013). Quality assessment of large-eddy simulation of wind flow around a high-rise building: Validation and solution verification. *Computers & Fluids*, *79*, 120 – 133. DOI https://doi.org/10.1016/j.compfluid.2013.03.006.

Grimmond, C. S. B., Blackett, M., Best, M. J., Barlow, J., Baik, J. J., Belcher, S. E., & Bohnenstengel, S. I. (2010). The International Urban Energy Balance Models Comparison Project: First Results from Phase 1. *J. Appl. Meteor. Clim.*, (pp. 1268–1292). DOI https://doi.org/10.1175/2010JAMC2354.1.

Grimmond, S. (2007). Urbanization and global environmental change: local effects of urban warming. *Geogr. J.*, *173*(1), 83–88. DOI https://doi.org/10.1111/j.1475-4959.2007.232_3.x.

Gromke, C., Blocken, B., Janssen, W., Merema, B., van Hooff, T., & Timmermans, H. (2015). CFD analysis of transpirational cooling by vegetation: Case study for specific meteorological conditions during a heat wave in Arnhem, Netherlands. *Build. Environ.*, *83*, 11–26. DOI https://doi.org/10.1016/j.buildenv.2014.04.022.

Grylls, T., Le Cornec, C. M. A., Salizzoni, P., Soulhac, L., Stettler, M., & van Reeuwijk, M. (2019). Evaluation of an operational air quality model using large-eddy simulation. *Manuscript in preparation.*

Hall, D. O., & Rao, K. K. (1999). *Photosynthesis*. Studies in biology. Cambridge: Cambridge University Press, 6th ed.

Harman, I. N., Best, M. J., & Belcher, S. E. (2004). Radiative exchange in an urban street canyon. *Boundary-Layer Meteorology*, *110*(2), 301–316. DOI `https://doi.org/10.1023/A:1026029822517`.

Heus, T., van Heerwaarden, C. C., Jonker, H. J. J., Siebesma, A. P., Axelsen, S., van den Dries, K., Geoffroy, O., Moene, A. F., Pino, D., de Roode, S. R., & Vila-Guerau de Arellano, J. (2010). Formulation of the Dutch Atmospheric Large-Eddy Simulation (DALES) and overview of its applications. *Geosci. Model Dev.*, *3*, 415–444. DOI `https://doi.org/10.5194/gmd-3-415-2010`.

Heusinger, J., & Weber, S. (2017). Surface energy balance of an extensive green roof as quantified by full year eddy-covariance measurements. *Science of The Total Environment*, *577*, 220 – 230. DOI `https://doi.org/10.1016/j.scitotenv.2016.10.168`.

Hölling, M., & Herwig, H. (2005). Asymptotic analysis of the near-wall region of turbulent natural convection flows. *J. Fluid Mech.*, *541*, 383–397. DOI `https://doi.org/10.1017/S0022112005006300`.

Holtslag, A. A. M., & De Bruin, H. A. R. (1988). Applied modeling of the nighttime surface energy balance over land. *J. Appl. Meteorol.*, *27*(6), 689–704. DOI `https://doi.org/10.1175/1520-0450(1988)027%3C0689:AMOTNS%3E2.0.CO;2`.

Hottel, H. C., & Sarofim, A. F. (1967). *Radiative transfer*. McGraw-Hill.

Howell, J. R. (2018). View factor calculator.
URL `http://www.thermalradiation.net/` accessed: 2018-06-30.

Howell, J. R., Menguc, M. P., & Siegel, R. (2010). *Thermal radiation heat transfer*. CRC press.

Huttner, S. (2012). *Further development and application of the 3D microclimate simulation ENVI-met*. Ph.D. thesis, Johannes Gutenberg-Universität Mainz.

IPCC (2014). Climate Change 2014: Impacts, Adaptation, and Vulnerability. Part B: Regional Aspects. Contribution of Working Group II to the Fifth Assessment

Report of the Intergovernmental Panel on Climate Change. Tech. rep., Intergovernmental Panel on Climate Change.

Järvi, L., Grimmond, C. S. B., & Christen, A. (2011). The surface urban energy and water balance scheme (SUEWS): Evaluation in Los Angeles and Vancouver. *J. Hydrol.*, *411*(3), 219–237. DOI `https://doi.org/10.1016/j.jhydrol.2011.10.001`.

Jarvis, P. G. (1976). The Interpretation of the Variations in Leaf Water Potential and Stomatal Conductance Found in Canopies in the Field. *Philos. Trans. R. Soc. London B Biol. Sci.*, *273*(927), 593–610. DOI `https://doi.org/10.1098/rstb.1976.0035`.

Jenkins, Thomas and Bolivar-Mendoza, Gabriel (2018). Solar Time, Angles, and Irradiance Calculator: User Manual.
URL `https://aces.nmsu.edu/pubs/_circulars/CR674.pdf` accessed: `2018-11-27`.

Kovar-Panskus, a., Moulinneuf, L., Savory, E., Abdelqari, A., Sini, J. F., Rosant, J. M., Robins, A., & Toy, N. (2002). A wind tunnel investigation of the influence of solar-induced wall-heating on the flow regime within a simulated urban street canyon. *Water, Air, Soil Pollut. Focus*, *2*(5-6), 555–571. DOI `https://doi.org/10.1023/A:1021345131117`.

Kovats, R. S., & Hajat, S. (2008). Heat Stress and Public Health: A Critical Review. *Annu. Rev. Public Heal.*, *29*(1), 41–55. DOI `https://doi.org/10.1146/annurev.publhealth.29.020907.090843`.

Krayenhoff, E. S., Christen, A., Martilli, A., & Oke, T. R. (2014). A Multi-layer Radiation Model for Urban Neighbourhoods with Trees. *Boundary-Layer Meteorol.*, *151*(1), 139–178. DOI `https://doi.org/10.1007/s10546-013-9883-1`.

Krayenhoff, E. S., & Voogt, J. (2007). A microscale three-dimensional urban energy balance model for studying surface temperatures. *Boundary-Layer Meteorol.*, *123*, 433–461. DOI `https://doi.org/10.1007/s10546-006-9153-6`.

Li, D., Bou-Zeid, E., & Oppenheimer, M. (2014). The effectiveness of cool and green roofs as urban heat island mitigation strategies. *Environ. Res. Lett.*, *9*(5). DOI `https://doi.org/10.1088/1748-9326/9/5/055002`.

Lindberg, F., Holmer, B., & Thorsson, S. (2008). SOLWEIG 1.0–Modelling spatial variations of 3D radiant fluxes and mean radiant temperature in complex urban settings. *Int. J. Biometeorol.*, *52*(7), 697–713. DOI `https://doi.org/10.1007/s00484-008-0162-7`.

Louis, J. F. (1979). A parametric model of vertical eddy fluxes in the atmosphere. *Boundary-Layer Meteorol.*, *17*(2), 187–202. DOI `https://doi.org/10.1007/BF00117978`.

Lowan, A. N., Davids, N., & Levenson, A. (1942). Table of the zeros of the Legendre polynomials of order 1-16 and the weight coefficients for Gauss' mechanical quadrature formula. *Bull. Am. Math. Soc.*, *48*(10), 739–743. DOI `https://doi.org/10.1090/S0002-9904-1942-07771-8`.

Luber, G., & McGeehin, M. (2008). Climate Change and Extreme Heat Events. *Am. J. Prev. Med.*, *35*(5), 429–435. DOI `https://doi.org/10.1016/j.amepre.2008.08.021`.

Mackey, C. W., Lee, X., & Smith, R. B. (2012). Remotely sensing the cooling effects of city scale efforts to reduce urban heat island. *Build. Environ.*, *49*, 348–358. DOI `https://doi.org/10.1016/j.buildenv.2011.08.004`.

Maronga, B., Gryschka, M., Heinze, R., Hoffmann, F., Kanani-Sühring, F., Keck, M., Ketelsen, K., Letzel, M. O., Sühring, M., & Raasch, S. (2015). The Parallelized Large-Eddy Simulation Model (PALM) version 4.0 for atmospheric and oceanic flows: model formulation, recent developments, and future perspectives. *Geosci. Model Dev. Discuss.*, *8*(2), 1539–1637. DOI `https://doi.org/10.5194/gmd-8-2515-2015`.

Masson, V. (2000). A physically-based scheme for the urban energy budget in atmospheric models. *Boundary-Layer Meteorol.*, *94*, 357–397. DOI `https://doi.org/10.1023/A:1002463829265`.

Masson, V., Gomes, L., Pigeon, G., Liousse, C., Pont, V., Lagouarde, J.-P., Voogt, J., Salmond, J., Oke, T. R., Hidalgo, J., Legain, D., Garrouste, O., Lac, C., Connan, O., Briottet, X., Lachérade, S., & Tulet, P. (2008). The Canopy and Aerosol Particles Interactions in TOulouse Urban Layer (CAPITOUL) experiment. *Meteorol. Atmos. Phys.*, *102*(3-4), 135–157. DOI https://doi.org/10.1007/s00703-008-0289-4.

Matzarakis, A., Rutz, F., & Mayer, H. (2010). Modelling radiation fluxes in simple and complex environments: basics of the RayMan model. *Int. J. Biometeorol.*, *54*(2), 131–139. DOI https://doi.org/10.1007/s00484-006-0061-8.

McDermott, R., Vanella, M., & Henderson, B. (2017). A temperature wall function for large-eddy simulation of natural convection based on modified Rayleigh number scaling. In *APS Meet. Abstr.*, (p. D35.002).

Mirzaei, P. A. (2015). Recent challenges in modeling of urban heat island. *Sustain. cities Soc.*, *19*, 200–206. DOI https://doi.org/10.1016/j.scs.2015.04.001.

Mirzaei, P. A., & Haghighat, F. (2010). Approaches to study urban heat island - abilities and limitations. *Build. Environ.*, *45*(10), 2192–2201.

Mittal, R., & Iaccarino, G. (2005). Immersed Boundary Methods. *Annu. Rev. Fluid Mech.*, *37*(1), 239–261. DOI https://doi.org/10.1146/annurev.fluid.37.061903.175743.

Moene, A. F., & van Dam, J. C. (2014). *Transport in the atmosphere-vegetation-soil continuum*. Cambridge University Press.

Mohd-Yusof, J. (1997). Combined Immersed-Boundary/B-spline methods for simulations of flow in complex geometries. Tech. rep., Center for Turbulence Research, NASA Ames/Stanford Univ.

Monin, A. S., & Obukhov, A. M. (1954). Basic laws of turbulent mixing in the surface layer of the atmosphere. *Contrib. Geophys. Inst. Acad. Sci. USSR*, *24*(151), 163–187.

Moonen, P., Defraeye, T., Dorer, V., Blocken, B., & Carmeliet, J. (2012). Urban Physics: Effect of the micro-climate on comfort, health and energy demand. *Front. Archit. Res.*, *1*(3), 197–228. DOI https://doi.org/10.1016/j.foar.2012.05.002.

Murphy, D. M., & Koop, T. (2005). Review of the vapour pressures of ice and supercooled water for atmospheric applications. *Q. J. R. Meteorol. Soc.*, *131*(608), 1539–1565. DOI `https://doi.org/10.1256/qj.04.94`.

Musy, M., Malys, L., Morille, B., & Inard, C. (2015). The use of SOLENE-microclimat model to assess adaptation strategies at the district scale. *Urban Clim.*, *14*, 213–223. DOI `https://doi.org/10.1016/j.uclim.2015.07.004`.

Nickolay Lamm (2018). Blog on storagefront.com.
URL `https://www.storagefront.com/therentersbent/why-are-cities-hotter-than-surrounding-areas/` accessed: 2018-05-15.

Nielsen, P. V. (2015). Fifty years of cfd for room air distribution. *Building and Environment*, *91*, 78–90. DOI `https://doi.org/10.1016/j.buildenv.2015.02.035`.

Nieuwstadt, F. T. M., & Brost, R. A. (1986). The Decay of Convective Turbulence. *J. Atmos. Sci.*, *43*(6), 532–546. DOI https://doi.org/10.1175/1520-0469(1986)043<0532:TDOCT>2.0.CO;2.

NOAA (2018). Solar Position Calculator.
URL `https://www.esrl.noaa.gov/gmd/grad/solcalc/azel.html` accessed: 2018-04-06.

Noilhan, J., & Planton, S. (1989). A Simple Parameterization of Land Surface Processes for Meteorological Models. *Mon. Wea. Rev.*, *117*(3), 536–549. DOI https://doi.org/10.1175/1520-0493(1989)117<0536:ASPOLS>2.0.CO;2.

Oberndorfer, E., Lundholm, J., Bass, B., Coffman, R. R., Doshi, H., Dunnett, N., Gaffin, S., Köhler, M., Liu, K. K. Y., & Rowe, B. (2007). Green Roofs as Urban Ecosystems: Ecological Structures, Functions, and Services. *Bioscience*, *57*(10), 823–833. DOI `https://doi.org/10.1641/B571005`.

Obukhov, A. M. (1946). Turbulence in an atmosphere with inhomogeneous temperature, Tr. *Inst. Teor. Geofis. Akad. Nauk. SSSR*, *1*, 95–115.

Oke, T. R. (1981). Canyon geometry and the nocturnal urban heat island: Comparison of scale model and field observations. *Journal of Climatology*, *1*(3), 237–254. DOI `https://doi.org/10.1002/joc.3370010304`.

Oke, T. R. (1982). The energetic basis of the urban heat island. *Q. J. R. Meteorol. Soc.*, *108*(455), 1–24. DOI `https://doi.org/10.1002/qj.49710845502`.

Oke, T. R. (1988). Street design and urban canopy layer climate. *Energy Build.*, *11*, 103–113. DOI `https://doi.org/10.1016/0378-7788(88)90026-6`.

Oke, T. R., Mills, G., Christen, A., & Voogt, J. A. (2017). *Urban Climates*. Cambridge University Press.

Ouwersloot, H. (2017). DALES GIT repository.
URL `https://github.com/dalesteam/dales` accessed: 2018-04-15.

Panofsky, A. (1963). Determination of stress from wind and temperature measurements. *Q. J. R. Meteorol. Soc.*, *89*(379), 85–94. DOI `https://doi.org/10.1002/qj.49708937906`.

Parente, A., Gorlé, C., van Beeck, J., & Benocci, C. (2011). A comprehensive modelling approach for the neutral atmospheric boundary layer: consistent inflow conditions, wall function and turbulence model. *Boundary-Layer Meteorol.*, *140*(3), 411.

Paulson, C. A. (1970). The Mathematical Representation of Wind Speed and Temperature Profiles in the Unstable Atmospheric Surface Layer. *J. Appl. Meteorol.*, *9*(6), 857–861. DOI `https://doi.org/10.1175/1520-0450(1970)009<0857:TMROWS>2.0.CO;2`.

Peskin, C. S. (1972). Flow patterns around heart valves: A numerical method. *J. Comput. Phys.*, *10*(2), 252–271. DOI `https://doi.org/10.1016/0021-9991(72)90065-4`.

Petty, G. W. (2006). *A First Course in Atmospheric Radiation*. Sundog Pub.

Peyret, R., & Taylor, T. D. (2012). *Computational methods for fluid flow*. Springer Science & Business Media.

Pourquie, M., Breugem, W. P., & Boersma, B. J. (2009). Some Issues Related to the Use of Immersed Boundary Methods to Represent Square Obstacles. *Int. J. Multiscale Comput. Eng.*, *7*(6), 509–522. DOI `https://doi.org/10.1615/IntJMultCompEng.v7.i6.30`.

Rao, V. R., & Sastri, V. M. K. (1996). Efficient evaluation of diffuse view factors for radiation. *Int. J. Heat Mass Transf.*, *39*(6), 1281–1286. DOI `https://doi.org/10.1016/0017-9310(95)00203-0`.

Resler, J., Krč, P., Belda, M., Juruš, P., Benešová, N., Lopata, J., Vlček, O., Damašková, D., Eben, K., Derbek, P., Maronga, B., & Kanani-Sühring, F. (2017). PALM-USM v1.0: A new urban surface model integrated into the PALM large-eddy simulation model. *Geosci. Model Dev.*, *10*(10), 3635–3659. DOI `https://doi.org/10.5194/gmd-10-3635-2017`.

Richards, K., Schatzmann, M., & Leitl, B. (2006). Wind tunnel experiments modelling the thermal effects within the vicinity of a single block building with leeward wall heating. *J. Wind Eng. Ind. Aerodyn.*, *94*(8), 621–636. DOI `https://doi.org/10.1016/j.jweia.2006.02.003`.

Rizwan, A. M., Dennis, L. Y. C., & Liu, C. (2008). A review on the generation, determination and mitigation of Urban Heat Island. *J. Environ. Sci.*, *20*(1), 120–128. DOI `https://doi.org/10.1016/S1001-0742(08)60019-4`.

Rosenzweig, C., Solecki, W., Romero-Lankao, P., Mehrotra, S., Dhakal, S., Bowman, T., & Ibrahim, S. A. (2015). Summary for City Leaders - Second UCCRN Assessment Report on Climate Change and Cities (ARC3.2). Tech. rep., Urban Climate Change Research Network (UCCRN).

Sagaut, P. (2000). *Large Eddy Simulation for Incompressible Flows*. Springer-Verlag Berlin Heidelberg.

Santamouris, M. (2014). Cooling the cities - A review of reflective and green roof mitigation technologies to fight heat island and improve comfort in urban environments. *Sol. Energy*, *103*, 682–703. DOI `https://doi.org/10.1016/j.solener.2012.07.003`.

Schlünzen, K. H., Hinneburg, D., Knoth, O., Lambrecht, M., Leitl, B., Lopez, S., Lüpkes, C., Panskus, H., Renner, E., & Schatzmann, M. (2003). Flow and transport in the obstacle layer: First results of the micro-scale model MITRAS. *J. Atmos. Chem.*, *44*(2), 113–130.

Sievers, U. (2016). *Das kleinskalige Strömungsmodell MUKLIMO_3. Teil 2: Thermodynamische Erweiterungen*. Deutscher Wetterdienst.

Smagorinsky, J. (1963). General circulation experiments with the primitive equations. *Mon. Wea. Rev.*, *91*(3), 99–164. DOI https://doi.org/10.1175/1520-0493(1963)091%3C0099:GCEWTP%3E2.3.CO;2.

Sparrow, E. M. (1961). Radiation heat transfer. Tech. rep., NASA.

Sparrow, E. M. (1963). On the calculation of radiant interchange between surfaces. *Mod. Dev. Heat Transf. New York*. DOI https://doi.org/10.1115/1.3683676.

Sparrow, E. M., & Cess, R. D. (1978). *Radiation heat transfer. Series in thermal and fluids engineering*. New York: McGraw-Hill, 5th ed.

Stewart, J. B. (1988). Modelling surface conductance of pine forest. *Agric. For. Meteorol.*, *43*(1), 19–35. DOI https://doi.org/10.1016/0168-1923(88)90003-2.

Sun, T., Grimmond, C. S. B., & Ni, G.-H. (2016). How do green roofs mitigate urban thermal stress under heat waves? *J. Geophys. Res. Atmos.*, *121*(10), 5320–5335. DOI https://doi.org/10.1002/2016JD024873.

Suter, I., Maksimović, Č., & van Reeuwijk, M. (2017). A neighbourhood-scale estimate for the cooling potential of green roofs. *Urban Clim.*, *20*, 33–45. DOI https://doi.org/10.1016/j.uclim.2017.02.007.

Svensson, M. K. (2004). Sky view factor analysis – implications for urban air temperature differences. *Meteorological Applications*, *11*(3), 201–211. DOI https://doi.org/10.1017/S1350482704001288.

Swinbank, W. C. (1963). Long-wave radiation from clear skies. *Q. J. R. Meteorol. Soc.*, *89*(381), 339–348. DOI https://doi.org/10.1002/qj.49708938105.

The Engineering Toolbox (2018). The Engineering Toolbox, Material Properties. URL https://www.engineeringtoolbox.com/material-properties-t_24.html accessed: 2018-05-15.

Thorgeirsson, H. (2018). Can green facades improve the urban microclimate in cities? Tech. rep.

Threlkeld, J. L. (1970). *Thermal environmental engineering*. Prentice Hall.

Tomas, J. M., Pourquie, M., & Jonker, H. J. J. (2015). The influence of an obstacle on flow and pollutant dispersion in neutral and stable boundary layers. *Atmos. Environ.*, *113*, 236–246. DOI `https://doi.org/10.1016/j.atmosenv.2015.05.016`.

Tomas, J. M., Pourquie, M. J. B. M., & Jonker, H. J. J. (2016). Stable Stratification Effects on Flow and Pollutant Dispersion in Boundary Layers Entering a Generic Urban Environment. *Boundary-Layer Meteorol.*, *159*(2), 221–239. DOI `https://doi.org/10.1007/s10546-015-0124-7`.

Tzoulas, K., Korpela, K., Venn, S., Yli-Pelkonen, V., Kaźmierczak, A., Niemela, J., & James, P. (2007). Promoting ecosystem and human health in urban areas using Green Infrastructure: A literature review. *Landsc. Urban Plan.*, *81*(3), 167–178. DOI `https://doi.org/10.1016/j.landurbplan.2007.02.001`.

UK Environment Agency (2018). Lidar composite with 50cm resolution for DSM. URL `https://data.gov.uk/dataset/0ab507af-cd91-40cb-8524-3efafc267211/lidar-composite-dsm-50cm` accessed: `2018-12-01`.

UK Met Office (2018). UK Met Office climate data. URL `https://www.metoffice.gov.uk/public/weather/climate/gcpsvg3nc?tab=climateTables` accessed: `2018-05-15`.

UNFPA (2012). State of World Population 2012. Tech. rep., United Nations Population Fund.

United Nations Environment Programme (2014). Green Infrastructure Guide for Water Management: Ecosystem-based management approaches for water-related infrastructure projects. Tech. rep., DEP/1827/NA.

Uno, I., Cai, X. M., Steyn, D. G., & Emori, S. (1995). A simple extension of the Louis method for rough surface layer modelling. *Boundary-Layer Meteorol.*, *76*(4), 395–409. DOI `https://doi.org/10.1007/BF00709241`.

Van den Hurk, B., Viterbo, P., Beljaars, A. C. M., & Betts, A. K. (2000). Offline validation of the ERA40 surface scheme, 295. Tech. rep., ECMWF.

Van Reeuwijk, M. (2007). *Direct simulation and regularization modeling of turbulent thermal convection*. Ph.D. thesis, TU Delft.

Verzicco, R., Mohd-Yusof, J., Orlandi, P., & Haworth, D. (2000). Large Eddy Simulation in Complex Geometric Configurations Using Boundary Body Forces. *AIAA J.*, *38*(3), 427–433. DOI `https://doi.org/10.2514/2.1001`.

Vreman, A. W. (2004). An eddy-viscosity subgrid-scale model for turbulent shear flow: Algebraic theory and applications. *Phys. fluids*, *16*(10), 3670–3681. DOI `https://doi.org/10.1063/1.1785131`.

Walker, T., Xue, S.-C., & Barton, G. W. (2010). Numerical determination of radiative view factors using ray tracing. *J. Heat Transfer*, *132*(7), 72702. DOI `https://doi.org/10.1115/1.4000974`.

Wesseling, P. (1996). von Neumann stability conditions for the convection-diffusion eqation. *IMA J. Numer. Anal.*, *16*(4), 583–598. DOI `https://doi.org/10.1093/imanum/16.4.583`.

Wicker, L. J., & Skamarock, W. C. (2002). Time-Splitting Methods for Elastic Models Using Forward Time Schemes. *Mon. Weather Rev.*, *130*(8), 2088–2097. DOI `https://doi.org/10.1175/1520-0493(2002)130<2088:TSMFEM>2.0.CO;2`.

Wu, L. (1995). *URBAN4: An Urban Canopy Layer Surface Energy Balance Climate Model*. Ph.D. thesis, University of California, Los Angeles.

Yaghoobian, N., & Kleissl, J. (2012). Effect of reflective pavements on building energy use. *Urban Clim.*, *2*, 25–42. DOI `https://doi.org/10.1016/j.uclim.2012.09.002`.

Yang, J., Wang, Z.-H., Georgescu, M., Chen, F., & Tewari, M. (2016). Assessing the Impact of Enhanced Hydrological Processes on Urban Hydrometeorology with Application to Two Cities in Contrasting Climates. *J. Hydrometeorol.*, *17*(4), 1031–1047. DOI `https://doi.org/10.1175/JHM-D-15-0112.1`.

Zhu, S., Guan, H., Bennett, J., Clay, R., Ewenz, C., Benger, S., Maghrabi, A., & Millington, A. C. (2013). Influence of sky temperature distribution on sky view factor and its applications in urban heat island. *International Journal of Climatology*, *33*(7), 1837–1843. DOI `https://doi.org/10.1002/joc.3660`.

Appendices

A

View factor calculation

A.1 Contour integration for view factors between two finite areas

By employing Stokes' theorem the area integrals for view factor (Eq. (4.2)) can be transferred to contour integrals. The significant advantage of this transformation is the reduction of integrations that need to be carried out from four to two. Following Howell et al. (2010) Stokes' theorem in three dimensions can be expressed as

$$\oint_{C_i} Pdx + Qdy + Rdz = \int_{A_i} \left[\cos\alpha \left(\frac{\partial R}{\partial y} - \frac{\partial Q}{\partial z} \right) + \cos\beta \left(\frac{\partial P}{\partial z} - \frac{\partial R}{\partial x} \right) + \cos\gamma \left(\frac{\partial Q}{\partial x} - \frac{\partial P}{\partial y} \right) \right] d_{A_i} \tag{A.1}$$

where P, Q and R are twice differentiable functions and α, β and γ are the angles between the axes and the local surface normal (see Fig. 4.5). The view factor between a differential area element di and a finite area j is defined as:

$$\psi_{di,j} = \int_{\mathrm{A_j}} \frac{\cos\theta_i \cos\theta_j}{\pi S^2} dA_j. \tag{A.2}$$

The integrand in Eq. (A.2) is $(\cos\theta_i \cos\theta_j/(\pi S^2))dA_j$. Using vector geometry the two cosines can be expressed as:

$$\cos\theta_i = \frac{x_j - x_i}{S}\cos\alpha_i + \frac{y_j - y_i}{S}\cos\beta_i + \frac{z_j - z_i}{S}\cos\gamma_i \tag{A.3}$$

$$\cos\theta_j = \frac{x_i - x_j}{S}\cos\alpha_j + \frac{y_i - y_j}{S}\cos\beta_j + \frac{z_i - z_j}{S}\cos\gamma_j. \tag{A.4}$$

Substituting (A.3) and (A.4) into (A.2) gives:

$$\psi_{di,j} = \int_{\mathrm{A_j}} S^{-4}((x_j - x_i)\cos\alpha_i + (y_j - y_i)\cos\beta_i + (z_j - z_i)\cos\gamma_i) \tag{A.5}$$
$$\times((x_i - x_j)\cos\alpha_j + (y_i - y_j)\cos\beta_j + (z_i - z_j)\cos\gamma_j)\, dA_j.$$

Let

$$l = \cos\alpha, \quad m = \cos\beta, \quad n = \cos\gamma,$$
$$f = \frac{(x_j - x_i)l_i + (y_j - y_i)m_i + (z_j - z_i)n_i}{\pi S^4}.$$

Equation (A.5) can then be written as:

$$\psi_{di,j} = \int_{\mathrm{A_j}} (x_i - x_j)fl_j + (y_i - y_j)fm_j + (z_i - z_j)fn_j\, dA_j. \tag{A.6}$$

Comparing Eq. (A.6) to the right-hand side of Eq. (A.1) Sparrow (1963) found

$$P = \frac{-m_i(z_j - z_i) + n_i(y_j - y_i)}{2\pi S^2},$$
$$Q = \frac{l_i(z_j - z_i) - n_i(x_j - x_i)}{2\pi S^2},$$
$$R = \frac{-l_i(y_j - y_i) + m_i(x_j - x_i)}{2\pi S^2}.$$

Using Stokes' Theorem $\psi_{di,j}$ is then given by

$$\psi_{di,j} = \oint_{C_j} (Pdx_j + Qdy_j + Rdz_j)\,. \tag{A.7}$$

The view factor between the two finite areas i and j is related to $\psi_{di,j}$ via

$$
\begin{aligned}
A_i\psi_{i,j} =& \int_{A_i} \psi_{di,j}\, dA_i, && \text{(A.8)}\\
=& \frac{1}{2\pi}\oint_{C_j}\left[\int_{A_i}\frac{-m_i(z_j-z_i)+n_i(y_j-y_i)}{S^2}dA_i\right]dx_j && \text{(A.9)}\\
&+\frac{1}{2\pi}\oint_{C_j}\left[\int_{A_i}\frac{l_i(z_j-z_i)-n_i(x_j-x_i)}{S^2}dA_i\right]dy_j\\
&+\frac{1}{2\pi}\oint_{C_j}\left[\int_{A_i}\frac{-l_i(y_j-y_i)+m_i(x_j-x_i)}{S^2}dA_i\right]dz_j.
\end{aligned}
$$

Stokes' theorem can again be applied on each of the area integrals in Eq. (A.9). Suitable solutions following Sparrow & Cess (1978) are $P = \ln S$, $Q = 0$, $R = 0$. The view factor $\psi_{i,j}$ can then be calculated according to

$$
\begin{aligned}
\psi_{i,j} =& \frac{1}{2\pi A_i}\oint_{C_j}\left[\oint_{C_i}\ln S dx_i\right]dx_j && \text{(A.10)}\\
&+\frac{1}{2\pi A_i}\oint_{C_j}\left[\oint_{C_i}\ln S dy_i\right]dy_j\\
&+\frac{1}{2\pi A_i}\oint_{C_j}\left[\oint_{C_i}\ln S dz_i\right]dz_j,
\end{aligned}
$$

or more compactly

$$\psi_{i,j} = \frac{1}{2\pi A_i}\oint_{C_i}\oint_{C_j}\left[\ln S dx_j dx_i + \ln S dy_j dy_i + \ln S d_j d_i\right]. \tag{A.11}$$

A.2 Gauss - Legendre quadrature

Quadrature is used in numerical analysis to approximate the integral of a function f over an integration domain $[a, b]$. For this the integration domain is commonly first changed to $[-1, 1]$ according to:

$$\int_a^b f(x)dx = \frac{b-a}{2}\int_{-1}^{1} f\left(\frac{b-a}{2}x + \frac{a+b}{2}\right)dx \tag{A.12}$$

Gauss-Legendre quadrature assumes that $f(x)$ can be expressed as $g(x)$ multiplied by a weight function $w(x)$:

$$\int_{-1}^{1} f(x)dx \approx \int_{-1}^{1} w(x)g(x)dx, \tag{A.13}$$

where $g(x)$ is approximately polynomial. The quadrature rule can then be written as

$$\int_{-1}^{1} w(x)g(x)dx = \sum_{i}^{n} w_i g(x_i), \tag{A.14}$$

where x_i are the nodes and w_i are the quadrature weights. Equation (A.14) contains $2n$ free parameters and we can choose w_i and x_i such that the integral of g, were it a polynomial of degree $2n-1$, could be evaluated exactly. For this the nodes $x_1, .., x_n$ should be chosen to be the roots of the degree-n Legendre polynomial $P_n(x)$ and the weights are then given by

$$w_i = \int_{-1}^{1} \prod_{k=1,k\neq i}^{n} \frac{x - x_i}{x_k - x_i} dx. \tag{A.15}$$

The Legendre polynomials can be defined via the recursive relation:

$$P_{n+1}(x) = \frac{2n+1}{n+1} x P_n(x) - \frac{n}{n+1} P_{n-1}(x), \text{ with } P_0(x) = 1,\ P_1(x) = x \tag{A.16}$$

Roots and weights for Gauss - Legendre quadrature are readily available in the literature, e.g. Lowan et al. (1942).

A.3 Analytical solutions for view factors

For certain configurations of planar surfaces i and j the view factors can be calculated analytically Wu (1995), Howell (2018). Some analytical solutions were compared to numerical ones in section 4.3.4 to verify the numerical computation. The formulae for all cases shown in Figure A.1 are given below, where the cases are numbered left to right, top to bottom.

Case 1 represent the solution for two identical, parallel, directly opposed rectangles. The view factor $\psi_{i,j}$ is calculated between the surfaces i and j, which both have the dimensions $y_1 \times z_1$ and are separated by a distance x_1. In this situation

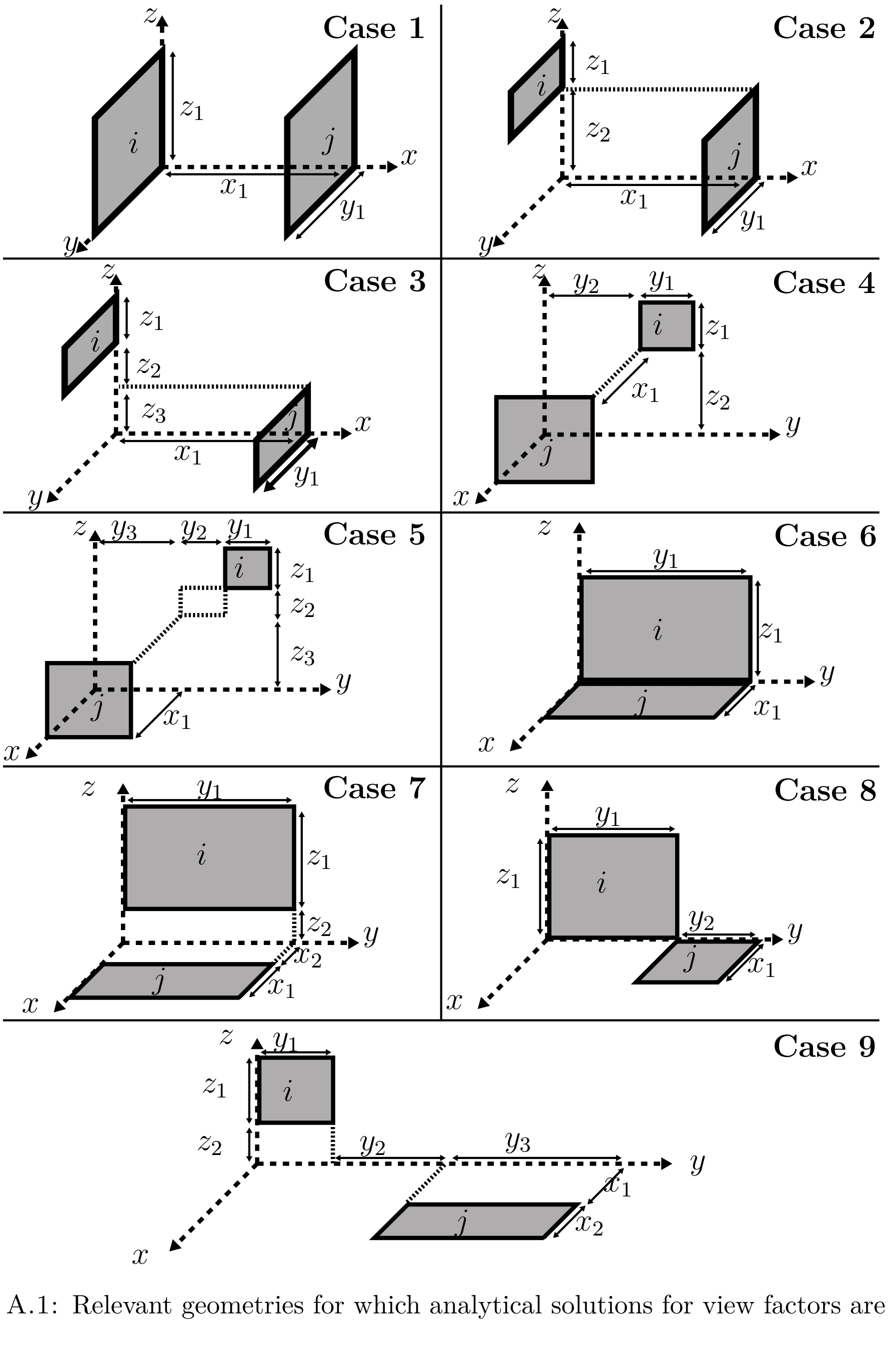

Figure A.1: Relevant geometries for which analytical solutions for view factors are known.

$\psi_{i,j} = \psi_{j,i}$, since the area of i and j are identical and $\psi_{i,j}$ is given by:

$$\begin{aligned}
a =& \frac{z_1}{x_1}, \quad b = \frac{y_1}{x_1} \\
\psi_{i,j} =& F_1(x_1, y_1, z_1) \\
=& \frac{2}{\pi ab} \left[\ln \sqrt{\frac{(1+a^2)(1+b^2)}{1+a^2+b^2}} + a\sqrt{1+b^2} \arctan \frac{a}{\sqrt{1+b^2}} \right. \\
& \left. + b\sqrt{1+a^2} \arctan \frac{b}{\sqrt{1+a^2}} - a \arctan a - b \arctan b \right].
\end{aligned} \tag{A.17}$$

Case 2 represent the solution for two parallel rectangles with one side of equal length and one "common" edge. The solutions for cases 2-5 can be derived using the additive and reciprocal rules (Eq. (4.4) & (4.3)) together with the analytical solution for case 1.

$$\begin{aligned}
\psi_{i,j} =& F_2(x_1, y_1, z_1, z_2) \\
=& \frac{1}{2y_1 z_1} \left[y_1(z_1+z_2) F_1(x_1, y_1, z_1+z_2) \right. \\
& \left. - y_1 z_1 F_1(x_1, y_1, z_1) - y_1 z_2 F_1(x_1, y_1, z_2) \right].
\end{aligned} \tag{A.18}$$

Case 3 represent the solution for two parallel rectangles with one side of equal length.

$$\begin{aligned}
\psi_{i,j} =& F_3(x_1, y_1, z_1, z_2, z_3) \\
=& \frac{z_1+z_2+z_3}{z_1} F_1(x_1, y_1, z_1+z_2+z_3) \\
& - F_1(x_1, y_1, z_1) - F_2(x_1, y_1, z_1, z_2) \\
& - \frac{z_2+z_3}{z_1} \left[F_1(x_1, y_1, z_2+z_3) + F_2(x_1, y_1, z_2+z_3, z_1) \right].
\end{aligned} \tag{A.19}$$

Case 4 represent the solution for two parallel rectangles with one "common" corner.

$$
\begin{aligned}
\psi_{i,j} =& F_4(x_1, y_1, y_2, z_1, z_2) \\
=& \frac{1}{2y_1 z_1} \left[(y_1 + y_2)(z_1 + z_2) F_1(x_1, y_1 + y_2, z_1 + z_2) \right. \\
& - (y_1 + y_2) z_1 F_1(x_1, y_1 + y_2, z_1) \\
& - (y_1 + y_2) z_2 F_1(x_1, y_1 + y_2, z_2) \\
& - (y_1 + y_2) z_2 F_2(x_1, y_1 + y_2, z_2, z_1) \\
& - y_1 z_1 F_2(x_1, y_1, z_1, z_2) \\
& \left. - y_2 z_1 F_2(x_1, y_2, z_1, z_2) \right] .
\end{aligned} \tag{A.20}
$$

Case 5 represent the solution for two parallel rectangles with arbitrary size and separation. With these 5 solutions all view factors between parallel rectangles can be calculated and the following cases deal with surfaces on perpendicular planes.

$$
\begin{aligned}
\psi_{i,j} =& F_5(x_1, y_1, y_2, y_3, z_1, z_2, z_3) \\
=& F_4(x_1, y_1, y_2 + y_3, z_1, z_2 + z_3) - F_4(x_1, y_1, y_2 + y_3, z_1, z_2) \\
& - F_4(x_1, y_2, y_2, z_1, z_2 + z_3) - F_4(x_1, y_1, y_2, z_1, z_2).
\end{aligned} \tag{A.21}
$$

Case 6 represent the solution for orthogonal rectangles with one side of equal length and a common edge.

$$
\begin{aligned}
a =& \frac{z_1}{y_1}, \quad b = \frac{x_1}{y_1} \\
\psi_{i,j} =& F_6(x_1, y_1, z_1) \qquad (A.22) \\
=& \frac{1}{\pi a} \left\{ a \arctan \frac{1}{a} + b \arctan \frac{1}{b} \right. \\
& - \sqrt{a^2 + b^2} \arctan \frac{1}{\sqrt{a^2 + b^2}} \\
& + \frac{1}{4} \log \left[\frac{(1 + a^2)(1 + b^2)}{(1 + a^2 + b^2)} \right. \\
& \times \left(\frac{a^2(1 + a^2 + b^2)}{(1 + a^2)(a^2 + b^2)} \right)^{a^2} \\
& \left. \left. \times \left(\frac{b^2(1 + b^2 + a^2)}{(1 + b^2)(b^2 + a^2)} \right)^{b^2} \right] \right\}.
\end{aligned}
$$

Case 7 represent the solution for orthogonal rectangles with one side of equal length. This and the following two solution can be derived using the additive and reciprocal rules together with the analytical solution for case 6.

$$
\begin{aligned}
\psi_{i,j} =& F_7(x_1, x_2, y_1, z_1, z_2) \qquad (A.23) \\
=& \frac{1}{x_1 y_1} \left[y_1(x_1 + x_2) F_6(x_1 + x_2, y_1, z_1 + z_2) \right. \\
& \left. - y_1(x_1 + x_2) F_6(x_1 + x_2, y_1, z_1) - x_2 y_1 F_6(x_2, y_1, z_1 + z_2) \right].
\end{aligned}
$$

Case 8 represent the solution for orthogonal rectangles with one common corner.

$$
\begin{aligned}
\psi_{i,j} =& F_8(x_1, y_1, y_2, z_1) \qquad (A.24) \\
=& \frac{1}{2 x_1 y_1} \left[(y_1 + y_2) x_1 F_6(x_1, y_1 + y_2, z_1) \right. \\
& \left. - x_1 y_1 F_6(x_1, y_1, z_1) - x_1 y_2 F_6(x_1, y_2, z_1) \right].
\end{aligned}
$$

Case 9 represent the solution for orthogonal rectangles of arbitrary size and separation.

$$
\begin{aligned}
\psi_{i,j} =& F_9(x_1, x_2, y_1, y_2, y_3, z_1, z_2) \\
=& \frac{z_1 + z_2}{z_1} \left[F_8(x_1 + x_2, y_1, y_2 + y_3, z_1 + z_2) \right. \\
&- F_8(x_1 + x_2, y_1, y_2, z_1 + z_2) - F_8(x_1, y_1, y_2 + y_3, z_1 + z_2) + F_8(x_1, y_1, y_2, z_1 + z_2)] \\
&+ \frac{z_2}{z_1} \left[F_8(x_1 + x_2, y_1, y_2 + y_3, z_2) \right. \\
&- F_8(x_1, y_1, y_2 + y_3, z_2) - F_8(x_1 + x_2, y_1, y_2, z_2) + F_8(x_1, y_1, y_2, z_2)] \, .
\end{aligned}
\tag{A.25}
$$